



Optimisation of a High Aspect-Ratio Transport Wing Using Coupled High-Fidelity Methods

Luís Miguel Martins Pacheco

Thesis to obtain the Master of Science Degree in

Aerospace Engineering

Supervisors: Prof. André Calado Marta

Eng. Ögmundur Petersson

Examination Committee

Chairperson: Prof. Afzal Suleman Supervisor: Prof. André Calado Marta

Member of the Committee: Prof. Fernando José Parracho Lau

To my parents.



Declaration

I declare that this document is an original work of my own authorship and that it fulfills all the requirements of the Code of Conduct and Good Practices of the Universidade de Lisboa.

Acknowledgments

I would like to express my heartfelt gratitude to my supervisor, Professor André Marta, for his guidance and enthusiasm throughout this project and during his lectures. I am equally thankful to Engineer Ögmundur Petersson for his exceptional mentorship, supervision, and for providing me with the opportunity to conduct my research at Airbus Defence and Space.

I extend my sincere thanks to the entire team of the Stress Methods and Optimisation department in Manching, particularly to Reinhold Maierl and Sebastian Deinert, for their time and invaluable advice. I would also like to thank Fabian Volle for his insights and support in setting up the optimisations. My appreciation also goes to my colleague Hannes Golombek for the shared laughter and camaraderie during my stay in Germany.

Furthermore, I am deeply thankful to my godmother and to all of my inspiring friends, whose encouragement continuously motivated me to strive for excellence.

Above all, I wish to express my profound gratitude to my family - my mother, father, and brother - for their unwavering support.



Resumo

O presente trabalho investiga o impacto do aumento do alongamento da asa na performance de aeronaves modernas e a influência de diferentes objetivos nos compromissos de projeto durante o dimensionamento estrutural. Duas asas compósitas com elevado alongamento de uma aeronave de médio alcance foram dimensionadas estruturalmente e a sua performance comparada. Três objetivos foram considerados: minimização da massa, maximização da eficiência aerodinâmica e maximização do alcance de Breguet. As otimizações foram realizadas com Lagrange, uma ferramenta de análise e otimização estrutural da Airbus, e TAU, a ferramenta de CFD do DLR. Um algoritmo de otimização baseado em gradientes, com análise direta de derivadas, foi utilizado. As variáveis de design são aproximadamente 3,000 e incluem a espessura e área do revestimento, longarinas e reforços. As restrições incluem resistência estrutural, buckling e critérios de manufatura. Torção aerodinâmica negativa na asa é introduzida com aeroelastic tailoring, criando um alívio passivo de cargas através de uma distribuição de sustentação em forma de sino, reduzindo os momentos fletores na raiz da asa. Os critérios de manufatura constituem a restrição mais severa, impedindo uma maior redução da massa. Para os pontos de design investigados, os benefícios de aumentar o alongamento da asa em aeronaves modernas foram demonstrados, em particular o aumento da eficiência aerodinâmica e a redução do arrasto, apesar do aumento da massa estrutural. Para além disso, são realçadas as características de design distintas que surgem para diferentes objetivos e a importância de um objetivo multidisciplinar para guiar os compromissos nas fases iniciais do projeto.

Palavras-Chave: otimização multidisciplinar, dimensionamento estrutural, asas compósitas, aeroelastic tailoring, alívio passivo de cargas.



Abstract

This work studies the influence of increasing the wing aspect ratio on the performance of modern transport aircraft and examines how different objective functions affect structural sizing design trade-offs. To this end, two high aspect-ratio composite medium-range transport aircraft wings underwent aeroelastic structural sizing, and their performances were compared. The optimisations were conducted using Airbus's in-house MDO suite and structural solver Lagrange and DLR's CFD solver TAU. Three objectives were considered: mass minimisation, aerodynamic efficiency maximisation, and Breguet range maximisation. A gradient-based algorithm with direct sensitivity analysis was used. Design variables, numbering approximately 3,000, included structural sizing parameters such as the thickness or crosssectional area of the skin, spars, and stringers. Constraints reflected industry requirements, encompassing structural strength, buckling stability, and manufacturing criteria. Wing washout was induced solely with aeroelastic tailoring, promoting passive load alleviation through a bell-shaped lift distribution, effectively reducing the wing root bending moment. Manufacturing requirements constituted the most restrictive constraint in achieving further mass savings. For the investigated design points, the benefits of increasing the aspect ratio in modern transport aircraft were demonstrated, notably the improvement in aerodynamic efficiency and reduction in drag, despite the increase in structural weight. Furthermore, the markedly different design characteristics arising from different objective functions, and the value of a multidisciplinary performance-based objective in guiding early-stage design trade-offs were highlighted.

Keywords: multidisciplinary design optimisation, structural sizing, composite wings, aeroelastic tailoring, passive load alleviation.



Contents

	Ackı	nowled	gments	vii		
	Res	umo .		ix		
	Abs	tract .		xi		
	List	of Table	es	xvii		
	List	of Figu	res	xix		
	Non	nenclati	ure	xxi		
	Glos	ssary		xxv		
1	Intro	oductio		1		
	1.1	Motiva	ation	1		
	1.2	Metho	ods, Objectives and Deliverables	3		
	1.3	Thesis	s Overview	4		
2	Airc	raft De	esign	7		
	2.1	Traditi	onal Aircraft Design	7		
	2.2	Mode	rn Design Challenges	8		
	2.3	Wing	Design	10		
	2.4	Nume	rical Optimisation	14		
	2.5	Multid	isciplinary Design Optimisation	15		
		2.5.1	Optimisation Algorithms	15		
		2.5.2	Sensitivity Analysis	17		
		2.5.3	Multidisciplinary Optimisation Architectures	21		
		2.5.4	Multidisciplinary Analysis Methods	22		
3	Stru	Structural Sizing Framework for Minimum Mass 23				
	3.1	Struct	ural Sizing Workflow	23		
	3.2	Param	netric Geometry Model	24		
	3.3 Aeroelastic Analysis and Optimisation		lastic Analysis and Optimisation	26		
	3.4	Aeroe	lastic Analysis Models	28		
		3.4.1	Aerodynamic Model	28		
		3.4.2	Structural Model	30		
		3.4.3	Fluid-Structure Coupling Model	33		

	3.5	Structu	ıral Sizing Criteria and Requirements	33
		3.5.1	Strength Requirements	34
		3.5.2	Buckling Requirements	34
		3.5.3	Manufacturing Requirements	34
4	Airc	raft Per	formance Analysis Framework	37
	4.1	Flight F	Performance	37
	4.2	Aerostr	ructural Analysis	38
	4.3	Trimmi	ng	39
	4.4	Aerody	namic Discipline	40
	4.5	Structu	ıral Discipline	40
	4.6	Loads	and Displacement Transfer	41
	4.7	Aerody	namic Mesh Deformation	41
5	DLR	R-F25 M	odels	43
	5.1	Geome	etric Models	43
		5.1.1	Baseline Configuration	43
		5.1.2	Higher Aspect-Ratio Variant	45
	5.2	Structu	ral Models	46
	5.3	.3 Aerodynamic Models		49
		5.3.1	Structural Sizing Optimisation	49
		5.3.2	Aircraft Performance	50
	5.4	Couplin	ng Models	50
6	DLR	R-F25 St	ructural Sizing Optimisation for Minimum Mass	53
	6.1	Probler	m Definition	53
		6.1.1	Optimisation Parameters	53
		6.1.2	Load Cases	53
		6.1.3	Design Variables	54
		6.1.4	Structural Sizing Criteria	55
		6.1.5	Trimming	58
	6.2	Optimis	sation Workflow	58
	6.3	DLR-F	25 Baseline Properties	59
	6.4	Static S	Structural Sizing	60
		6.4.1	Wingbox Mass	60
		6.4.2	Wingbox Deformation	61
		6.4.3	Wing Skin Thickness	62
	6.5	Aeroelastic Structural Sizing		
		6.5.1	Wingbox Mass and Deformation	63
		6.5.2	Wing Skin Thickness	64

		6.5.3	Wing Skin Ply Shares	. 65
		6.5.4	Wing Skin Reserve Factors	. 66
	6.6	Perfor	mance Analysis	. 68
		6.6.1	In-flight Twist Distribution	. 68
		6.6.2	Lift Distribution	. 68
		6.6.3	Drag Decomposition	. 69
		6.6.4	Breguet Range	. 70
7	DLF	R-F25 S	tructural Sizing for Maximum Aerodynamic Efficiency or Breguet Range	71
	7.1	Proble	em Definition	. 71
	7.2	Struct	ural Sizing for Aerodynamic Efficiency	. 72
	7.3	Struct	ural Sizing for Breguet Range	. 73
	7.4	Lift Dis	stributions	. 74
	7.5	Pareto	Fronts	. 75
8	Con	clusio	ns and Future Work	77
	8.1	Summ	nary	. 77
	8.2	Outloo	bk	. 78
Bi	bliog	raphy		79
Α	Stru	ıctural	Sizing Optimisation	91
	A.1	Static	Structural Sizing	. 91
		A.1.1	F25-AR17	. 91
	A.2	Aeroe	lastic Structural Sizing	. 92
		A.2.1	F25-AR15	. 92
		A 2 2	E95 AD17	0.4



List of Tables

5.1	DLR-F25 wing key characteristics: baseline and higher aspect-ratio wings	46
5.2	Structural discretization and elements of the F25-AR15 and F25-AR17 wings	48
6.1	Optimisation parameters used for structural sizing	54
6.2	Load cases considered in the structural sizing optimisation	54
6.3	Design variables and their bounds for structural sizing	56
6.4	Structural sizing optimisation problem size	57
6.5	Wingbox structural mass throughout the static structural sizing	60
6.6	Wingtip displacement throughout the static structural sizing	61
6.7	Wingbox structural mass after aeroelastic structural sizing	64
6.8	Comparison of wing drag counts in cruise between the F25-AR17 and F25-AR15	69
7.1	Structural and aerodynamic characteristics of the optimised designs	74



List of Figures

1.1	Flight forecast for Europe between 2019 and 2050	2
1.2	Projected CO_2 emission scenarios for aviation from 2020 to 2050	2
1.3	Master's dissertation workflow.	4
2.1	Integration of MDO into the design process	9
2.2	Main structural components of a typical transport aircraft wingbox	10
2.3	Elliptic and aerostructural optimum lift distribution	13
2.4	XDSM diagram for the MDF architecture	21
2.5	XDSM diagram for a MDF architecture with a Gauss-Seidel multidisciplinary analysis	22
3.1	Aeroelastic structural sizing optimisation process	24
3.2	CPACS parametric notation for a wing structure	25
3.3	Node mapping of a FE structural model to a parametric geometry	26
3.4	Remeshing or morphing of a modified parametric geometry	26
3.5	Interaction between aerodynamic forces and structural elasticity	27
3.6	Structural sizing optimisation process for minimum mass	28
3.7	Lifting surface idealization in the doublet lattice method	29
3.8	Forces acting on a CBAR element and degrees of freedom of a CQUAD4 element	32
3.9	Finite element model highlighting the applied elements	32
3.10	Continuity constraint applied to two neighbouring patches	35
4.1	Aircraft performance evaluation process	39
4.2	Coupled aerostructural analysis for performance evaluation	39
4.3	Force equilibrium in trimming for performance evaluation	40
5.1	Outer geometry of the DLR-F25 baseline configuration	44
5.2	DLR-F25 wing planform	44
5.3	DLR-F25 wing control surfaces	45
5.4	Schematic representation of different aspect-ratio variation methods	45
5.5	Shape and topological modifications to the F25-AR17 wing	47
5.6	F25-AR15 FE structural model	47
5.7	F25-AR15 CONM2 mass point distribution.	48

5.8	F25-AR15 doublet lattice method mesh	49
5.9	F25-AR15 high-fidelity aerodynamic surface mesh	50
5.10	F25-AR15 wing coupling for structural sizing	51
6.1	F25-AR15 wingbox design variable patches	54
6.2	Design variable linking.	55
6.3	T-shaped stringer profile	55
6.4	F25-AR15 wing upper skin, spars and stringers buckling fields	57
6.5	Minimum thickness requirements	57
6.6	Force and pitching moment equilibrium in trimming for structural sizing	58
6.7	Structural sizing optimisation workflow	58
6.8	F25-AR15 wing upper skin uniform thickness and strength constraint violation prior to	
	structural sizing.	59
6.9	Bending and twist distributions prior to structural sizing.	60
6.10	Bending and twist distributions after static structural sizing.	61
6.11	F25-AR15 wing upper skin thickness distribution throughout the static structural sizing	62
6.12	F25-AR15 wing lower skin thickness distribution throughout the static structural sizing	63
6.13	Bending and twist distributions after aeroelastic structural sizing	64
6.14	Wing skin thickness distribution after aeroelastic structural sizing	65
6.15	F25-AR15 wing upper skin ply share distribution after aeroelastic structural sizing	66
6.16	F25-AR15 wing upper skin reserve factors after aeroelastic structural sizing.	67
6.17	Twist distribution in cruise	68
6.18	Lift distribution in cruise	69
7.1	Structural sizing optimisation process for aerodynamic efficiency or Breguet range	72
7.2	Convergence history of the structural sizing optimisations for aerodynamic efficiency	73
7.3	Convergence history of the structural sizing optimisations for Breguet range	73
7.4	Lift distributions for the structural sizing optimisations for mass, aerodynamic efficiency,	
	and Breguet range	75
7.5	F25-AR15 and F25-AR17 Pareto fronts	75
A.1	F25-AR17 wing upper skin thickness distribution throughout the static structural sizing	91
A.2	F25-AR17 wing lower skin thickness distribution throughout the static structural sizing	91
A.3	F25-AR15 spar and stringer dimensions after aeroelastic structural sizing	92
A.4	F25-AR15 wing skin ply share distribution after aeroelastic structural sizing	92
A.5	F25-AR15 wing skin reserve factors after aeroelastic structural sizing	93
A.6	F25-AR17 spar and stringer dimensions after aeroelastic structural sizing	94
A.7	F25-AR17 wing skin ply share distribution after aeroelastic structural sizing	94
A.8	F25-AR17 wing skin reserve factors after aeroelastic structural sizing.	95

Nomenclature

Greek symbols

α	Angl	e of	attac	k

- Γ Doublet strength
- Δ Perturbation step
- ε Strain
- η Spanwise relative coordinate
- ν Poisson's ratio
- ξ Chordwise relative coordinate
- ρ Air density
- σ Stress
- ϕ_c Convective flux
- ϕ_v Diffusive flux
- ψ Adjoint vector

Roman symbols

- AR Aspect ratio
- AIC Aerodynamic influence coefficient matrix
- b Wingspan
- b_c Boundary conditions
- c Speed of sound
- C_D Coefficient of drag
- C_L Coefficient of lift
- D Drag

- E Young's modulus
- e Oswald efficiency factor
- f Force
- f Objective, cost or merit function
- g Constraint function vector
- G Shear modulus
- K Stiffness matrix
- L Lift
- L' Lift per unit span
- M Mapping operator
- Mach number
- q Dynamic pressure
- Residual vector
- R_{Br} Breguet range
- S Reference area
- u Structural displacement
- v Flow velocity vector
- V Flow velocity
- W Weight
- x Design variables vector
- y State variables vector

Subscripts

- δF Fluid flow boundary
- F Fluid flow discipline
- f Fibre
- i Induced drag
- ind Induced angle of attack
- δM Mesh deformation boundary

- ${\cal M}$ Mesh deformation discipline
- m Matrix
- p Parasite drag
- δS Structural boundary
- Structural discipline
- w Wave drag



Glossary

ACO Ant Colony Optimisation
AD Automatic Differentiation

AIC Aerodynamic Influence Coefficient

Airbus DS Airbus Defence and Space

AR Aspect Ratio

BFGS Broyden-Fletcher-Goldfarb-Shanno
CAJU Clean Aviation Joint Undertaking
CFD Computational Fluid Dynamics
CFRP Carbon Fibre Reinforced Polymer

CPACS Common Parametric Aircraft Configuration Scheme

CSM Computational Structural Mechanics

DLM Doublet Lattice Method
DLR German Aerospace Center

FD Finite-Difference

FDM Finite Difference Method

FE Finite Element

FVM Finite Element Method
FVM Finite Volume Method
HARW High Aspect-Ratio Wing

HPC High Performance Computing

ICAO International Civil Aviation Organization

IPS Infinite Plate Spline
KKT Karush-Kuhn-Tucker

MDA Multidisciplinary Design Analysis

MDAO Multidisciplinary Design Analysis and Optimisation

MDF Multidisciplinary Feasible

MDO Multidisciplinary Design Optimisation

MLS Moving Least SquaresMTOW Maximum Take-Off WeightMZFW Maximum Zero Fuel Weight

NASA National Aeronautics and Space AdministrationNLPQL Non-Linear Programming by Quadratic Lagrangian

RANS Reynolds-averaged Navier-Stokes

RBE Rigid Body Elements

RF Reserve Factor
SA Spalart–Allmaras

SNOPT Sparse Nonlinear Optimiser

SQP Sequential Quadratic Programming

TO Topology Optimisation

TSFC Thrust-Specific Fuel Consumption

UPWing Ultra Performance WingVLM Vortex Lattice Method

XDSM eXtended Design Structure Matrix

Chapter 1

Introduction

Aviation plays a vital role in modern society, however, its environmental impacts have become an increasingly pressing concern. This problem is poised to intensify as the current pace of technological advancements fails to offset the rise in emissions caused by air traffic growth. To address this challenge, the development of novel, environmentally sustainable aircraft configurations is imperative.

The present master's thesis aspires to investigate a Multidisciplinary Design Optimisation (MDO) approach focused on high aspect-ratio composite wings, with the objective of improving overall aircraft performance.

1.1 Motivation

The aviation industry exerts a profound influence on economic growth and societal development. It plays a pivotal role in addressing societal needs by providing rapid mobility for both passengers and freight. Furthermore, aviation strengthens economic competitiveness by stimulating business growth, opening new markets, boosting international trade, attracting investment, and enabling effective communication between regions and companies [1, 2].

Aviation remains indispensable for long-haul and intercontinental routes, and the industry is projected to grow significantly in the forthcoming decades. In Europe alone, EUROCONTROL forecasts over 16 million flights annually by 2050, representing a 44% increase compared to 2019 (pre-COVID-19), with an average annual growth rate of 1.2% [3], as depicted in Figure 1.1.

This surge in demand poses challenges, particularly in the context of the pressing issue of climate change. Currently, the aviation sector accounts for approximately 12% of transport-related emissions and 2% of all human-induced CO_2 emissions [1, 4]. Although fuel efficiency has improved over recent decades, with fuel consumption per hundred passengers-kilometre decreasing by 39% between 2005 and 2019 [5], the growth of air transport has outpaced these gains [6]. If current trends persist, global CO_2 emissions from aviation are projected to triple by 2050 compared to 2015 levels, potentially consuming 25% of the global carbon budget, as reported by the International Civil Aviation Organization (ICAO) [4, 7].

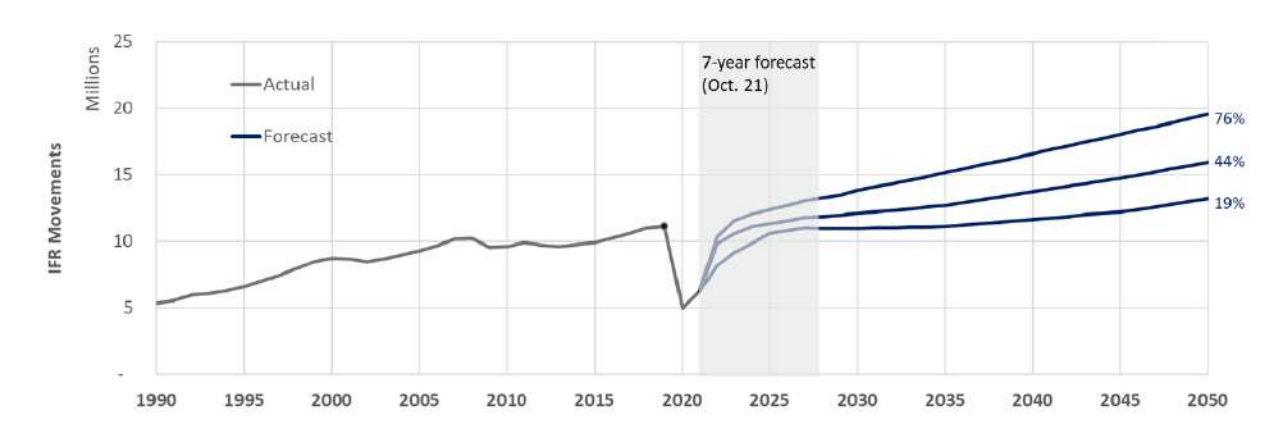


Figure 1.1: Flight forecast for Europe until 2050 under low, base, and high demand scenarios [3].

Figure 1.2 depicts the projected CO_2 emissions for aviation from 2020 to 2050 for different technological development scenarios, illustrating how the growth of air transport will outpace current efficiency gains, emphasising the urgent need for new technologies and sustainable solutions.

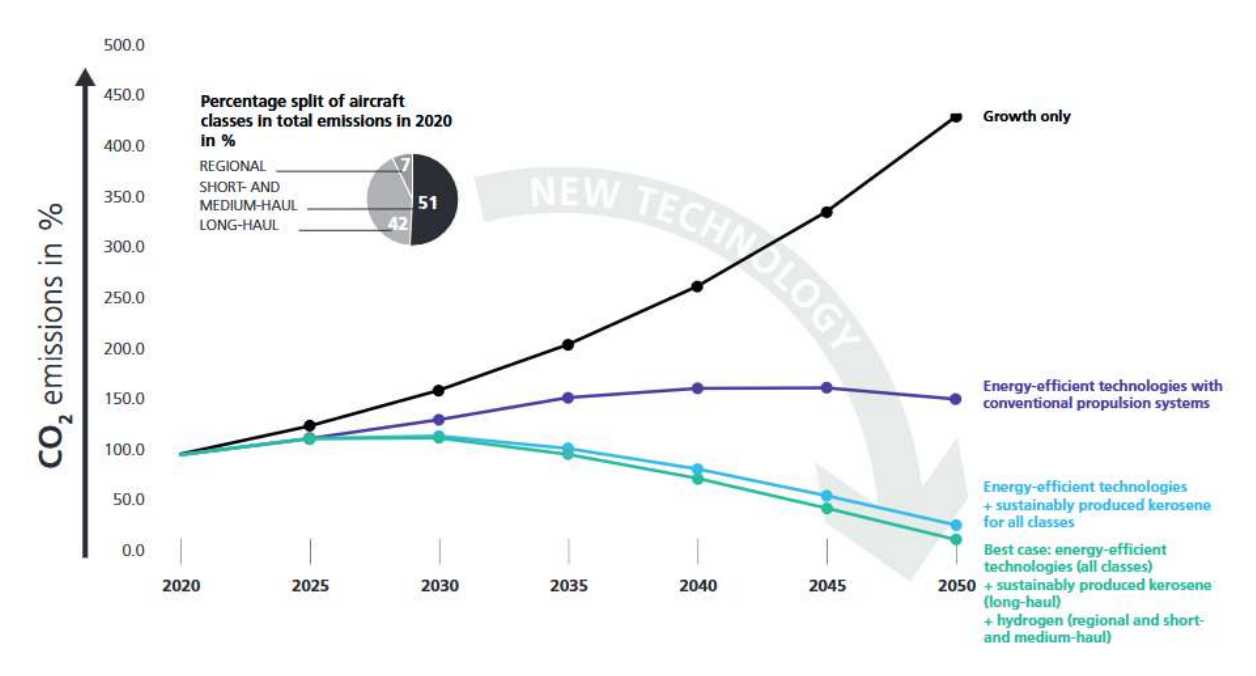


Figure 1.2: Projected CO_2 emissions for aviation from 2020 to 2050 for different technological development scenarios [8].

As global priorities shift towards ambitious climate objectives, achieving sustainability has become one of the foremost challenges of the aviation industry. Developing safe, reliable, cost-effective, and climate-neutral aviation solutions is paramount, as the sector must align with stringent environmental goals, such as the European Green Deal [6, 9]. A critical component of this transition involves improving overall aircraft efficiency, encompassing both aerodynamic and structural dimensions.

Among various proposed solutions, High Aspect-Ratio Wings (HARW) have emerged as a particularly effective concept to improve aerodynamic efficiency. Such designs can significantly reduce lift-induced drag during cruise [10, 11]. In fact, modern commercial aircraft are increasingly incorporating slender and more flexible wing designs [11, 12]. However, these configurations pose challenges. High

aspect-ratio wing aircraft have increased structural weight due to the reinforcements required to counteract the higher wing root bending moment these aircraft experience during flight [13, 14]. Additionally, slender wings are more susceptible to aeroelastic effects and non-linear aerodynamic and structural phenomena [10, 12, 15]. This gives rise to a tightly coupled and conflicting set of design objectives across the aerodynamic and structural domains. As such, a multidisciplinary design optimisation approach becomes essential to explore the inherent trade-offs of HARW in a highly automated manner and to determine the optimal balance between the disciplines while adhering to extensive competing constraints [11, 14, 16].

To advance sustainable aviation and meet the European Green Deal targets, the European Commission has established the Clean Aviation Joint Undertaking (CAJU), a consortium uniting international public and private partners. Within the purview of this consortium are industry leaders such as Airbus Defence and Space (Airbus DS) and research organisations such as the German Aerospace Centre (DLR). Among the key projects within Clean Aviation is the Ultra Performance Wing (UPWing) [17]. The research presented in this master's thesis was conducted over eight months in the Stress Methods and Optimisation department at Airbus DS in Manching, Germany, as part of the UPWing project.

1.2 Methods, Objectives and Deliverables

In the present study, a high-fidelity Multidisciplinary Design Analysis and Optimisation (MDAO) framework is used for the structural sizing optimisation of two high aspect-ratio composite wing aircraft. The primary objective of this study is to investigate the aerostructural trade-offs associated with increasing the wing aspect ratio of a medium-range transport aircraft, and to highlight the potential of composite high aspect-ratio wings to improve aircraft performance. Additionally, this thesis aims to examine the influence of varying objective functions on structural sizing.

An aeroelastic structural sizing optimisation is initially conducted with the structural mass as the objective function. The structural sizing optimisations are setup using Airbus's Defence and Space inhouse tool Descartes [18], which generates the aircraft's geometric model and the input data for the aeroelastic analyses and optimisations based on a parametric CPACS database [19–22]. Thereafter, Airbus's in-house MDO suite Lagrange [23, 24] is used to perform the structural sizing optimisations, ensuring the aircraft meet structural integrity requirements. Lagrange supports a range of gradient-based optimisation algorithms and allows for both shape and sizing variables under stringent constraints, including strength, buckling, and manufacturability [23]. The structural sizing yields an optimised aircraft.

Following the structural sizing for mass minimisation, the performance of the resulting aircraft configurations is evaluated with a high-fidelity aerostructural analysis, using a recently developed MDAO framework [25, 26]. This framework couples Lagrange with the DLR's Computational Fluid Dynamics (CFD) solver TAU [27–29] within the high-performance computing (HPC) software integration framework FlowSimulator. A quantitative comparison of the twist and lift distribution, aerodynamic drag, and Breguet range of both aircraft configurations is conducted to evaluate the influence of aspect ratio on aircraft performance.

Due to the differing fidelity requirements of the structural sizing and the performance evaluation frameworks, two levels of fidelity are used in this work for the aerodynamic discipline: linear aerodynamics is used to drive the structural sizing optimisation, whereas high-fidelity aerodynamics is used in the performance analysis framework.

In a subsequent phase of the thesis, following the conventional structural sizing for mass minimisation and the performance assessment, the investigation is extended to explore two alternative objective functions for structural sizing: the maximisation of aerodynamic efficiency and the maximisation of Breguet range. The goal is to compare how the different objective functions influence the final designs.

The three major steps of this dissertation's workflow are illustrated in Figure 1.3.



Figure 1.3: Master's dissertation workflow.

This research is conducted using the DLR-F25 aircraft model. Developed by DLR based on the Airbus A321neo, this model serves as a reference platform for investigating advanced aeronautical technologies, bridging contemporary and future aircraft configurations. Designed for the short- to medium-range market segment, the DLR-F25 features a wing with a high aspect ratio of 15.6. The DLR-F25 is integral to the Clean Aviation programme, providing a consistent baseline for evaluating and validating innovative technologies [30, 31].

1.3 Thesis Overview

This thesis is divided into eight chapters. Chapter 1 introduces the topic, providing an overview of the motivation for this work, the context in which the thesis is embedded, and a summary of the objectives, workflow, methods, tools, and deliverables of the dissertation.

Chapter 2 provides an overview of aircraft design. It begins with a discussion of the various phases of the traditional aircraft design process and highlights the associated challenges. Multidisciplinary design optimisation is subsequently introduced, and its role in addressing these challenges is emphasised. Additionally, the chapter explores typical wing design considerations, including the role of structural components and the effect of aerodynamic parameters on overall aircraft performance. Particular emphasis is placed on the wing aspect ratio and its influence on induced drag.

Chapter 3 delves into the aeroelastic structural sizing optimisation framework, detailing its inputs, outputs, and the numerical tools used. The chapter begins with a description of the parametric geometry modelling process and its advantages. This is followed by an explanation of the approach used to solve the optimisation problem and an overview of the analysis disciplines and their coupling.

Chapter 4 describes the aerostructural analysis framework used to evaluate aircraft performance. It provides an overview of the aerodynamic and structural disciplines, as well as the aerodynamic mesh deformation and load and displacement interpolation processes for the performance analysis module.

In Chapter 5, the baseline DLR-F25 aircraft model is described. The development of a higher aspectratio variant of the DLR-F25 is presented, along with a detailed description of all models required for the structural sizing optimisations and performance analyses. These include the structural, aerodynamic and coupling models for both aircraft.

In Chapter 6 the structural sizing for mass minimisation of both aircraft is presented. The chapter begins with a description of the optimisation model, including the optimisation parameters, design variables, criteria model, and load cases. Subsequently, the results of the structural sizing optimisations are presented. The optimised designs are analysed, and the different aspect-ratio aircraft are compared. Finally, the performance of both optimised aircraft is evaluated. The in-flight twist, lift distribution and the drag during cruise are analysed and juxtaposed between both aspect-ratio aircraft models. Additionally, the Breguet range for both aircraft is estimated and compared.

In Chapter 7, the results of the structural sizing optimisations with aerodynamic efficiency and Breguet range as the objective functions are presented and analysed. The designs of all structural sizing optimisations are compared. The influence of aspect ratio and the chosen objective function on overall aircraft performance is analysed.

Chapter 8 provides the summary and conclusions of the dissertation. The achievements of the work are outlined, along with discussions of potential future developments. Suggestions for improving and extending the current optimisation process are also provided.

Chapter 2

Aircraft Design

This chapter provides a brief overview of the traditional aircraft design process, highlighting the major challenges associated with this method. Multidisciplinary design optimisation is introduced as a potential solution, with an in-depth examination of this design approach and its advantages. Additionally, the chapter explores a typical wing design focusing on the purpose of each component and the various design parameters that influence aerodynamics. Particular emphasis is placed on the relationship between aspect ratio and induced drag, as well as their impact on overall aircraft performance.

2.1 Traditional Aircraft Design

Aircraft design is inherently iterative. To develop a new aircraft, various parameters from multiple engineering disciplines must be defined in response to specific requirements imposed by customers, manufacturers, regulatory agencies, or overarching initiatives like the European Green Deal. These requirements can range from top-level considerations, such as the aircraft's intended purpose, operational scope, and development timeline, to more technical specifications, including range, payload, speed, and even airport parking compatibility. Such requirements are typically derived from customer input, market analysis, or benchmarking of existing aircraft. Over the course of the design process, these requirements may evolve to accommodate a feasible and optimised solution.

The aircraft design process is traditionally divided into three major phases: conceptual, preliminary, and detailed design. Each phase builds upon the preceding one, with progressively higher levels of detail [32].

The conceptual design phase begins with the establishment of specifications and requirements for the new aircraft. During this phase, a broad spectrum of potential configurations is explored. Designers perform trade-off studies, comparing different designs and requirements, and utilise statistical models based on existing aircraft configurations. The objective is to identify the most promising design concept that balances competing requirements effectively [33]. Key tasks during this phase include estimating the aircraft's shape, weight, and performance characteristics. Critical aspects of the overall geometry, such as wing shape, wing-fuselage placement, and the configuration of the horizontal and vertical tails,

are determined. Additionally, this phase assesses the propulsion systems, payload capabilities, and the design's overall stability. Multiple alternative concepts are evaluated to identify the driving requirements and associated trade-offs. The outcome of the conceptual design phase are technically viable solutions that meet the initial specifications. One or more concepts are selected for further study in subsequent phases. However, these concepts may still undergo topological modifications or, in some cases, be discarded as the project progresses [32].

In the preliminary design phase, the selected concept is refined and analysed in greater detail by specialists across multiple engineering disciplines. Experts in structures, aerodynamics, landing gear, and control systems apply higher-fidelity analysis methods to evaluate the design. This phase includes rigorous testing in aerodynamics, structures, propulsion, stability and control, often involving wind tunnel experiments, CFD, and Computational Structural Mechanics (CSM) [32, 34]. Major subsystems are designed, and cost estimates are refined with greater accuracy. The overall configuration established during the conceptual design phase is expected to remain largely consistent; significant deviations at this stage would indicate a flawed conceptual design, necessitating a return to the earlier phase. By the conclusion of this phase, although the design is not yet ready for production, the configuration is frozen, and the manufacturer must decide whether to proceed with the detailed design and subsequent production. This decision carries substantial financial implications, as an unsuccessful product could result in considerable losses [32, 34]. The present work is situated within the scope of this phase.

The detailed design phase builds upon the aircraft model established during preliminary design. Structural components, such as ribs, spars, and skin panels are designed and analysed with meticulous detail, often requiring adjustments to address assembly and manufacturing considerations. This phase progressively improves weight and performance forecasts [32]. Upon completion of this phase, the aircraft is ready for production, followed by flight testing. Subsequently, growth versions of the aircraft, which start from the preliminary design phase, may be developed. These iterations leverage previous design knowledge to create optimised versions without major conceptual changes, thereby reducing costs associated with design, manufacturing, certification, and operation [33].

2.2 Modern Design Challenges

The increasing complexity of modern aircraft presents significant challenges to traditional design methodologies. The vastness of design spaces continues to grow, making it increasingly difficult for engineers to explore them effectively. Traditional aircraft design approaches often rely on assumptions and past experiences to constrain the design space to a manageable scale. However, this premature narrowing of the design space, often based on statistical models, can severely hinder the design process of novel unconventional configurations, such as high aspect-ratio wing aircraft, and ultimately, compromise the development of new high-performance solutions [35].

Furthermore, contemporary aircraft design requires a tight coupling to address the interactions between design-driving disciplines. This integration is particularly challenging as specialised expertise are frequently distributed among several teams operating across different organisations [36]. For instance,

structural design, which manually iterates between load calculations and structural sizing, becomes increasingly insufficient within this context. The combination of these challenges with shortened development timelines and constrained budgets, underscores the limitations of the traditional approach to modern aircraft design [23].

To overcome these challenges, multidisciplinary design optimisation methods are being increasingly adopted, particularly during the conceptual and preliminary design phases. MDO enables the exploration of extensive design spaces through a systematic approach capable of employing multi-fidelity numerical analysis models and methods. Unlike traditional aircraft design approaches, that rely on assumptions and best practices, MDO is a more data-driven methodology, whilst still enabling human ingenuity to play a meaningful role. Moreover, MDO facilitates the consideration of interactions between individual disciplines, for instance by integrating load calculations and structural sizing within a unified optimisation framework, while also allowing the simultaneous evaluation of a comprehensive set of competing design-driving requirements [35, 36].

Aircraft design is inherently multidisciplinary, and by integrating MDO from the outset of the design process, it is possible to exploit the interactions between design-driving disciplines, unlocking new design opportunities and maximising design knowledge during the stages of greatest design flexibility [13]. This approach leads to higher performance solutions while significantly reducing development time and costs, as illustrated in Figure 2.1

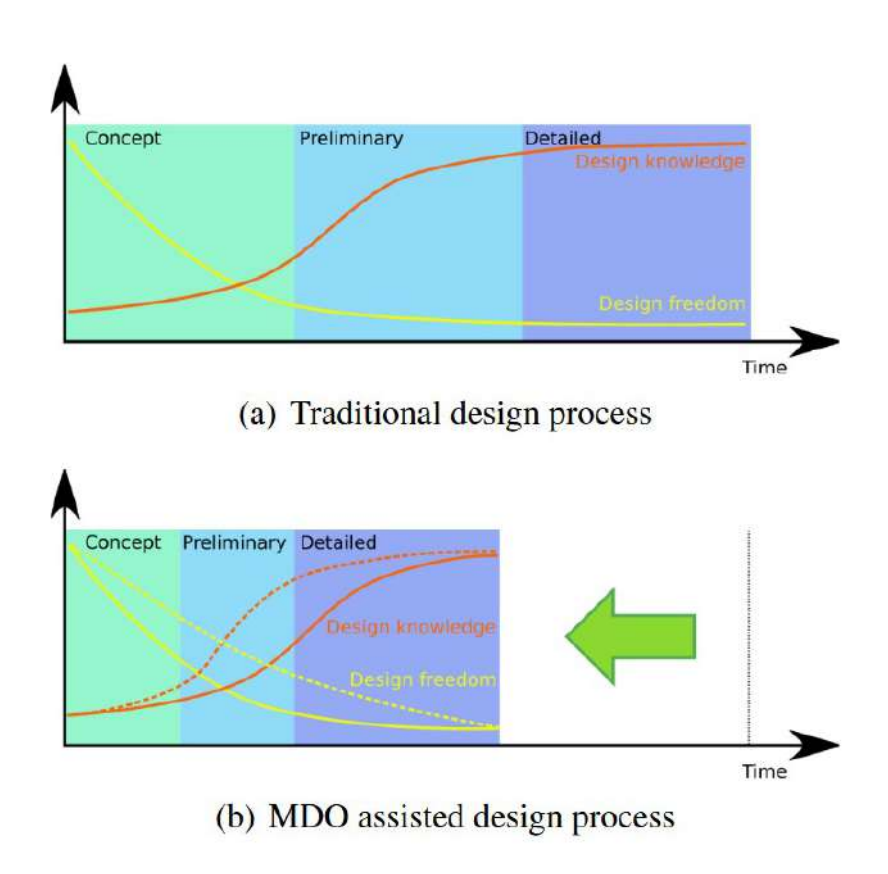


Figure 2.1: Benefits of integrating MDO into the design process [23].

2.3 Wing Design

The typical structural components of a wing, illustrated in Figure 2.2, include the skin panels, spars, ribs, and stringers, each serving a critical function [37–39]. The outer covering of the wing, referred to as the skin, is divided into panels and primarily functions as an impermeable surface that supports the aerodynamic pressure distribution responsible for generating lift. Additionally, wing covers transmit loads to the internal structure and, in modern stressed-skin construction, carry bending and torsional loads.

The spars are the principal load-bearing members, running longitudinally from the root to the tip of the wing. These components provide strength and stiffness to resist the bending, torsion, and shear forces encountered during flight, bearing the majority of the bending moment induced by aerodynamic lift and weight distribution.

Perpendicular to the spars are the ribs, which ensure that the wing's cross-sectional shape is maintained as designed under loading. Ribs also transmit concentrated loads into the structure and act as attachment points for control surfaces. Furthermore, they support the skin and stringers against buckling by acting as panel breakers and defining the skin panel and stringer column lengths.

Stringers, which are smaller longitudinal reinforcements running parallel to the spars and attached between the ribs, primarily serve to stiffen the skin, enabling it to withstand compression loads caused by wing bending and twisting. Collectively, the spars, skin, ribs, and stringers form the wingbox, an integrated structure that acts as the primary load-carrying element of the wing.

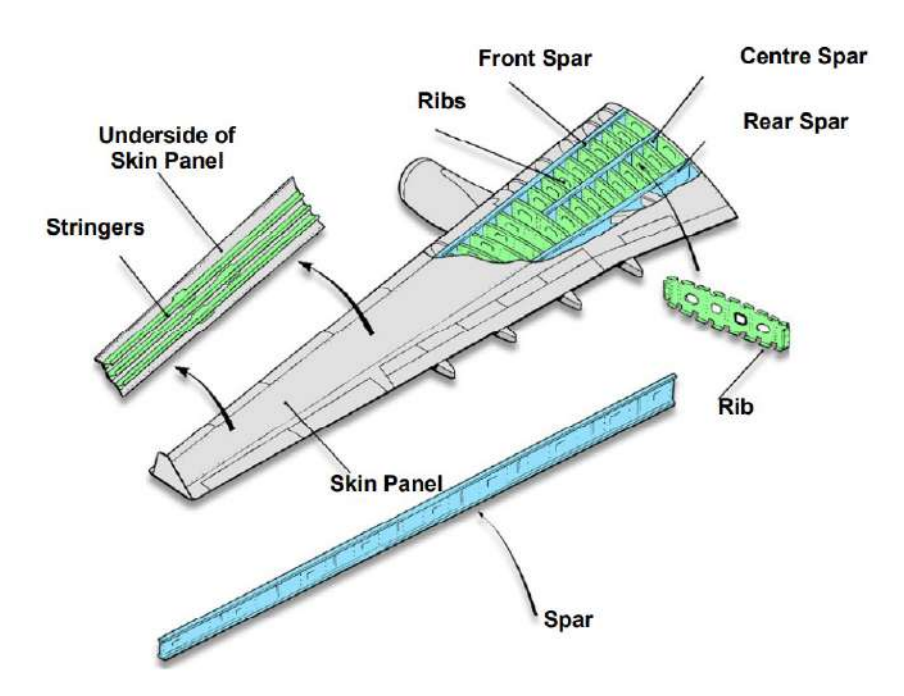


Figure 2.2: Main structural components of a typical transport aircraft wingbox [40].

An aircraft's wing can be characterised by several parameters, including aspect ratio (AR), sweep, twist and dihedral angles, span, and taper ratio. These parameters significantly influence the lift distribution and aerodynamic drag, thereby impacting wing efficiency, overall flight performance, and aircraft fuel consumption [41].

For a more effective comparison between different flight conditions, aircraft drag is often expressed as a dimensionless coefficient [42], given by

$$C_D = \frac{D}{q \cdot S} \,, \tag{2.1}$$

where D is the total drag, q is the dynamic pressure, and S is the reference area. The dynamic pressure is defined as

$$q = \frac{\rho \cdot V^2}{2} \,, \tag{2.2}$$

where ρ is the air density and V is the flow velocity.

The drag coefficient can be used to predict aircraft drag under different velocity and density conditions than those at which it was calculated, provided flow characteristics, such as the viscosity and compressibility, measured through the Reynolds and Mach numbers, respectively, remain similar [42].

The total drag experienced by the wing can be divided into three primary components, based on the aerodynamic effects and physical phenomena responsible for them [32, 43, 44]:

- Parasite drag (C_{Dp}): primarily arising from pressure drag and skin friction due to viscosity;
- Wave drag (C_{Dw}): caused by the formation of shock waves near or beyond Mach 1 due to compressibility effects. As this study focuses on subsonic flight, wave drag is not relevant;
- **Induced drag** (C_{Di}): generated as a consequence of aerodynamic lift production.

The total drag coefficient can thus be expressed as

$$C_D = C_{Dn} + C_{Dw} + C_{Di}, (2.3)$$

where C_D is the total drag coefficient, C_{Dp} the parasite drag coefficient, C_{Dw} the wave drag coefficient, and C_{Di} the induced drag coefficient.

Induced drag constitutes a significant portion of total drag, accounting for approximately 40% of the overall drag for large transport aircraft during cruise [43, 45]. Therefore, reducing induced drag is crucial to lowering fuel consumption and emissions. Induced drag arises due to the pressure differential between the upper and lower wing surfaces, which causes airflow from the lower surface to move around the wingtips, forming vortices. These vortices induce a downwash velocity on the flow, reducing the effective angle of attack α by the induced angle of attack $\alpha_{\rm ind}$. Consequently, the lift vector tilts rearward, resulting in a component of lift that acts as drag, hence the term "lift induced drag" [44, 46].

For planar wings and small angles of attack, the induced drag coefficient C_{Di} is given by [32, 46]

$$C_{Di} = \frac{C_L^2}{\pi \cdot AR \cdot e} \,, \tag{2.4}$$

where \mathcal{C}_L is the lift coefficient, AR is the aspect ratio, and e is the Oswald span efficiency factor. The

aspect ratio is defined as the square of the wingspan b divided by the wing area S

$$AR = \frac{b^2}{S}. ag{2.5}$$

For non-planar wings (e.g., those with camber or twist), the induced drag is calculated as [32, 46]

$$C_{Di} = rac{\left(C_L - C_{L, ext{min drag}}
ight)^2}{\pi \cdot AR \cdot e} \,.$$
 (2.6)

According to the lifting-line theory, for a planar wing, the minimum induced drag for a given C_L , wing area, and aspect ratio occurs when the spanwise lift distribution is elliptical [44], a principle first published by Prandtl in 1918 [47]. The Oswald efficiency factor, seen in Equations (2.4) and (2.6), serves as a correction to account for deviations in induced drag from that of an ideal wing with the same aspect ratio and an elliptical lift distribution [48]. For an ideal elliptical lift distribution, e=1. For planar wings, e=1 typically ranges between 0 and 1, whereas non-planar wing configurations can achieve values exceeding unity. Adjusting parameters such as twist or chord distribution along the wingspan can improve the lift distribution and enhance the Oswald efficiency factor [46]. Prandtl's lifting-line theory results provide a theoretical optimum against which drag reduction concepts can be compared.

Induced drag depends on the wing lift, speed, and span [43]. Increasing the wingspan reduces induced drag, even at the expense of a lower Reynolds number and Oswald efficiency factor [49]. Therefore, increasing a wing's aspect ratio by increasing its span is a promising lever to reduce induced drag as it can outweigh the negative effects associated with a deviation of an ideal elliptical lift distribution [48], a principal first described by Prandtl in 1933 [50]. The present study follows this approach, aiming to reduce the induced drag of a wing by increasing its aspect ratio to improve overall aircraft performance.

Increasing the span is among the most effective approaches for reducing induced drag. However, alternative techniques, such as wingtip devices, have yielded comparable benefits to span extensions, albeit encountering similar drawbacks, such as a higher wing root bending moment [51–53]. The concept of wingtip devices has been proposed for a considerable period [54], with Richard Whitcomb coining the term *winglet* following a series of experimental evaluations of various designs at NASA Langley in 1976 [55]. A version of a wingtip device, known as *sharklet*, is currently used on the Airbus A320neo, enabling fuel savings of up to 3.5% per flight [56]. Various wingtip device configurations continue to be developed, with Demasi et al. [57] providing a comprehensive review of existing concepts and evaluating their aerodynamic efficiency. Additionally, optimising parameters such as taper ratio, twist, and dihedral angles has been shown to provide improvements to induce drag, although on a smaller scale [41].

Despite their benefits, wings with higher aspect ratios present their own set of engineering challenges. The wingspan is a critical factor in ground operations, and it is constrained by the standardised dimensions of aprons and taxiways. Increasing an aircraft's wingspan may result in a reclassification into a different category concerning compatibility with ICAO airport apron constraints (e.g., ICAO Aerodrome Code C: maximum wingspan of 36 metres vs. ICAO Aerodrome Code D: maximum wingspan of 52 metres [58]). This reclassification can lead to a reduced number of available parking slots or, in some airports, none at all [59]. While the present study does not address this constraint in depth, there has

been proposed solutions in literature, including morphing wings [60, 61] and folding wingtips [62–65], such as the ones present in the Boeing 777X [66].

Instead, this study examines the structural weight implications of increased span. A larger span results in a higher structural weight, not only because the wing itself incorporates additional material due to its larger area, but also due to the increased wing root bending moment associated with higher aspect ratios, which leads to structural reinforcements in the wing root region [46].

Composite materials play a crucial role in addressing these challenges by mitigating the weight penalties associated with increased span through their high stiffness and strength-to-weight ratios, and easiness to enable aeroelastic tailoring and passive load alleviation [67]. These materials are currently used in commercial aircraft wings, with the Airbus A350 XWB and Boeing 787 Dreamliner incorporating up to 50% composite materials by structural weight [68]. Their advantages have also been extensively studied in academic research [69–72]. Notably, in a gradient-based aerostructural optimisation study, Kennedy and Martins [73] compared metallic and composite aircraft wings, demonstrating that the superior strength-to-weight ratio of composite materials enabled wingspans up to 6% greater than those of their metallic counterparts. Furthermore, composite structures were found to be 34% to 40% lighter, resulting in fuel savings of approximately 5% to 8%.

The trade-off between induced drag and structural weight in high aspect-ratio wings has long been recognised. In 1950, Jones [74] investigated this relationship, concluding that a 15% reduction in induced drag could be achieved by increasing the span by 15%, for a fixed wing root bending moment. While induced drag varies inversely with the square of the span, wing bending weight scales approximately with the cube of the span [43]. Therefore, beyond a certain point, the additional structural weight negates the benefits of reduced drag. Due to these trade-offs, the elliptical lift distribution does not yield the optimal aerostructural solution for wing design, as illustrated in Figure 2.3. To accurately reflect overall wing performance, both structural and aerodynamic aspects must be considered.

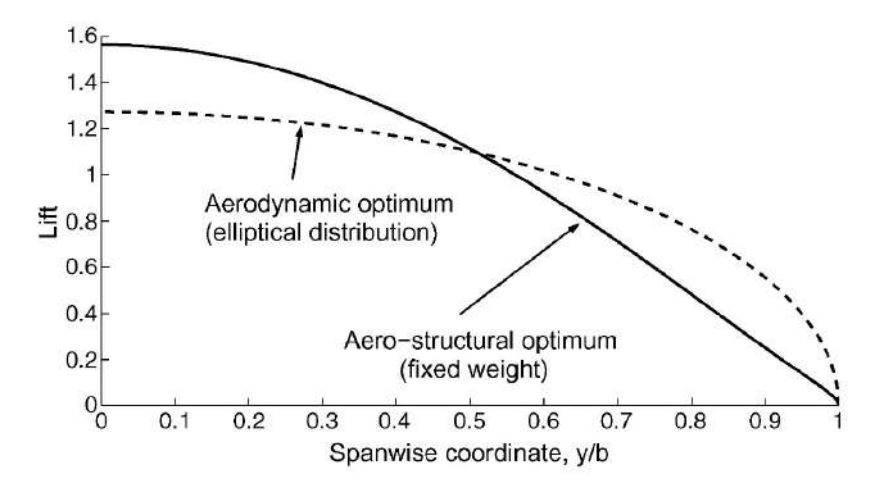


Figure 2.3: Elliptic and aerostructural optimum lift distribution [75].

It is clear that the relation between aspect ratio and wing performance is not solely an aerodynamic issue but a multidisciplinary design problem. Depending on the objective, the optimal performance can be more complex than the classical elliptical lift distribution, requiring a realistic representation of wing

structural behaviour, the consideration of multiple structurally critical design points and constraints, and the incorporation of composite materials. Furthermore, induced drag can be significantly affected by flow condition changes due to deformations on the wing structure, necessitating the consideration of aeroelastic effects. Therefore, high-fidelity analysis and multidisciplinary optimisation tools are essential for investigating the trade-offs associated with increasing the aspect ratio [43].

2.4 Numerical Optimisation

The traditional design process entails manually adjusting parameters to optimise specific performance metrics. In contrast, modern approaches leverage numerical optimisation algorithms to automate this process, enabling a more systematic and efficient exploration for optimal parameter combinations. This automation is particularly beneficial when the number of design variables or their interactions become excessively complex.

A numerical optimisation problem can be expressed as the minimisation of an objective function, also referred to as a cost function or figure of merit, with respect to a vector of design variables, while satisfying a set of constraints. The objective and constraint functions may depend directly on the design variables and on the state of the physical system, which is determined by solving the system's governing equations. Mathematically, the general numerical optimisation problem can be formulated as [76, 77]

$$\min_{m{x}} \quad f(m{x},m{y})$$
 subject to $m{g}(m{x},m{y}) \leq 0$
$$m{y} = m{y}(m{x})$$
 $m{x}_{\mathsf{lower}} \leq m{x} \leq m{x}_{\mathsf{upper}}$.

In this formulation, the objective function f represents the performance metric to be optimised and may be linear or non-linear. In a constrained optimisation problem, the vector g encompasses the criteria that must be satisfied to ensure a feasible solution. A constraint is considered active if it directly influences the optimal solution by being exactly satisfied; otherwise, it is said to be inactive. The performance metric and constraints are typically determined from system responses, referred to as state variables g, which are obtained by solving the governing equations. The vector g denotes the design variables, which typically influence both the objective function g and the constraint model g, either directly or through their effect on the state variables g. These design variables represent the parameters that can be freely adjusted within the optimisation process and are subject to upper and lower bounds, thereby defining the design space. Design variables may be continuous or discrete. The notation convention adopted herein uses non-boldface for scalars, boldface lowercase for vectors, and boldface uppercase for matrices.

The feasible domain within the design space consists of all solutions that satisfy the given constraints and can be obtained using permissible combinations of design variable values. The numerical optimisation problem aims to identify a feasible solution that minimises the objective function.

2.5 Multidisciplinary Design Optimisation

Multidisciplinary design optimisation is an engineering field that uses numerical optimisation techniques to design systems involving multiple disciplines [76]. MDO is of fundamental importance in the design of multidisciplinary systems, such as aircraft, where overall performance is driven not only by the performance of individual disciplines but also by the intricate interactions between them. In such design problems, both the objective and constraint functions are typically defined from responses of multiple analysis disciplines, wherein the outputs of one discipline affect and are, in turn, influenced by the others. As a result, the different disciplines are inherently interdependent, requiring the outputs of one discipline as inputs for another [77].

Although this interdependence is sometimes disregarded by performing single-discipline optimisations, accounting for these interactions provides a more accurate representation of system behaviour and ultimately leads to superior optimisation outcomes, as the combination of individually optimised disciplines does not necessarily result in the best optimised overall system. This issue becomes particularly significant when the disciplines involved exhibit strong coupling [78, 79].

In aircraft design, strong multidisciplinary coupling is inherent, particularly in the context of static aeroelasticity addressed in this thesis. Static aeroelasticity accounts for interactions between structural and fluid mechanics, necessitating a multidisciplinary approach to achieve an optimal design [77, 80].

2.5.1 Optimisation Algorithms

In MDO, the design variables are controlled by an optimisation algorithm that searches for the optimum of the objective function. A wide variety of optimisation algorithms exist, each with distinct advantages and requirements. These algorithms can be classified based on their approach to exploring the design space and the information they require. Broadly, they can be classified into two main categories: stochastic and deterministic [76, 77].

Stochastic Algorithms

Stochastic algorithms use semi-random techniques to adjust the design variables, leading to different optimisation results even when starting from the same initial conditions and settings. These algorithms do not rely on a search direction to determine the next iteration design variables, using only objective function information. Because of this, they are zeroth-order methods, meaning no gradients are computed. Since they do not depend on gradient information, stochastic algorithms are less likely to become trapped in local optima and have a greater probability of locating the global optimum. Additionally, as no sensitivity information is required, the smoothness and continuity of the design space are not critical, making these methods well-suited to handle discrete variables. Their primary limitation is that, as the number of design parameters increases, the number of function evaluations required to reach the optimum grows exponentially, rendering these methods computationally impractical for large-scale problems [46, 81].

Examples of such methods include ant colony, particle swarm, neural networks, simulated annealing, and genetic algorithms. Bras et al. [82] utilised an Ant Colony Optimisation (ACO) method to perform Topology Optimisation (TO) on the cross-section of a wingbox. This study highlighted the capability of the ACO methods to handle discrete problems and non-differentiable objective functions.

A study by Henderson et al. [83] explored trade-offs in aircraft design, focusing on environmental metrics such as fuel burn and $NO_{\rm X}$ emissions, while minimising direct operating costs. The design variables considered included aircraft geometry, engine parameters, and cruise settings. Given that the design space contained numerous local minima and exhibited discontinuities, a particle swarm optimiser was used for single-objective optimisations, whilst multi-objective optimisations were performed using a genetic algorithm. The optimised aircraft for minimum fuel burn and $NO_{\rm X}$ emissions exhibited a high aspect-ratio wing with reduced induced drag.

Furthermore, a study by Wu et al. [84] used a neural network-based response surface model in conjunction with a genetic algorithm to optimise the internal structural layout of a high aspect-ratio composite wing. The optimisation considered web positioning, and the thickness and stacking sequence of the skin. The final optimised design achieved a 146% improvement in the strength-to-weight ratio.

Deterministic Algorithms

Deterministic algorithms, unlike stochastic methods, always converge to the same optimum when initialised from identical starting conditions and settings. These algorithms can be further classified based on the order of function information they utilise: gradient-free (zeroth-order) methods rely only on function values, first-order methods additionally compute first-order derivatives with respect to the design parameters, and second-order methods incorporate second-order sensitivity information. Examples of these different order methods include the simplex algorithm, the steepest descent method, and the Sequential Quadratic Programming (SQP), respectively [76, 77]. The principal advantage of gradient-based methods is their ability to converge with significantly fewer function evaluations. This makes them particularly suitable for large-scale problems involving numerous design variables and constraints. However, the effectiveness of these methods depends on the availability of high-quality gradient information, which requires smooth and continuous functions. Furthermore, these methods only guarantee convergence to a local optimum rather than the global solution [46, 81].

In [14], Kenway and Martins present a multipoint high-fidelity aerostructural optimisation of a transonic aircraft. The Sparse Nonlinear Optimiser (SNOPT) gradient-based algorithm [85], which is based on a SQP approach for constrained non-linear optimisations, was utilised. The optimisation considered wing planform, aerofoil shape, and structural thickness parameters, encompassing a total of 476 design variables. The optimisation resulted in a 4.2% reduction in take-off gross weight and an 11.2% decrease in fuel burn, and demonstrated the computational efficiency of gradient-based methods for high-fidelity aerostructural optimisations involving hundreds of coupled design variables.

Deinert, in his PhD dissertation [46], developed a framework for multidisciplinary shape and sizing optimisations. The gradient-based Non-Linear Programming by Quadratic Lagrangian (NLPQL) algo-

rithm [86] was selected as the optimisation algorithm for the framework. Deinert successfully applied the framework to an industrial-scale wing optimisation. The optimisation had the Breguet range as the objective function and accounted for shape, trimming, and structural sizing design variables, totalling over 1,700. The constraint criteria included von Mises stresses, skin buckling, and flight mechanical trim, amounting to approximately 26,000 constraints. As a result of the optimisation, the wingspan was increased and the planform adjusted, leading to an 8% increase in the Breguet range.

Optimisation Algorithm Selection

Selecting the most appropriate optimisation algorithm requires an assessment of the design problem at hand. For problems with a limited number of design variables that exhibit multiple local minima or discontinuities, zeroth-order methods are preferable. Conversely, problems with a large number of design variables and smooth design spaces favour gradient-based optimisation algorithms.

In this thesis, the design problem is a aeroelastic structural sizing optimisation. The design variables used are continuous and include thicknesses and cross-sectional areas of wingbox structural components, totalling approximately 3,000. Moreover, to ensure structural integrity, a substantial number of constraints is imposed, as these are defined on an element-wise basis across multiple load cases, numbering around 200,000. The functions are expected to be reasonably smooth and continuous, making gradient computations feasible. Additionally, due to the strong coupling between the aerodynamic and structural disciplines, the computational cost of the aeroelastic analysis may be substantial. Therefore, an optimisation algorithm requiring as few system evaluations as possible is preferred.

Based on these considerations, a second-order gradient-based deterministic optimisation algorithm was selected for this work, specifically the NLPQL [86], which is already integrated in the Lagrange MDO suite. The NLPQL is a modified version of the SQP algorithm for non-linear problems. It uses an active-set strategy to limit the number of constraints considered in the sensitivity analysis, thereby lowering the computational cost. Furthermore, the Broyden-Fletcher-Goldfarb-Shanno (BFGS) method [76] is used to iteratively approximate the second-order derivative information required by the NLPQL algorithm.

2.5.2 Sensitivity Analysis

Sensitivity analysis is the study of how the outputs of a model change in response to changes in its inputs. Computing the sensitivities in gradient-based optimisations can often be the most computationally expensive step in the optimisation cycle. Consequently, selecting an appropriate method to compute the derivatives, taking into account the trade-off between computational cost and accuracy is of crucial importance for an efficient optimisation process.

Several methods are commonly used in aircraft design to estimate sensitivities, each with its own advantages and limitations. These include finite-difference, complex-step, automatic differentiation, and semi-analytic methods [77]. In [87], Martins et al. present a comprehensive review and comparison of all existing discrete methods for computing derivatives of computational models, introducing a unified mathematical framework from which all these methods can be derived.

Finite-Difference Method

The Finite-Difference (FD) method is the most basic approach to estimate the derivatives of functions. For each design variable, the design is perturbed and analysed to determine the new value of the objective function. The derivative is then estimated by taking the difference between the outputs and dividing by the value of the perturbation [87]. This method is based on the Taylor series expansion of the function f(x) around a given point x,

$$f(x + \Delta x) = f(x) + \Delta x \frac{\partial f(x)}{\partial x} + O(\Delta x^2).$$
 (2.8)

By rearranging this expansion, one can derive various finite-difference formulas for approximating the derivative, such as the forward-difference formula,

$$\frac{\partial f}{\partial x} \approx \frac{f(x + \Delta x) - f(x)}{\Delta x} + O(\Delta x)$$
. (2.9)

While the FD method is easy to implement and widely used, it is not very accurate and is computationally expensive for problems with a large number of design variables. This is because the method requires evaluating the function f(x) multiple times for each design variable, making it impractical for large-scale optimisation problems [77]. Additionally, the accuracy of the FD method is sensitive to the choice of the perturbation step size Δx , which can lead to numerical issues such as truncation or cancellation errors if not chosen carefully [88]. The great advantage of finite differences is that only discrete function evaluations are required for differentiation, so it can be applied even if the mathematical relations are unknown or unavailable, as is the case with commercial software. Many gradient-based optimisation algorithms use finite-differences by default [89].

Complex-Step Method

The complex-step derivative approximation computes derivatives of real functions using complex variables. The complex-step method is an alternative to the finite-difference method, maintaining its simplicity while being much more accurate. This approach uses a small imaginary perturbation $i\Delta x$, instead of a real perturbation, to calculate the derivative. The Taylor series expansion for the complex-step method is given by [77]

$$f(x+i\Delta x) = f(x) + i\Delta x \frac{\partial f(x)}{\partial x} + O(\Delta x^2).$$
 (2.10)

By taking the imaginary part of both sides and dividing by Δx , the derivative is approximated as

$$\frac{\partial f}{\partial x} \approx \frac{\text{Im}[f(x+i\Delta x)]}{\Delta x} + O(\Delta x^2)$$
 (2.11)

This method allows for an arbitrarily small step size without the issue of subtractive cancellation errors since it does not perform any subtractions. Furthermore, it is relatively straightforward to implement, even in legacy codes, and, once integrated, it remains easy to maintain [90]. However, its computational

cost remains proportional to the number of design variables and the solver's code must support complex arithmetic, which, when used, may lead to increased solver run times.

Martins et al. [91] provide a comprehensive overview of the complex-step derivative approximation and its automated application to numerical algorithms. Several improvements to the fundamental method are proposed. The complex-step method is applied to two multidisciplinary solvers, and the resulting sensitivities are shown to be step-size insensitive and as accurate as the underlying analyses. Furthermore, in [92], Martins establishes that the complex-step method is equivalent to the forward mode of automatic differentiation, which is discussed in the following section.

Automatic Differentiation

Automatic Differentiation (AD) is a highly accurate and efficient technique for computing exact derivatives by systematically applying the chain rule. This method automatically differentiates a given algorithm by adding source code to compute the required sensitivities. AD can be implemented in two modes: forward and reverse mode. In forward mode, the sensitivity of a single independent variable is propagated through the chain rule computational steps. This approach is efficient when differentiating multiple functions with respect to a single parameter but becomes computationally prohibitive when dealing with a large number of design variables. Conversely, in the reverse mode, the function is first evaluated, after which the computations proceed backwards to the independent variables. Reverse mode is independent of the number of design variables; however, it requires storing intermediate variables during the solution process, which can lead to high memory demands for large-scale problems [77].

One of the primary advantages of AD is its ease of implementation. To leverage this advantage, a highly efficient hybrid approach combining AD with the adjoint method, which is introduced in the next section, has been proposed in the literature. This approach, known as the *ADjoint*, selectively applies the reverse mode of AD to differentiate only the code responsible for computing the necessary partial derivatives required by the adjoint method. The ADjoint has been demonstrated to be both effective and computationally efficient by Mader et al. [93] and Marta [94, 95].

Semi-Analytic Methods

Semi-analytical methods are widely recognised as the most accurate and efficient approach to sensitivity analysis. However, they are inherently more complex than the alternative methods presented, as they require an understanding of both the governing equations and the numerical algorithms used to solve them [77].

As outlined in Section 2.4, the functions of interest and the constraints generally depend not only on the design variables, but also on the physical state of the system. These state variables are obtained by solving the governing equations of the system for a given vector of design variables, thereby establishing the dependence of the system state on the design variables,

$$\mathcal{R}(x, y(x)) = 0. \tag{2.12}$$

To compute the total sensitivities of the function of interest with respect to the design variables, the chain rule is applied

$$\frac{df}{dx} = \frac{\partial f}{\partial x} + \frac{\partial f}{\partial y} \frac{dy}{dx}.$$
 (2.13)

All terms in this total sensitivity equation can be readily computed by varying the denominator and reevaluating the function in the numerator, except for $\frac{dy}{dx}$. Since the governing equations must always be satisfied, the total derivative of the residuals with respect to any design variable must be zero. By applying this condition to Equation (2.12), and rewriting it, we get [96]

$$\frac{\partial \mathcal{R}}{\partial y} \frac{dy}{dx} = -\frac{\partial \mathcal{R}}{\partial x}.$$
 (2.14)

Solving for $\frac{dy}{dx}$ and substituting this back into the total derivative expression yields

$$\frac{df}{dx} = \frac{\partial f}{\partial x} - \underbrace{\frac{\partial f}{\partial y} \left[\frac{\partial \mathcal{R}}{\partial y} \right]^{-1} \frac{\partial \mathcal{R}}{\partial x}}_{\text{If}} . \tag{2.15}$$

This expression can be solved using either the direct or the adjoint method.

In the direct method, $\frac{dy}{dx}$ is solved explicitly from Equation (2.14) and subsequently substituted into the total sensitivity Equation (2.15). However, $\frac{dy}{dx}$ must be computed for each design variable, which can become computationally expensive for large-scale problems [96].

In the adjoint method, an auxiliary adjoint vector, ψ , can be obtained by solving the adjoint equations

$$\frac{\partial \mathcal{R}}{\partial y}\psi = -\frac{\partial f}{\partial y}.$$
 (2.16)

This adjoint vector is then substituted into Equation (2.15) to determine the total sensitivity [96]. Unlike the direct method, the computational cost of the adjoint method is largely independent of the number of design variables and instead depends on the number of functions of interest. Consequently, the adjoint method is particularly advantageous when the number of design variables is significantly larger than the number of functions of interest, whereas the direct method is preferable in the opposite case [77].

The adjoint method has been extended and applied to multidisciplinary coupled sensitivity analysis. In his PhD dissertation, Martins [96] developed and applied the coupled adjoint method to a high-fidelity aerostructural optimisation of a supersonic business jet configuration. This method has also been implemented in some of his other aerostructural optimisations [14, 75, 81]. Conversely, in the aforementioned dissertation of Deinert [46], the coupled direct method was favoured and accordingly applied.

Overall, due to their accuracy and efficiency, the coupled direct and adjoint methods are particularly well suited for the problem at hand, making them the most appropriate choice for the present study. These methods are already implemented within Lagrange [24]. Considering the relationship between the number of functions and design variables, Lagrange automatically selected the coupled direct method as the most suitable approach for sensitivity analysis.

2.5.3 Multidisciplinary Optimisation Architectures

One of the most critical aspects in the implementation of MDO is its organisational strategy, commonly referred to as the MDO architecture. This architecture defines both the manner in which the various analysis and optimisation models are coupled and the approach used to solve the overall optimisation problem. MDO architectures can be classified as either monolithic or distributed. In monolithic architectures, a single optimisation problem is formulated and solved as a whole. Conversely, in a distributed approach, the same problem is decomposed into multiple sub-problems, each containing a smaller subset of local variables and constraints, with coupling and coordination between sub-problems being ensured by a system-level optimiser [77, 97]. Airbus's MDO suite, Lagrange, employs a monolithic architecture, specifically the Multidisciplinary Feasible (MDF) formulation.

The MDF architecture operates similarly to a conventional single-discipline optimisation, wherein all disciplines are coupled to form a single multidisciplinary analysis module. In MDF, the optimiser minimises the constrained objective function by controlling the design variables, whereas the state and coupling variables are determined through the solution of a multidisciplinary analysis at each iteration. Therefore, consistency is ensured at the analysis level, with a Multidisciplinary Design Analysis (MDA) iteratively solving the governing equations across all disciplines until the coupling variables have converged. Once the MDA has converged, the objective and constraint functions are reevaluated, after which the optimiser updates the design variables and commences another iteration [77, 97]. To illustrate the organisational strategy, data dependencies, and process flow among the components of the MDF architecture, its eXtended Design Structure Matrix (XDSM) diagram [98] is presented in Figure 2.4.

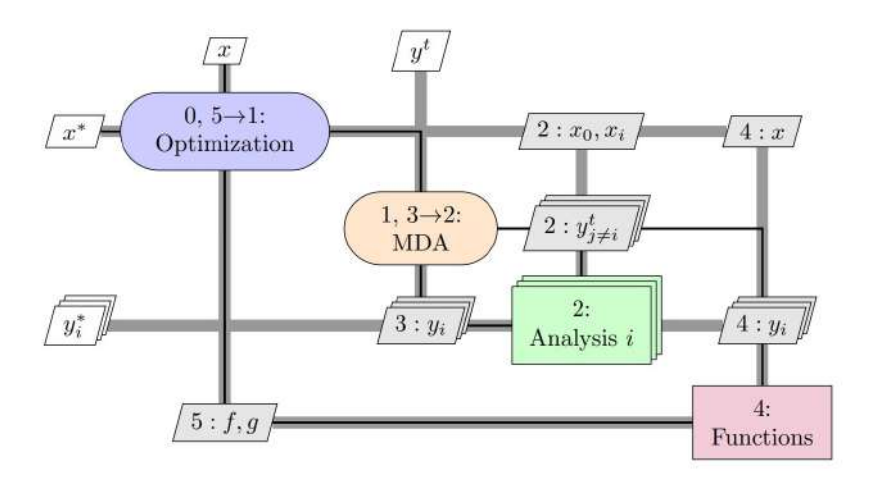


Figure 2.4: XDSM diagram for the MDF architecture [99].

A fundamental advantage of the MDF formulation is that each optimisation iteration inherently satisfies multidisciplinary feasibility. Consequently, even if the optimisation process is prematurely terminated, the resulting system design remains physically compatible. However, it is not guaranteed that all optimisation constraints will be satisfied. Furthermore, when addressing strongly coupled problems, MDF reduces the problem dimensionality compared to alternative architectures. Additionally, by treating the coupled discipline analysis as a single monolithic system, MDF facilitates the use of well-established single-discipline optimisation techniques [77, 97].

Nevertheless, MDF has certain drawbacks. The primary limitation is that parallel computation is predominantly restricted to the MDA module, leading to increased computational costs compared to decoupled architectures that exploit parallelism more effectively [100]. Additionally, for gradient-based multidisciplinary optimisations, MDF requires the computation of sensitivities for the entire multidisciplinary system rather than for individual disciplines in isolation [77, 97]. Fortunately, Lagrange's semi-analytic coupled sensitivity analysis techniques effectively mitigate this issue [24].

2.5.4 Multidisciplinary Analysis Methods

The MDF architecture requires multidisciplinary analysis to solve the coupling problem. As the MDA lies at the core of the optimisation process, the adopted approach to solve the multidisciplinary system significantly influences the optimisation's efficiency and robustness.

There are two main approaches for conducting the multidisciplinary analysis of coupled systems: fixed-point-iteration-based methods and Newton-based methods. In fixed-point approaches, each discipline is solved sequentially, keeping the data from the other disciplines fixed when solving for a particular discipline. In contrast, Newton-based approaches update all data and solve all disciplines simultaneously within each iteration of the coupled system [77, 101, 102]. In this work, for both the structural sizing optimisation and aircraft performance analysis, a fixed-point approach, specifically the Gauss-Seidel method, is used to solve the aerostructural analysis problems.

When solving the MDA problem with the Gauss-Seidel method, each analysis is executed sequentially, using the most recent outputs from the other analyses as soon as they become available. Due to the sequential nature of the Gauss-Seidel method, parallel evaluation of disciplines is not possible, however, changing the order in which the disciplines are solved and under-relaxation methods can improve the convergence rate [101, 102]. In Figure 2.5, the XDSM diagram for a MDF architecture with a Gauss-Seidel multidisciplinary analysis involving three analysis disciplines is presented.

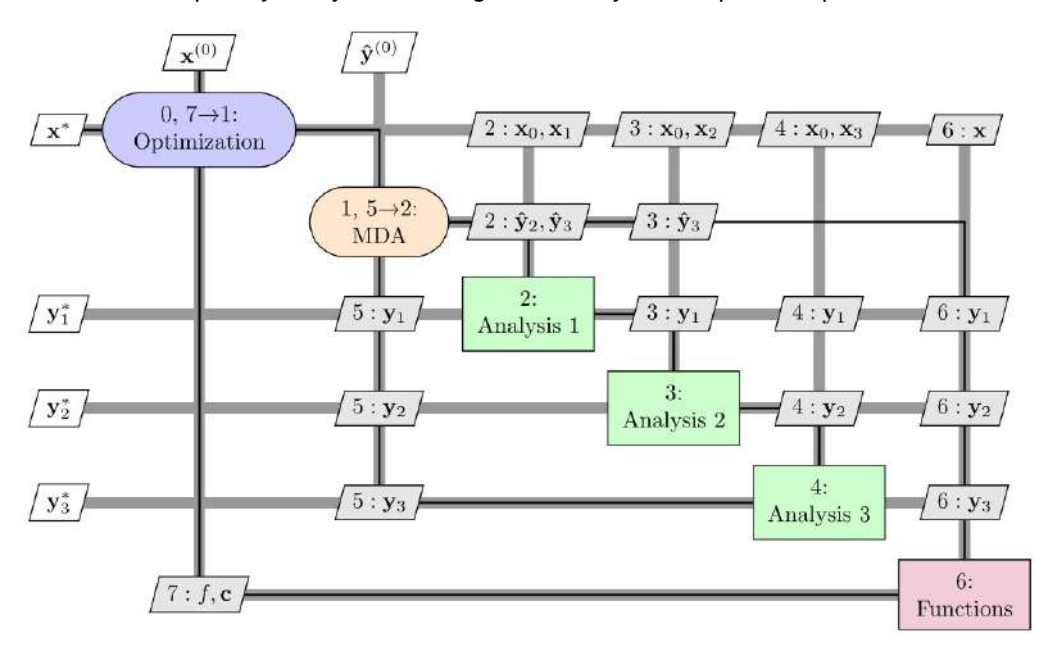


Figure 2.5: XDSM diagram for a MDF architecture with a Gauss-Seidel multidisciplinary analysis [97].

Chapter 3

Structural Sizing Framework for Minimum Mass

This chapter provides a detailed description of the structural sizing optimisation process for mass minimisation. First, an overview of the optimisation workflow is presented, along with the software used. Subsequently, the procedure for generating the parametric geometry model of the aircraft is described, including its node mapping and mesh morphing capabilities. This is followed by an examination of the approach adopted to solve the optimisation problem and its aeroelastic analysis. Finally, the analysis models and the structural sizing criteria and requirements are detailed. All structural sizing activities conducted in this work adhere to the methodology outlined in this chapter.

3.1 Structural Sizing Workflow

The established process for aeroelastic structural sizing optimisation incorporates two proprietary Airbus Defence and Space tools: Descartes and Lagrange. Additionally, commercially available software, such as Altair HyperMesh® and HyperView®, are used for pre- and post-processing tasks.

Descartes [18, 103] is a pre-processing tool capable of generating a parametric aircraft geometry model. This model provides the necessary input data for the optimisation process, including structural and aerodynamic models, as well as the optimisation model itself. Descartes is specifically tailored for aircraft design applications.

Lagrange [23, 24] is a MDO suite embedded with a structural finite element solver. Thus, it unifies two optimisation components in one: an optimisation framework and an analysis method. Lagrange can execute aeroelastic analysis and structural sizing optimisations. It uses the NASTRAN® format for its input files, ensuring compatibility with any NASTRAN®-supported pre-processor, such as Altair HyperMesh®. In addition to generating text-based output files, Lagrange produces results that can be visualised in Altair's HyperView® post-processor.

Lagrange supports a broad range of system analyses, including steady and unsteady (flutter and gust) aeroelastic simulations, gradient-based optimisation algorithms, and sensitivity analysis methods,

including fully coupled analytical sensitivity computations [24]. Furthermore, it allows for both shape and sizing optimisation variables and stringent constraints, including strength, buckling, manufacturability, as well as other criteria. Lagrange also integrates various linear aerodynamic analysis tools for aeroelastic analysis and automates the iterative load analysis and structural sizing loop process. For a more detailed overview of Lagrange's capabilities, refer to [23].

The aeroelastic structural sizing optimisation process begins with the generation of a parametric geometry model using Descartes. From this parameterised geometry, the aerodynamic, structural, and optimisation models are derived. Additional pre-processing tasks are carried out using Altair HyperMesh[®]. Subsequently, Lagrange conducts the structural sizing optimisation ensuring that the aircraft satisfies structural integrity requirements. This process results in an optimised aircraft design. At the core of this optimisation lies an aeroelastic analysis. The overall aeroelastic structural sizing optimisation process is illustrated in Figure 3.1.

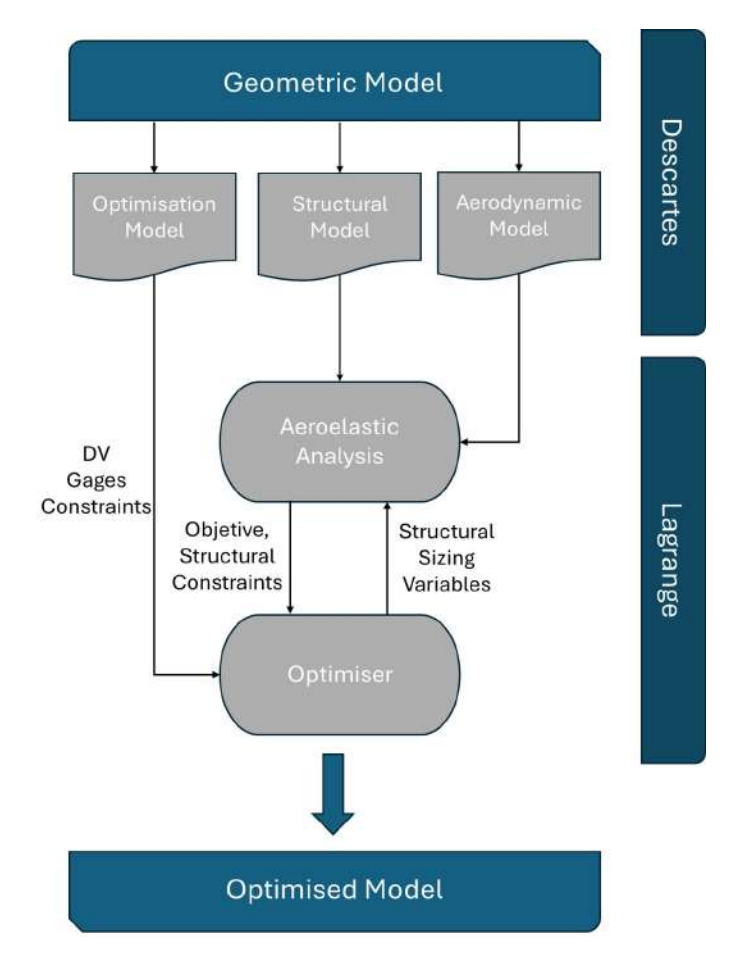


Figure 3.1: Aeroelastic structural sizing optimisation process.

3.2 Parametric Geometry Model

The aircraft's geometry model is generated in Descartes with a parametric approach. A parameterised geometry model is particularly advantageous as it enables rapid updates to the geometry, analysis and optimisation models in response to shape variations, such as an increase in wingspan.

Descartes uses the *Common Parametric Aircraft Configuration Scheme* (CPACS) [19–22] to generate the geometry model. CPACS uses the XML data format to parametrically describe the complete aircraft and serves as a centralised database for aircraft design, facilitating the exchange of data across various disciplines. In addition to data for the geometry, the database includes metadata for the analysis models such as materials, skin thickness, system masses, fuel tanks, amongst other information. CPACS is developed by the DLR under an open-source licence [19].

Within the CPACS data scheme, the positions of structural components are defined relative to the wing's coordinate system. The spanwise parameter, denoted by η , ranges from $\eta=0$ at the start of each wing segment to $\eta=1$ at the end. Similarly, the chordwise direction is represented by ξ , which starts at $\xi=0$ at the leading edge of the aerofoil and ends at $\xi=1$ at the trailing edge [104], as illustrated in Figure 3.2.

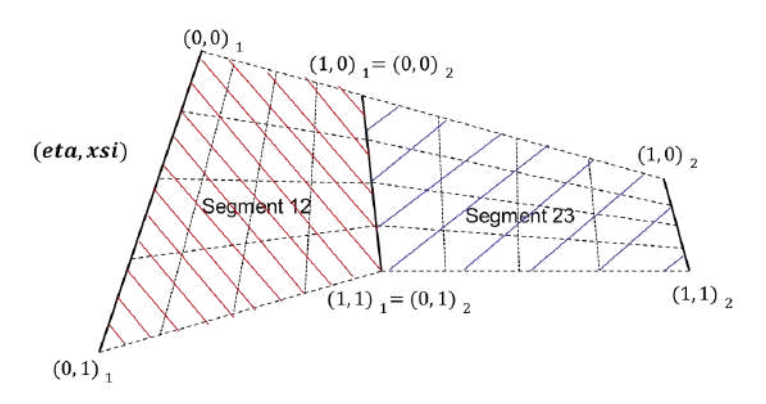


Figure 3.2: CPACS parametric notation for a wing structure [104].

Therefore, by using a parameterised geometry model in CPACS, Descartes can automatically update the positions of structural components when a shape variation occurs, as these components are always positioned relative to the wing geometry. This will minimise the construction effort required to generate a higher aspect-ratio aircraft geometry from a baseline model.

From the parametric geometry model, combined with the stored metadata, Descartes generates the structural, aerodynamic, and optimisation models necessary for the structural sizing optimisation. As a central geometry model is the basis for generating all analysis models, consistency between disciplines is secured [13, 18].

Once generated, these analysis models are linked to the parametric geometry through node mapping. In this process, the nodes of the analysis models are projected onto the surface of the geometry model, as seen in Figure 3.3, and their relative coordinates are stored. If the wing geometry is modified, the established mapping between the geometry and the simulation models enables the morphing of the analysis meshes by rapidly updating the absolute node coordinates to reflect the shape changes, rather than requiring a complete remeshing. In the morphed analysis meshes, the number of elements, nodes, and their connectivity, remains unchanged with only the absolute grid point coordinates being updated [18, 103].

Mesh morphing is not possible if the wing geometry undergoes topological changes. Additionally, if through morphing the quality of the analysis mesh degrades to a point where reliable results cannot be

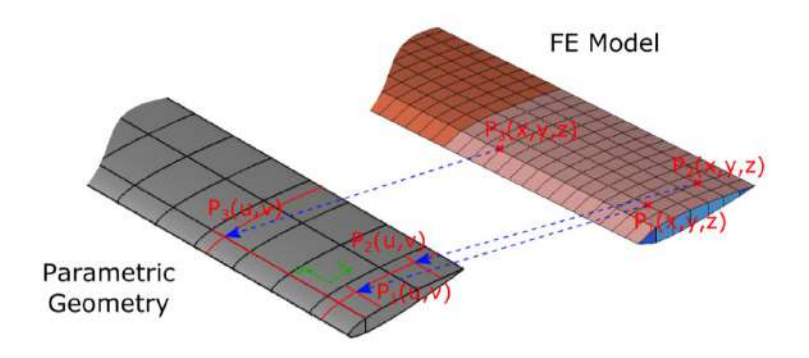


Figure 3.3: Node mapping of a finite element structural model to a parametric geometry [46]. guaranteed, remeshing should be performed [13], as seen in Figure 3.4.

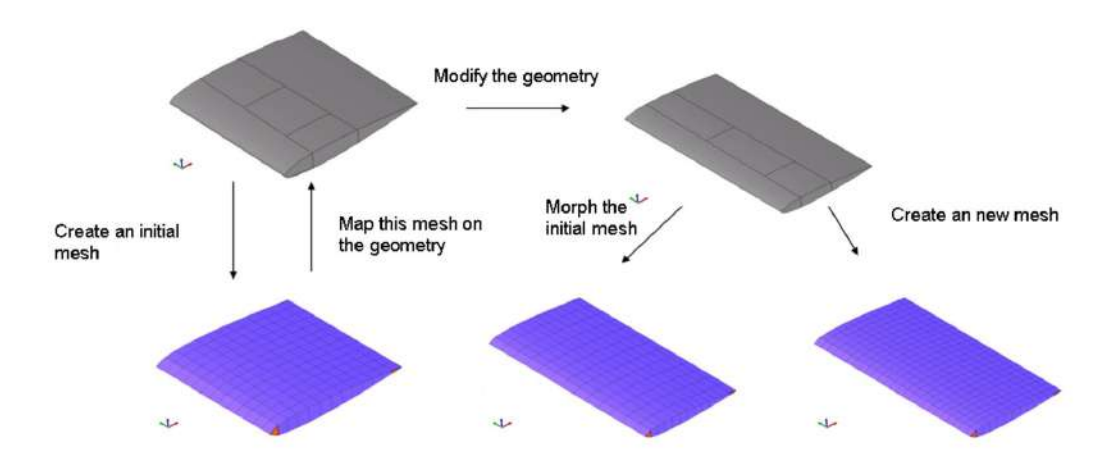


Figure 3.4: Remeshing or morphing of a modified parametric geometry [13].

The capabilities of Descartes to create all necessary models for structural sizing directly from a parametric geometry model, and to seamlessly accommodate shape modifications to the wing geometry and perform the corresponding morphing of the analysis models, are of particular importance to this work. These capabilities will be used to generate the geometry of a higher aspect-ratio aircraft from its baseline configuration, and to attempt the morphing of its analysis models. However, some challenges were encountered as will be discussed in Chapter 5.

3.3 Aeroelastic Analysis and Optimisation

For an accurate structural sizing it is crucial to account for aeroelastic effects. Aeroelasticity concerns the interaction between aerodynamic loads and elastic structural deformations. The pressure distribution generated by airflow over an aircraft's surface creates loads that deform the elastic structure. This deformation, in turn, changes the airflow and generates a new pressure distribution, as seen in Figure 3.5, creating a feedback loop.

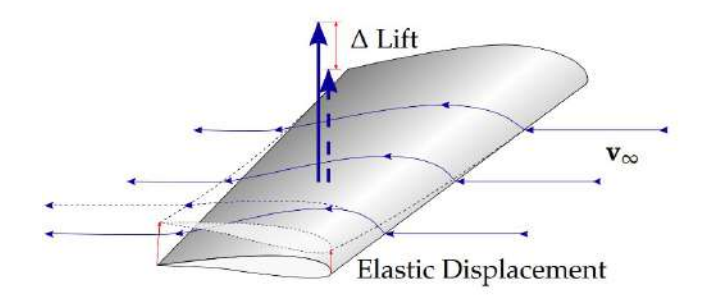


Figure 3.5: Interaction between aerodynamic forces and structural elasticity [46].

Aeroelastic phenomena are broadly classified into two categories: static and dynamic. Static aeroelasticity deals with the interaction between aerodynamic and elastic forces, influencing the load distribution and phenomena such as divergence. Dynamic aeroelasticity, on the other hand, incorporates inertial forces in addition to aerodynamic and elastic forces, encompassing phenomena such as flutter and buffeting [105]. This study focuses on static aeroelasticity, particularly its effects on load distribution.

The approach to solve the aeroelastic structural sizing problem used in this work involves two nested loops: an internal aeroelastic analysis loop and an external structural sizing optimisation loop [106].

Aeroelastic Analysis

The structural sizing process begins with an aeroelastic analysis. Initially, the aerodynamic problem is solved based on the rigid flight state without any effects of elasticity. The computed aerodynamic loads are subsequently interpolated, at the fluid-structure interface, to the unloaded structural model. Based on these aerodynamic loads, Lagrange solves the structural problem, determining the elastic displacement. These structural deformations are then applied to the aerodynamic model, altering the lift distribution on the wing. This new aerodynamic solution will then be applied to the structural model, starting over the loop, which runs iteratively until convergence is achieved. After the coupling has converged, the structural constraints are evaluated.

Structural Sizing Optimisation

After the aeroelastic analysis converges, the structural constraint violations, and the aircraft mass, which can be directly obtained from the structural model without additional calculations, serve as input for the optimiser. The optimiser explores the design space by varying the design variables, specifically the thicknesses and cross-sectional areas of the structural elements, with the goal of minimising the aircraft mass. This process modifies the weight and stiffness distribution, thereby altering the loads acting on the wing. These changes lead to a restart of the loads model loop, described above, using the updated structural model. This external structural sizing optimisation loop is also iterative. The XDSM diagram for the structural sizing optimisation for minimum mass is illustrated in Figure 3.6.

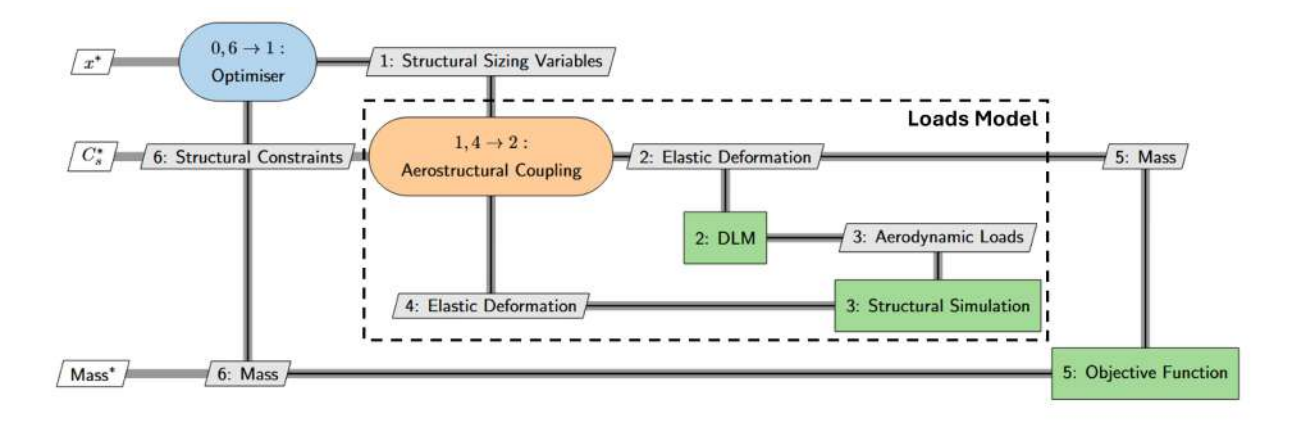


Figure 3.6: Structural sizing optimisation process for minimum mass.

3.4 Aeroelastic Analysis Models

Aeroelastic analysis is central to the structural sizing optimisation. Aeroelastic problems can be solved using two primary approaches: the monolithic (tightly coupled) approach and the partitioned (loosely coupled) approach.

The monolithic approach simultaneously solves the fluid and structural disciplines within a single computational domain using a unified numerical framework. In this approach, the associated matrices often suffer from ill-conditioning, and existing fluid and structural solvers cannot be used. By contrast, the partitioned approach solves the fluid and structural subdomains separately, leveraging existing specialised solvers tailored to each discipline. Since each discipline has its own computational domain, different levels of fidelity and discretisation can be used depending on the specific needs of the problem. The main challenges of the partitioned approach lie in the exchange of boundary conditions between disciplines and the convergence of the coupled solution [107].

In this study, the partitioned approach was selected, as seen in Figure 3.6, as not only it enables the use of existing specialised solvers for each discipline, but it also allows for different levels of fidelity for each domain. The following sections discuss the selected analysis models, and the coupling method employed between the disciplines.

3.4.1 Aerodynamic Model

In the context of aeroelastic analysis for structural sizing, the primary objective of the aerodynamic model is to provide an accurate representation of the load distribution responsible for the elastic deformation of the structure. Furthermore, the aerodynamic model must be robust and capable of incorporating these elastic deformations. The complexity of the aerodynamic model is directly correlated with the computational cost of aeroelastic analysis and optimisation, as these processes require repeated evaluations of the flow conditions to achieve convergence. Consequently, the selection of an aerodynamic model that balances accuracy and computational efficiency is of paramount importance.

A linear aerodynamic model offers sufficient accuracy in lift load distribution estimates for structural sizing in the preliminary design stage at a relatively low computational cost [46], without compromising

the robustness of the optimisation process. Higher-fidelity models often lack robustness when subjected to the large wingtip displacements induced by the structurally critical loads. In such models, the elastic deformations must be applied not only to the surface mesh but also propagated throughout the entire volume mesh. In contrast, potential flow methods do not pose this issue, as they require meshing only of the aircraft's geometry [32, 108].

Given these requirements, a lattice method was selected as the aerodynamic model for structural sizing, specifically the Doublet Lattice Method (DLM) [109–111], as it is particularly suited to aeroelastic applications. The DLM was first developed as an extension of the Vortex Lattice Method (VLM) [112] to unsteady aerodynamics. This method assumes inviscid and irrotational flow, meaning that viscous effects, turbulence and boundary layer are not modelled, and only lift and induced drag can be accurately computed [44, 108]. The DLM provides a harmonic solution for the unsteady linearised potential flow equations, also referred to as the unsteady Prandtl-Glauert equations [113].

The DLM discretises the lifting surfaces into panels, placing a distribution of doublets of strength Γ at the quarter-chord line of each panel. Additionally, a collocation point lies at the three-quarter chord line, where the boundary condition of zero normal flow is enforced according to Pistolesi's theorem [113], as shown in Figure 3.7.

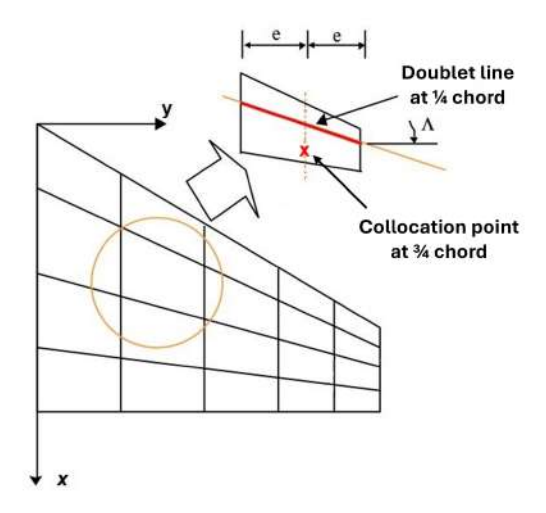


Figure 3.7: Lifting surface idealization in the doublet lattice method (adapted from [114]).

The doublet strengths are determined by enforcing the Neumann boundary condition at the collocation point of each panel, which guarantees flow impermeability. The resulting system of equations is given by [44]

$$AIC \cdot \Gamma = b_c, \tag{3.1}$$

where AIC is the Aerodynamic Influence Coefficient matrix and b_c denotes the boundary conditions. The AIC matrix depends primarily on the model's geometry and Mach number and captures the variations in aerodynamic loads due to deflections in the structure. It is a crucial component of the aeroelastic analysis and, once generated, it can be repeatedly applied to different boundary conditions, altered by elastic deformations, allowing the circulation to be obtained without recalculating the matrix [44].

After computing the doublet strength Γ , the lift force per unit span on each panel L' is calculated using the Kutta-Joukowski theorem [44],

$$L' = \rho v \times \Gamma \,, \tag{3.2}$$

where ρ is the fluid density and v is the undisturbed flow velocity vector.

In this thesis, the DLM mesh is generated from the aircraft geometric model using Descartes [18]. From this mesh, an in-house tool is used to generate the complex-valued AIC matrix once, prior to the structural sizing optimisation process. The AIC matrix is subsequently provided to Lagrange, which incorporates a linear aerodynamic analysis tool [23] capable of computing the aerodynamic loads according to Equations (3.1) and (3.2).

3.4.2 Structural Model

In the context of structural sizing optimisation, the structural model plays a key role in both the aeroelastic analysis, to determine the elastic behaviour of the aircraft, and the optimisation process, to evaluate structural sizing criteria. Therefore, the structural model must accurately represent the aircraft's stiffness and enable the assessment of structural sizing criteria such as strength, stability, and manufacturing constraints.

The response of a structure to an applied load may be linear or non-linear. When the structure behaves linearly, the displacements are proportional to the applied loads, and the material remains within the elastic domain. Non-linearity arises when material plasticity must be accounted for. In this work, it is assumed that the material remains within the elastic domain, and thus the response of the structure to applied loads is described by Hooke's law of linear elasticity as [115, 116]

$$K \cdot u = f, \tag{3.3}$$

where u represents the structure's displacements, f denotes the forces acting on the structural model, and K is its stiffness matrix.

In this work, composite materials are used in the wingbox due to their numerous advantages over metallic alternatives in the design of high aspect-ratio wings, as discussed in Section 2.3. If all fibres within each ply of the composite are parallel, each lamina exhibits orthotropic behaviour. Consequently, Hooke's law, as presented in Equation (3.3), can be simplified as [115, 116]

$$\begin{cases}
\varepsilon_{1} \\
\varepsilon_{2} \\
\varepsilon_{3} \\
\varepsilon_{4} \\
\varepsilon_{5} \\
\varepsilon_{6}
\end{cases} = \begin{bmatrix}
\frac{1}{E_{1}} & -\frac{\nu_{21}}{E_{2}} & -\frac{\nu_{31}}{E_{3}} & 0 & 0 & 0 \\
-\frac{\nu_{12}}{E_{1}} & \frac{1}{E_{2}} & -\frac{\nu_{32}}{E_{3}} & 0 & 0 & 0 \\
-\frac{\nu_{13}}{E_{1}} & -\frac{\nu_{23}}{E_{2}} & \frac{1}{E_{3}} & 0 & 0 & 0 \\
0 & 0 & 0 & \frac{1}{G_{23}} & 0 & 0 \\
0 & 0 & 0 & 0 & \frac{1}{G_{13}} & 0 \\
0 & 0 & 0 & 0 & \frac{1}{G_{13}} & 0 \\
0 & 0 & 0 & 0 & \frac{1}{G_{13}} & 0 \\
0 & 0 & 0 & 0 & \frac{1}{G_{13}} & 0
\end{cases}, \tag{3.4}$$

where σ and ε denote the stress and strain vectors, respectively, E_i is the Young's modulus in the i-direction, ν_{ij} is the Poisson's ratio, and G_{ij} is the shear modulus in the corresponding planes.

Under the assumptions that the composite is initially stress-free, the fibres and matrix are perfectly bonded, both phases exhibit isotropic and linearly elastic behaviour, the matrix is free of voids or cracks, and the fibres are uniformly distributed and parallel, the rule of mixtures can be used, and the properties of each ply are given by [115, 116]

$$E_1 = E_f v_f + E_m v_m$$
, (3.5a) $E_2 = \frac{E_f E_m}{E_f v_m + E_m v_f}$, (3.5b)

$$G_{12} = G_{21} = \frac{G_f G_m}{G_f v_m + G_m v_f},$$
 (3.5c) $v_{12} = v_{21} = v_f v_f + v_m v_m,$ (3.5d)

where E_f and E_m denote the Young's moduli of the fibre and matrix, respectively; ν_f and ν_m denote their Poisson's ratios; and v_f and v_m denote their respective volume fractions.

Once the properties of each ply are determined, the ply stiffness matrix can be computed. With the stiffness matrices of all laminae established, the laminate in-plane, coupling, and bending stiffness matrices are assembled by integrating the contributions of all plies through the laminate's thickness, as outlined in [115].

The governing equations of the structural problem can be solved using various numerical methods, including the Finite Difference Method (FDM), the Finite Volume Method (FVM), and the Finite Element Method (FEM). In this thesis, the structural problem is solved with Lagrange using the FEM, which is widely regarded as the standard approach in modern engineering for simulating elastic structural behaviour. With FEM, the domain is discretised into multiple subdomains known as elements. The solutions to the governing equations, namely the displacements, are computed at the nodes of each element and subsequently interpolated within the elements to obtain the displacement field [117, 118]. From the displacements, several system responses are derived, including strains, stresses, and buckling stability, all of which are essential for evaluating the structural sizing optimisation criteria. Furthermore, the properties of the finite elements can be adjusted during the optimisation process to model variations in thickness or cross-sectional area.

In this thesis, the FE structural model was generated from the geometry model using Descartes' internal meshing functionality [18, 36]. Descartes can generate a mesh within minutes, offering flexibility in selecting parameters such as element type, shape, size, and other options commonly found in commercial software. Various element types are available, such as rod, bar, and shell elements, each with distinct properties and shapes that allow for a more accurate representation of the structure and its physical behaviour. The selection of an element type depends on its capabilities, cost, and accuracy.

In the NASTRAN formulation, one-dimensional elements include the CROD and CBAR elements. The CROD is a two-node element that represents a tension-compression-torsion member. Therefore, its element stiffness matrix contains terms corresponding solely to axial and torsional degrees of freedom. On the other hand, the CBAR element incorporates six degrees of freedom at each node and defines a simple beam. Its formulation is derived from classical beam theory and in addition to axial forces and torques, it can model bending moments and shear forces [119].

In cases, such as aircraft structures, where one dimension, typically the thickness, is significantly smaller than the other two, it is possible to idealise a three-dimensional structure as a two-dimensional representation using shell elements [120]. For linear analysis, NASTRAN shell elements adopt classical thin plate theory assumptions. Examples of NASTRAN shell elements include the CTRIA3, a three-node isoparametric flat plate triangular element, and the CQUAD4, a four-node isoparametric flat plate quadrilateral element, having each six degrees of freedom per node. Shell elements account for bending effects by incorporating rotational degrees of freedom at their nodes [119]. The forces and moments acting on a CBAR element, as well as the degrees of freedom of a CQUAD4 element, are illustrated in Figure 3.8.

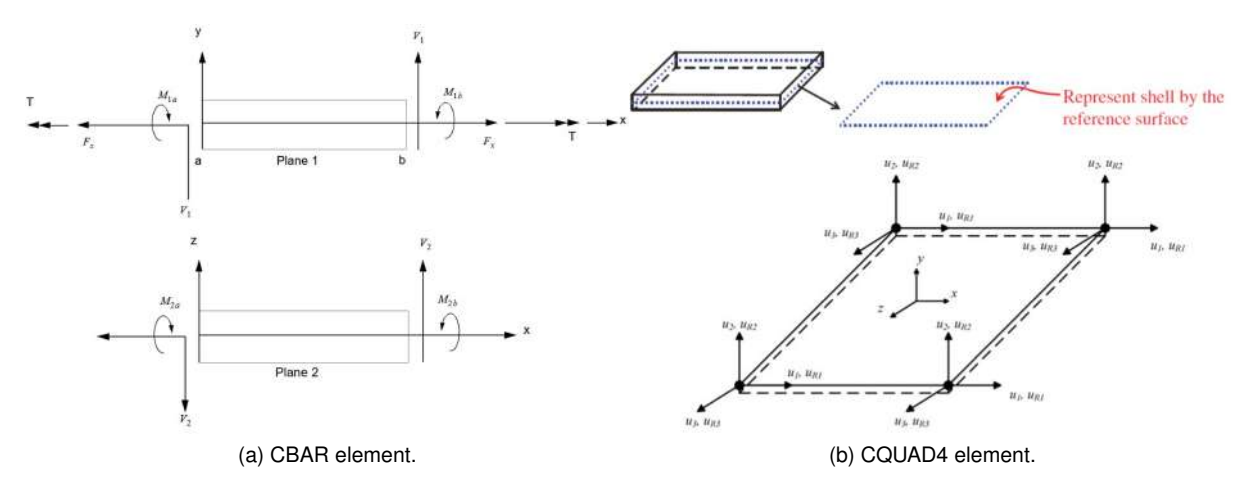


Figure 3.8: Forces and moments acting on a CBAR element [119]; and degrees of freedom of a CQUAD4 element [120, 121].

Due to the detailed nature of the structural sizing, which captures numerous local effects in the constraints, the various aircraft components were modelled as thin-walled shell structures. This allows for an accurate representation of the structure's elastic behaviour, while also enabling the assessment of structural sizing criteria. Specifically, the skin, spar webs, and ribs were modelled using two-dimensional shell elements (CQUAD4 and CTRIA3), while the stringers and spar caps were modelled as one-dimensional elements (CBAR and CROD, respectively) in the NASTRAN formulation. This modelling approach mirrors that used by Schulze et al. [48], as shown in Figure 3.9.

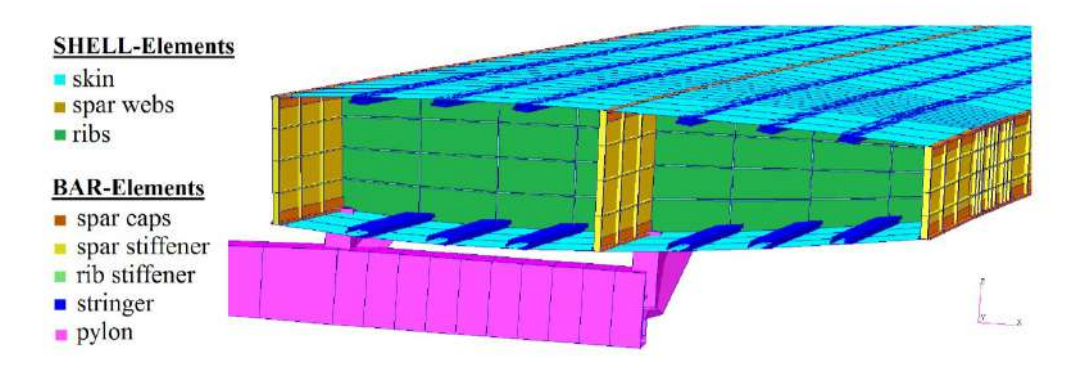


Figure 3.9: Finite element model highlighting the applied elements [48].

Following the mesh generation in Descartes, its quality was assessed using HyperMesh[®]. Elements that failed to meet the established criteria, including aspect ratio, skew angle, and warpage, were manually corrected to ensure the accuracy and reliability of the structural model.

In the structural model, the aircraft's weight can be separated into two components: the structural weight of the composite wing, determined by the size and material properties of its elements, which is to be minimised during structural sizing; and the weight of the fuel, payload, passengers and of the remaining aircraft structure, including engines and pylons. The latter can be represented by a simplification using distributed concentrated mass points (CONM2 elements), connected to the finite element model via Rigid Body Elements (RBEs).

3.4.3 Fluid-Structure Coupling Model

To solve the coupled aerostructural analysis problem, information needs to be iteratively exchanged between the aerodynamic and structural models. Due to the distinct domain discretisation, the meshes at the fluid-structure interface typically do not match, preventing direct information exchange [24]. In this thesis, a coupling model was used in the structural sizing process to interpolate structural displacements to the fluid flow mesh and aerodynamic loads to the structural domain.

In this coupling model, aerodynamic loads and elastic displacements are interpolated through a set of structural nodes strategically positioned at locations capable of adequately withstanding the applied loads. At these points, the interpolation of loads and displacements is performed using the Infinite Plate Spline (IPS) method, as formulated by Harder and Desmarais [122], which is already implemented in Lagrange.

By integrating the aerodynamic and structural domains with the coupling transformation, an iterative solution to the coupled aerostructural analysis problem is possible with Lagrange [23].

3.5 Structural Sizing Criteria and Requirements

A robust criteria model is essential to prevent optimisations from converging on impractical solutions. Structural integrity criteria are crucial not only for ensuring safety and regulatory compliance but also for overall performance. Structural sizing criteria directly influence the aircraft's weight, which, in turn, affects its fuel efficiency. Furthermore, it significantly influences the stiffness of the wing structure, which impacts the aircraft's aerodynamic performance through aeroelastic effects on the wing's in-flight shape.

Adequately addressing the criteria model ensures a balance between structural weight and stiffness, ultimately leading to a more efficient design. The requirements and criteria used for the structural sizing in this work are:

- Strength requirements;
- · Buckling requirements;
- Manufacturing requirements.

These requirements will be briefly detailed below. All criteria used in this work adhered to the recommendations set forth in internal documentation from Airbus Defence and Space and its UPWing partners. The criteria models are embedded within Lagrange and have been previously validated in industrial-scale cases, ensuring that the composite wing structural sizing results in a manufacturable design with realistic weight and stiffness [23].

The structural sizing criteria for the composite wing will focus primarily on optimising the wing covers, as they are the main drivers of aeroelastic tailoring, improving both passive load alleviation and wing cruise drag performance.

3.5.1 Strength Requirements

Strength requirements for typical composite wing structural sizing consider a range of failure modes, each evaluated through distinct analysis methods. In this thesis, to simplify the structural sizing process, a maximum allowable material strain in tension and compression will be imposed as a constraint (Section 6.1.4) [116]. Additionally, the twist at the wingtip is restricted to ensure adequate wing stiffness.

3.5.2 Buckling Requirements

Buckling requirements dictate that the wing covers must not experience buckling below the ultimate load. To prevent buckling from becoming a significant design driver, a minimum stringer and rib pitch were implemented during the design of the geometric model. The skin and spar buckling panels are modelled as bi-axially loaded, simply supported flat plates with anisotropic material properties. The critical buckling loads are determined using the analytical methods proposed by P. M. Weaver [123–125]. The stringer and the attached sheets are modelled as a super-stiffener. The critical buckling strength of the super stiffener is determined using the Johnson-Euler formula [126, 127].

3.5.3 Manufacturing Requirements

To ensure manufacturability of the composite wing after structural sizing, various constraints and requirements regarding thickness and ply share percentages are imposed.

Thickness variations between adjacent wing skin patches are constrained by ramp rate requirements in both the spanwise and chordwise directions. Furthermore, minimum laminate thicknesses are enforced in specific areas of the wing skin to satisfy design requirements. For instance, a minimum thickness is imposed for the upper skin to ensure aircraft safety in the event of a lightning strike, while in the lower skin a minimum thickness is applied due to the risk of tyre debris impact. Additionally, in the vicinity of the engine, for the lower skin, the minimum skin thickness is increased to accommodate the bolted joints of the pylon.

A maximum and minimum ply share percentage requirement is imposed for each ply direction on the wing skin. A continuity constraint limits ply thickness differences between plies of adjacent skin patches to prevent significant local variations in ply shares, as well as ply drops and ply additions, thereby ensuring manufacturability, as seen in Figure 3.10.

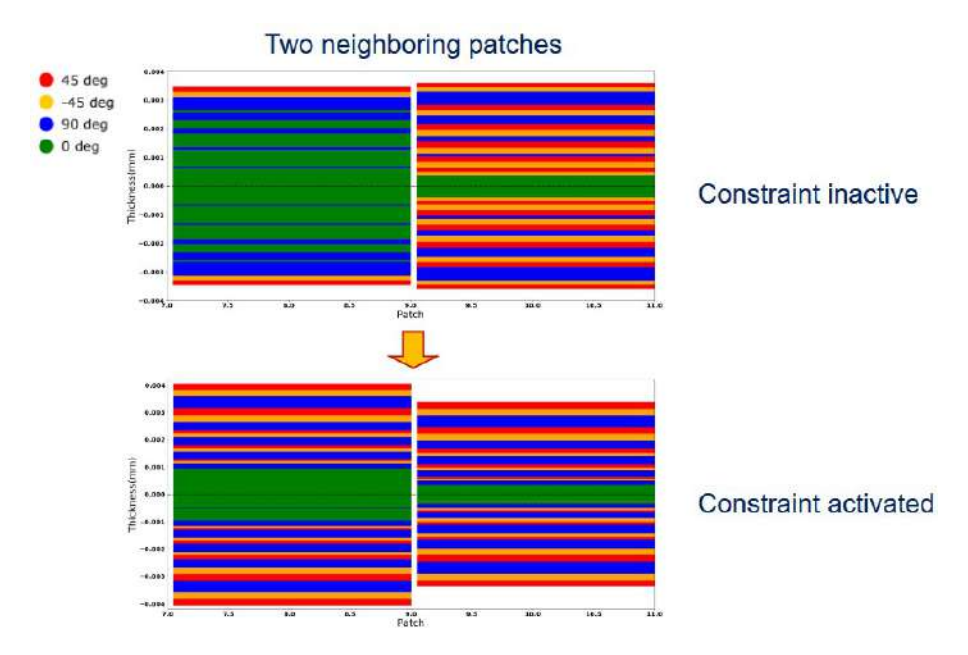


Figure 3.10: Continuity constraint applied to two neighbouring patches [128].

Chapter 4

Aircraft Performance Analysis Framework

This chapter presents a comprehensive description of the high-fidelity aerostructural analysis used to evaluate aircraft performance. An overview of the adopted framework, the corresponding software, and the methods used to solve the aerostructural problem is first introduced. Subsequently, the trimming process is succinctly explained. Finally, the aerodynamic and structural disciplines are described, along with the methods utilised for load and displacement interpolation and aerodynamic mesh deformation.

4.1 Flight Performance

The primary objective of the present study is to investigate the effects of increasing the aspect ratio on transport aircraft performance. To that end, following the completion of the structural sizing optimisations, the performance of the aircraft is analysed.

The relationship between aspect ratio and aircraft performance is not solely an aerodynamic matter but rather a multidisciplinary problem. Therefore, in addition to examining twist, lift distribution and drag, the aircraft's Breguet range is also considered. The Breguet range serves as a comprehensive measure of overall aircraft performance, as it encapsulates both aerodynamic and structural efficiency in a physically meaningful manner. The Breguet range of the aircraft can be estimated for a simplified cruise segment as [32],

$$R_{Br} = \frac{cMa}{\mathsf{TSFC}} \frac{L}{D} \ln \left(\frac{W_{\mathsf{initial}}}{W_{\mathsf{final}}} \right) \,, \tag{4.1}$$

where the Mach number Ma and the speed of sound c are functions of flight altitude and velocity; TSFC denotes the Thrust-Specific Fuel Consumption, determined by the propulsion system; the lift-to-drag ratio L/D reflects the aircraft's aerodynamic efficiency; and $W_{\rm initial}$ and $W_{\rm final}$ correspond to the total aircraft mass at the beginning and end of the cruise segment. The difference between these two masses represents the fuel weight burned during the mission, $W_{\rm fuel}$.

To examine aircraft performance, a high-fidelity multidisciplinary design analysis and optimisation framework is used. This framework was developed by Volle et al. [25, 26] at the DLR in collaboration with Airbus Defence and Space, and couples Airbus's MDO suite Lagrange [23, 24] with DLR's CFD solver TAU [27–29] through the high-performance computing (HPC) multidisciplinary software integration platform FlowSimulator [129, 130].

The framework allows for various types of objective functions, considering simultaneously shape and sizing parameters whilst adhering to industrial-scale structural sizing criteria. It combines multifidelity aerostructural analysis methods, where high-fidelity aerostructural analysis is used to evaluate performance-critical design points, while structurally critical loads are assessed using lower-fidelity aerostructural methods. For a detailed description of the framework's methodology, including the derivation of coupled aerostructural sensitivities with respect to shape and sizing parameters, refer to [25, 26, 131]. Volle [132] applied this framework to a transonic wing MDO benchmark case [133], optimising the wing using structural sizing and shape design variables to minimise fuel burn. The results showed good agreement with reference data, validating the framework's accuracy and reliability.

A succinct description of the framework's high-fidelity aerostructural analysis module used for performance evaluation follows.

4.2 Aerostructural Analysis

The high-fidelity aerostructural analysis module uses a three-field formulation of the aerostructural problem, where mesh deformation is incorporated as an additional discipline alongside aerodynamic and structural analysis. In this formulation, $\mathcal{R} \equiv \{\mathcal{R}_F, \mathcal{R}_M, \mathcal{R}_S\}$ corresponds to the residuals of the discretised governing equations for fluid flow, mesh deformation, and structural analysis, respectively. The state variables are $\mathbf{y} \equiv \{\mathbf{y}_F, \mathbf{y}_M, \mathbf{y}_S\}$, where \mathbf{y}_F denotes the fluid state within the CFD mesh, \mathbf{y}_M represents the deformed aerodynamic volume mesh coordinates, and \mathbf{y}_S refers to the structural displacement. In addition to this formulation, coupling between the aerodynamic and structural disciplines is needed to capture the effects of aeroelasticity on performance. This coupling is addressed through an iterative process, which sequentially solves the fluid flow, load interpolation, structural deformation, displacement transfer, and aerodynamic mesh deformation sub-problems.

The aerostructural analysis begins with a CFD simulation, with TAU solving the governing flow equations. The aerodynamic forces are then interpolated from the aerodynamic domain onto the structural mesh. Based on these aerodynamic loads, Lagrange's finite element solver computes the elastic displacement. These structural deformations are interpolated onto the aerodynamic surface mesh, and applied as boundary conditions in the aerodynamic mesh deformation problem.

The convergence criterion of the coupling process is defined by the L^2 norm of the variation in elastic deformation at the fluid-solid interface. The rate of convergence for the aerostructural coupling is improved through a dynamic under-relaxation using the standard Aitken Δ^2 method, as described by Küttler et al. [134]. To simulate free-flight conditions, the aerostructural coupling is wrapped within a gradient-based trimming process.

The CFD solver TAU and the MDO suite Lagrange, along with the mesh deformation and coupling methods used in this work, are integrated within the FlowSimulator environment. The high-fidelity aerostructural analysis process used for performance evaluation is illustrated in Figure 4.1, with the corresponding XDSM diagram shown in Figure 4.2.

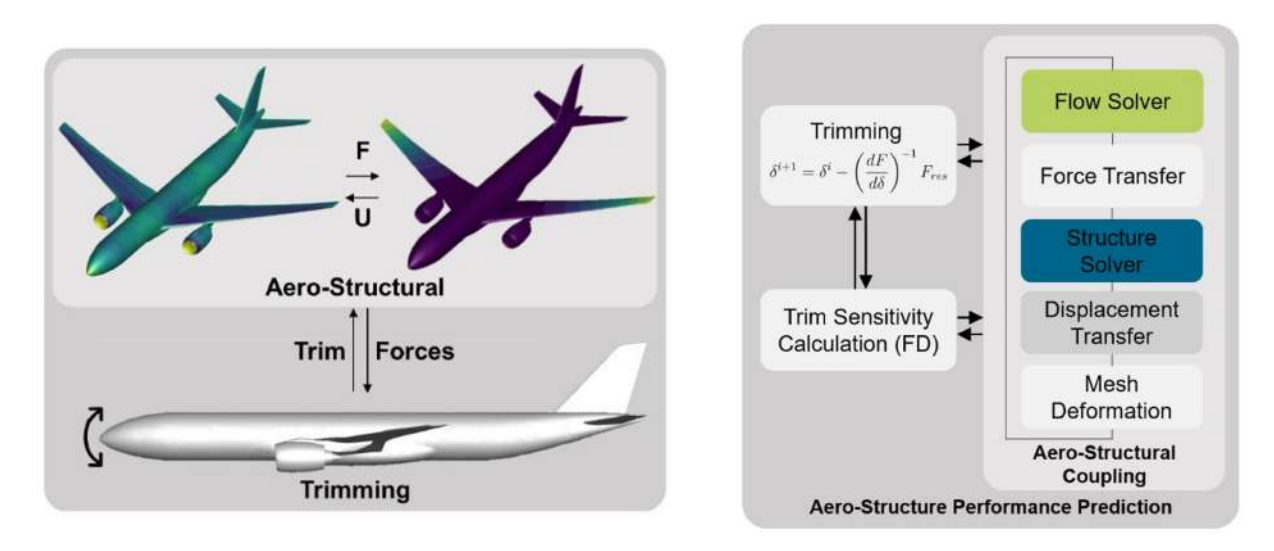


Figure 4.1: Aircraft performance evaluation process [25].

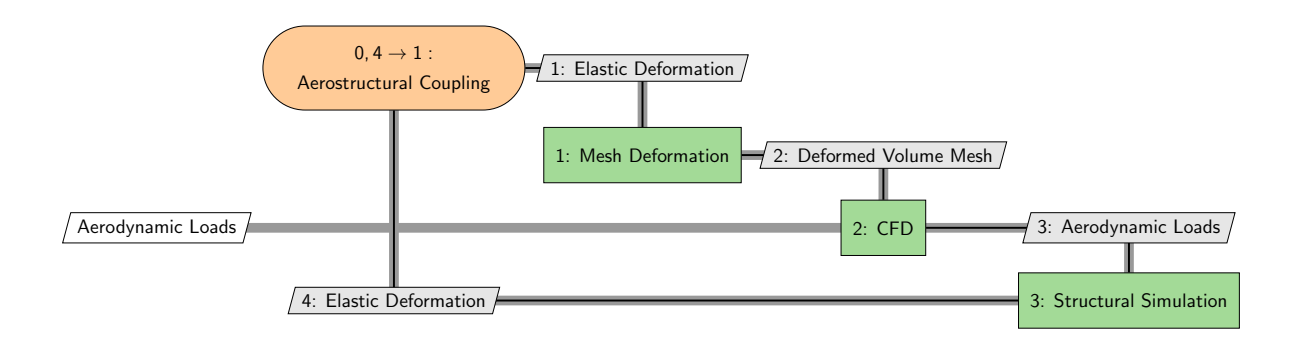


Figure 4.2: Coupled aerostructural analysis for performance evaluation.

4.3 Trimming

A feasible trimming state is essential for accurate aircraft performance evaluation. In the used framework, the aerostructural coupling is embedded within a gradient-based optimisation trimming process to achieve free-flight conditions by balancing the aircraft's weight and aerodynamic forces, as illustrated in Figure 4.3.

The aircraft is trimmed for a target lift force by solving a gradient descent optimisation problem, using one-sided finite-differences to compute the gradients of the trimming forces with respect to the trim variables under the assumption of linearity. The trimming variable used is the angle of attack α .

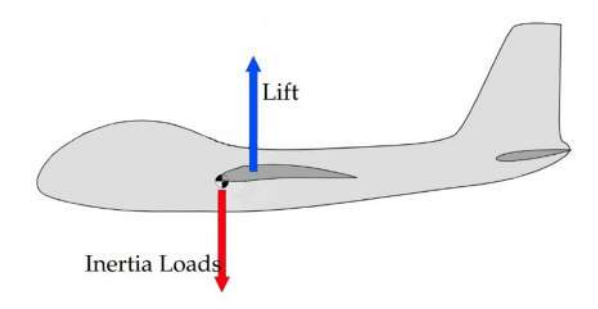


Figure 4.3: Force equilibrium in trimming for performance evaluation (adapted from [46]).

4.4 Aerodynamic Discipline

High-fidelity aerostructural analysis is necessary to evaluate the aircraft's performance. High-fidelity aerodynamics is required as reliable predictions of aerodynamic drag are unattainable using lower-fidelity models and are crucial for determining the proposed performance metrics. However, high-fidelity aerodynamic models are inherently more complex and computationally expensive.

The fluid flow problem is governed by the compressible Reynolds-averaged Navier-Stokes (RANS) equations, coupled with the Spalart-Allmaras (SA) one equation turbulence model in negative formulation. In differential form, the governing flow equations are given by

$$\mathcal{R}_F = \frac{\partial \mathbf{y}_F}{\partial t} + \nabla \cdot (\phi_c - \phi_v) = 0, \qquad (4.2)$$

where ϕ_c and ϕ_v are the convective and diffusive fluxes, respectively, and the state variables y_F denote the conserved quantities of the flow, including density, momentum, and total energy. The equations are discretised using the finite volume method and are solved using DLR's CFD solver TAU [27–29].

The generation of high-fidelity aerodynamic meshes is significantly more intricate than for linear aerodynamics. These meshes must be meticulously tested to ensure they accurately capture all relevant effects.

4.5 Structural Discipline

The structural problem is governed by the equations of linear elasticity. Applying the finite element method for discretisation, the structural residuum \mathcal{R}_S is expressed as

$$\mathcal{R}_S = K y_S - f_S = 0, \qquad (4.3)$$

where K is the symmetric stiffness matrix, y_S is the state variables vector representing the structural displacement, and f_S is the sum of the forces acting on the structure. The structural problem is solved using the built-in FE solver of Airbus's MDO suite Lagrange. As the structural problem for performance evaluation mirrors that of the structural sizing, the finite element model used can be the same.

4.6 Loads and Displacement Transfer

The aerostructural analysis is solved iteratively by sequentially updating the fluid flow, structural, and aerodynamic mesh deformation solutions. A mesh-free approach based on the Moving Least Squares (MLS) method [135] is used to interpolate the loads and displacements between the structural and aerodynamic domains. This method is independent of the formulation of the structural and fluid problems and is both conservative and consistent.

At each iteration, the forces on the aerodynamic surface mesh $f_{\delta F}$ are interpolated as boundary conditions to the structural problem, yielding the aerodynamic forces on the structural nodes $f_{\delta S}$, by using

$$\boldsymbol{f}_{\delta S} = \boldsymbol{M}^{\mathrm{T}} \boldsymbol{f}_{\delta F} \,, \tag{4.4}$$

where M denotes the mapping operator. Similarly, the structural displacements from the finite element mesh at the fluid-solid interface $u_{\delta S}$ are interpolated onto the fluid flow domain, yielding the deformations on the aerodynamic surface mesh $u_{\delta M}$, using

$$u_{\delta M} = M u_{\delta S}. \tag{4.5}$$

These displacements serve as boundary conditions for the fluid flow mesh deformation sub-problem.

4.7 Aerodynamic Mesh Deformation

To solve the high-fidelity aerostructural analysis problem, the aerodynamic volume mesh must adapt to the deformation of its surface mesh induced by the structural displacement. The mesh deformation method used is based on the linear elasticity analogy proposed by Rempke [136], whereby the fluid flow mesh is considered analogous to a volumetric structure problem. The governing equation for mesh deformation is expressed as

$$\mathcal{R}_M = K_M y_M - f_M(u) = 0, \qquad (4.6)$$

where y_M is the state variables vector denoting the deformation of the aerodynamic volume mesh, K_M is a symmetric stiffness matrix constructed by assigning stiffnesses to each element of the fluid flow mesh, inversely proportional to the element's volume, and f_M is a fictitious force imposing the Dirichlet boundary condition of the structural displacement at the aerodynamic surface mesh.

Chapter 5

DLR-F25 Models

This chapter focuses on the aircraft configurations analysed in this study. It begins by describing the main geometrical characteristics of the DLR-F25 baseline aircraft model. Subsequently, the generation of a higher aspect-ratio variant of this configuration is presented. Finally, the analysis models used for structural sizing and performance evaluation of both variants are discussed.

5.1 Geometric Models

The principal objective of this study is to investigate the impact of increasing the aspect ratio on aircraft performance, considering the trade-off between aerodynamic benefits, wherein higher aspect-ratio wings reduce induced drag, against the structural mass penalty necessary to ensure structural integrity. To this end, two aircraft models were considered: the high aspect-ratio DLR-F25 baseline configuration and its newly developed variant with an even greater aspect ratio.

5.1.1 Baseline Configuration

The DLR-F25 is a single-aisle, narrow-body aircraft model with a high aspect-ratio wing, designed for the short-to-medium range market segment [30, 31, 137]. It has been primarily developed by the DLR based on the Airbus A321neo, having similar capacity and design parameters to reflect the technological state of the art in 2020. The DLR-F25 is designed to accommodate 239 passengers within a fuselage measuring 44.51 metres in length, offering a range of 2,500 nautical miles. It is powered by two ultrahigh bypass-ratio turbofan engines, mounted under the wing just ahead of the kink. The landing gear is housed within the fuselage's belly fairing. This research aircraft model is currently used in the UPWing project [17] as a reference platform for assessing and validating innovative technologies. The outer geometry of the DLR-F25 is illustrated in Figure 5.1.

The DLR-F25 wing planform is shown in Figure 5.2. The wing can be divided by five sections: centre, root, kink, mid, and tip. The original design incorporated a folding wingtip at the mid-section to comply with the 36 metres wingspan limit imposed by the ICAO Aerodrome Reference Code C [58]. However, as mentioned in Section 2.3, this feature falls outside the scope of the present study.

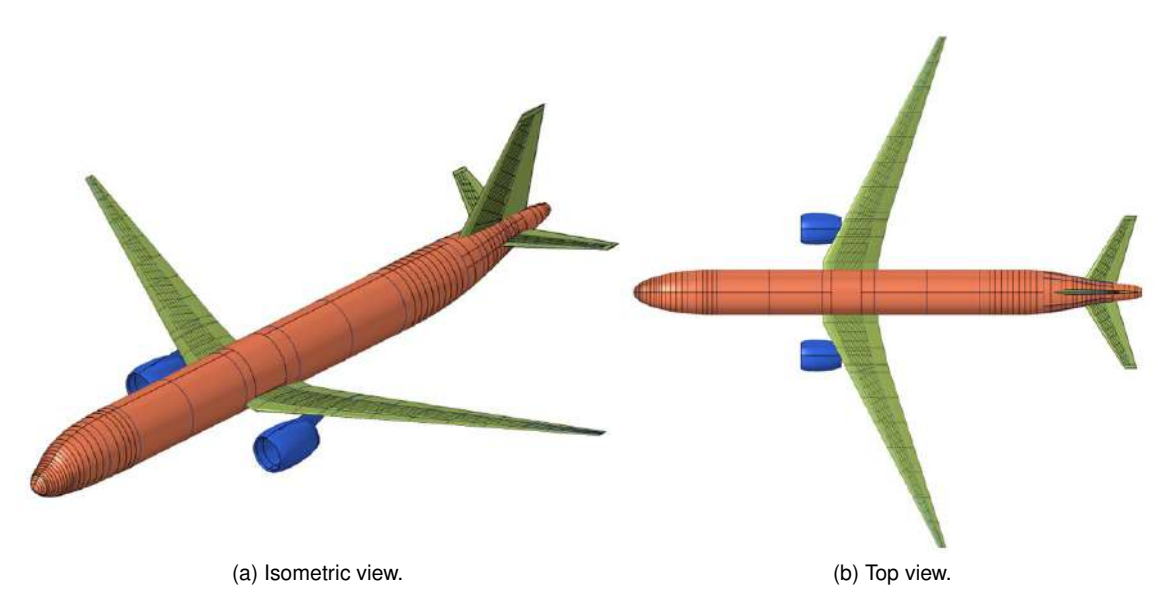


Figure 5.1: Outer geometry of the DLR-F25 baseline configuration generated using Descartes.

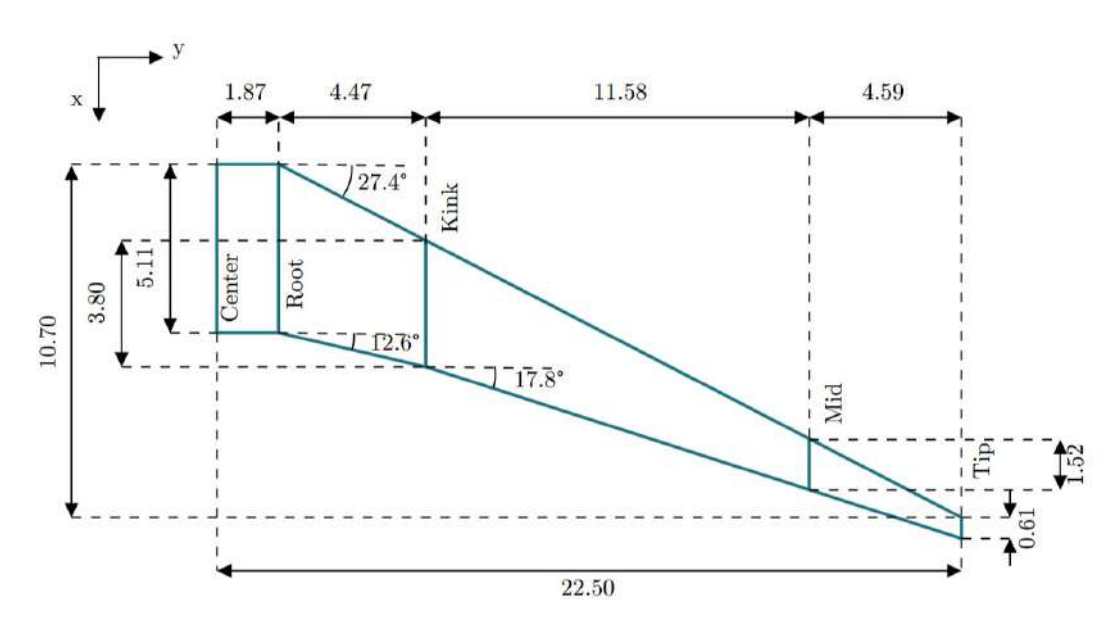


Figure 5.2: DLR-F25 wing planform (dimensions in metres) [137].

The key characteristics of the DLR-F25 wing are summarised in Table 5.1. The DLR-F25's aspect ratio of 15.6 is significantly higher than that of conventional transport aircraft, such as the Airbus A321-100, which has an aspect ratio of 9.4 [138]. Additionally, the DLR-F25 wing has a tip chord of 0.6 metres and a taper ratio of 0.12, resulting in a significantly thinner and narrower wing compared to a typical transport aircraft, such as those of the Airbus A320 family, whose tip chord measure approximately 1.5 metres and have taper ratios of 0.24 [138, 139].

The DLR-F25 features a carry-through wingbox extending through the fuselage. The wing comprises a two-spar design with 31 ribs per half-span and 11 stringers, which progressively taper as the wing narrows towards the tip. The ribs and stringers have a minimum pitch of 800 mm and 220 mm, respectively, to prevent buckling from becoming a dominant design constraint.

Each half wing is equipped with multiple high-lift devices, including six slats, three flaps, and two ailerons, as depicted in Figure 5.3.

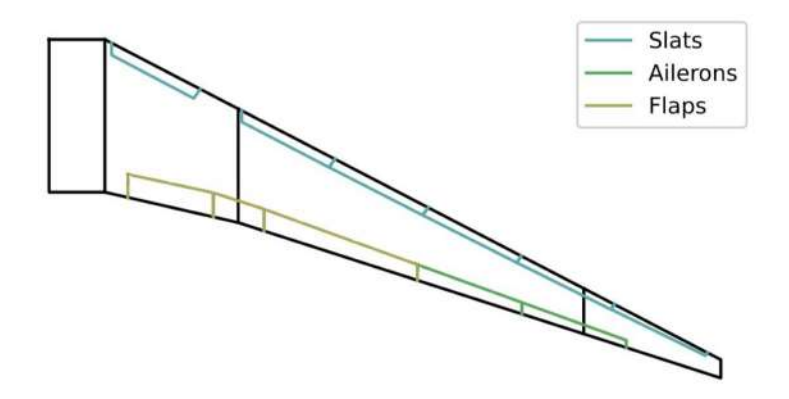


Figure 5.3: DLR-F25 wing control surfaces (adapted from [137]).

5.1.2 Higher Aspect-Ratio Variant

The DLR-F25 baseline aircraft was modelled using a parametric geometry representation in CPACS [30], wherein the positions of structural components were defined relative to the wing's coordinate system, as detailed in Section 3.2. This approach enables the automatic adjustment of component positions in response to shape variations, such as an increase in wingspan. Leveraging that parametric geometry, a higher aspect-ratio variant of the DLR-F25 was generated by modifying the baseline wing shape using Descartes.

To generate the higher aspect-ratio variant, the central part of the wing, up to the kink section, remained unaltered to preserve the wing-fuselage junction and the original pylon attachment configuration. Consequently, only the outer wing sections, aft of the engine position, were modified.

Several methods exist in the literature for increasing an aircraft's aspect ratio, involving changing or preserving parameters such as taper ratio, trailing and leading-edge sweep, or wing surface area, depending on the design objectives [48, 137]. Some of these methods are illustrated in Figure 5.4.

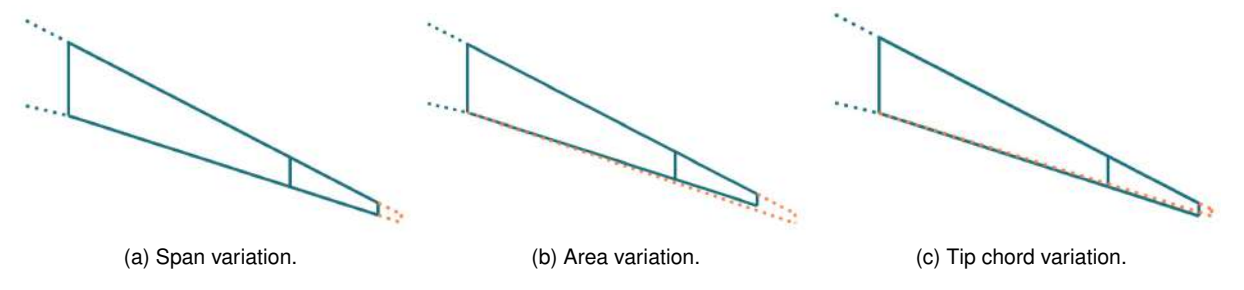


Figure 5.4: Schematic representation of different aspect-ratio variation methods [137].

For this study, the area method depicted in Figure 5.4b was adopted. This method maintains the leading-edge sweep and taper ratio constant but increases the surface area and trailing-edge sweep. This approach was selected to prevent unintended aerodynamic effects that could arise from varying the taper ratio, which might obscure or counteract the impact of increasing the aspect ratio. Maintaining

the baseline taper ratio was particularly critical, given that the DLR-F25's taper ratio was already small, and further reduction would pose significant aerodynamic challenges at the wingtip. Furthermore, this method has been shown to provide longitudinally stable aircraft [48] and, among the methods shown in Figure 5.4, it is the most effective in reducing induced drag.

Using that approach, the new higher aspect-ratio DLR-F25 variant was generated in Descartes through a shape change to the baseline wing geometry, as illustrated in Figure 5.5a. The outer wing segments were stretched to increase the overall wingspan by 10%. This resulted in a new aircraft model with a 11.5% higher aspect ratio of 17.4 and a 7.5% larger wing surface area. The control surfaces were proportionally extended along with the rest of the wing, maintaining their relative positions, and the vertical and horizontal tailplane remained unchanged. The maximum take-off weight was considered a top-level aircraft requirement and, therefore, kept constant.

Henceforth, the baseline DLR-F25 and its higher aspect-ratio variant will be referred to as F25-AR15 and F25-AR17, respectively. Table 5.1 summarises the main geometrical differences between the model's wings.

Table 5.1: DLR-F25 wing ke		

Parameter		Baseline	Higher AR
		F25-AR15	F25-AR17
Aspect ratio	AR	15.6	17.4
Wingspan	b	44.60 m	49.04 m
Wing area	S	$129.59 \; \mathrm{m}^2$	139.21 ${\sf m}^2$
Sweep at 1/4 chord	$\Lambda_{c/4}$	24.43°	24.69°
Taper ratio	$\stackrel{\gamma}{\lambda}$	0.12	0.12

The substantial increase in span for the F25-AR17 altered the baseline rib pitch. This resulted in significantly larger buckling fields for the F25-AR17, making buckling a critical design constraint and precluding a fair direct comparison between the two aspect ratio variants. Consequently, a topological modification was performed on the F25-AR17 wing structure, whereby two additional ribs were incorporated into the middle section of the wing and one near its tip. These topological changes can be seen in Figure 5.5b. As a result, the analysis models for structural sizing of the F25-AR17 were remeshed rather than directly morphed from those of the F25-AR15, as described in Section 3.2.

The analysis models for the structural sizing and performance evaluation of both variants will be presented in the following sections.

5.2 Structural Models

The structural problem to be solved for the structural sizing optimisation and the performance analysis is identical; thus, the same structural model is used for both tasks. Since mesh morphing is not feasible, a distinct structural model for each aircraft variant must be generated.

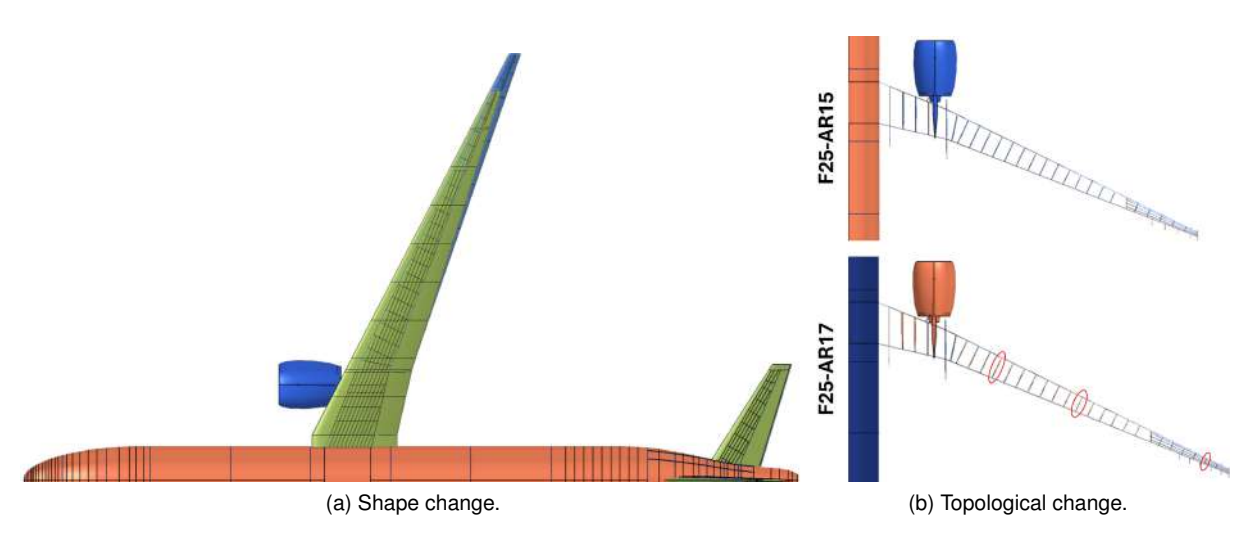


Figure 5.5: Shape and topological modifications applied to the F25-AR17 wing.

The FE structural models were generated using Descartes' internal meshing functionality. The skins, spars, and ribs were modelled using shell elements, specifically CQUAD4 and CTRIA3, while the stringers and spar caps were modelled using one-dimensional elements, namely the CBAR and CROD, respectively. The mesh quality was assessed using HyperMesh[®], and elements that failed to meet the established criteria concerning aspect ratio, skew angle, and warpage were corrected.

The FE structural model for the F25-AR15 is shown in Figure 5.6. The F25-AR17 model follows a comparable discretisation approach, as both models were constructed using the same methodology.

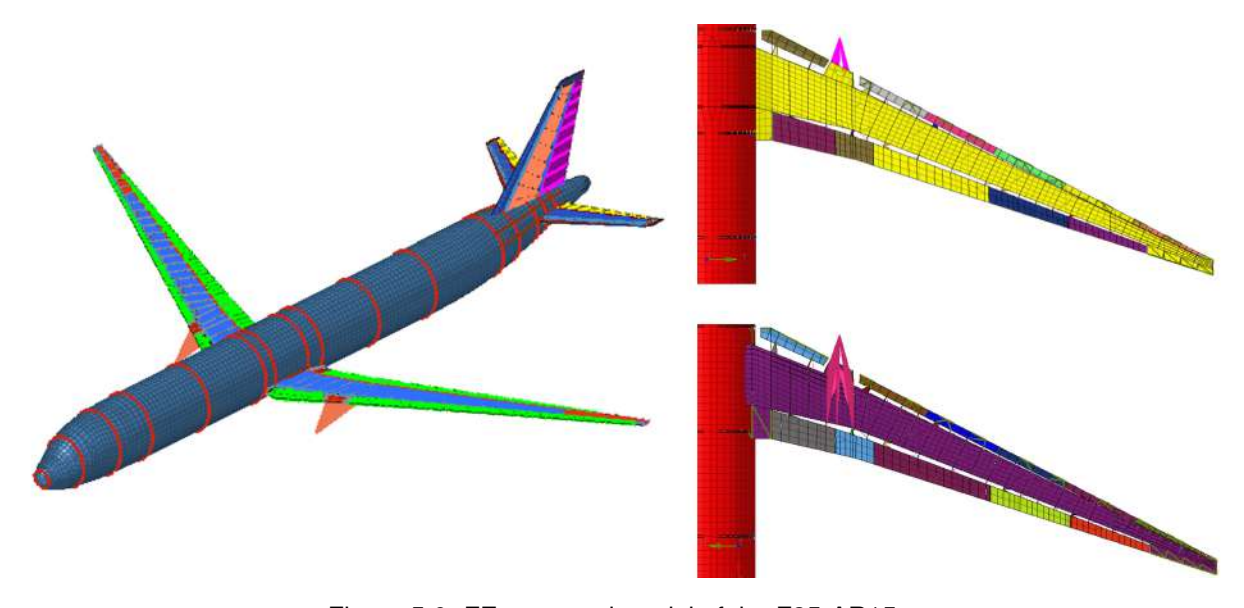


Figure 5.6: FE structural model of the F25-AR15.

A mesh convergence study was not conducted in the present work, as Descartes's internal meshing functionality is known to generate sufficiently fine meshes for preliminary design purposes. Furthermore, previous studies on the DLR-F25 have used meshes of similar refinement to the present ones, yielding satisfactory results [48]. Table 5.2 presents a comparative summary of the refinement and discretization used in the structural modelling of each aircraft variant.

Table 5.2: Structural discretization and elements of the F25-AR15 and F25-AR17 wings.

Parameter	F25-AR15	F25-AR17
Nodes	13,152	13,331
CQUAD4 elements	13,567	13,815
CTRIA3 elements	1,191	1,201
CROD elements	5,812	5,906
CBAR elements	3,175	3,331

The DLR-F25 model initially featured four possible mass configurations, comprising two distinct mass values and two different centre of gravity locations. A modal analysis was conducted, revealing that the differences in the centre of gravity had a negligible impact on the modal behaviour (i.e., less than 1% change in frequency for each mode). Consequently, to optimise computational resources, the mass configurations were reduced to two, retaining only one centre of gravity location. The two selected mass configurations correspond to the Maximum Take-Off Weight (MTOW) of 81,656 kg and the Maximum Zero Fuel Weight (MZFW) of 69,322 kg.

Irrespective of the mass configuration, the aircraft's weight is divided into two components: the structural weight of the composite wing, and the combined weight of the fuel, payload, passengers and the remaining aircraft structure, including engines and pylons.

The weight of the composite wing is evaluated from the size and material properties of its finite elements. The wing skin is modelled using a symmetric and balanced 24-ply carbon fibre reinforced polymer (CFRP) laminate with four ply orientations (0°, 90°, and $\pm 45^{\circ}$), and a material density of 1,580 kg/m³. The spar webs are modelled by a similar 20-ply CFRP laminate. The T-shaped stringers and spar caps are modelled using homogenised CFRP properties, assuming a ply distribution of 70% at 0°, 20% at $\pm 45^{\circ}$, and 10% at 90°, with a density of 1,750 kg/m³. The ply distribution for the stringers and spar caps remains constant throughout the optimisations.

The remaining weight is modelled by 131 distributed concentrated mass points, implemented as CONM2 elements and connected to the FE model using RBEs. Figure 5.7 illustrates the distribution of mass points in the F25-AR15, with the F25-AR17 having a similar arrangement.

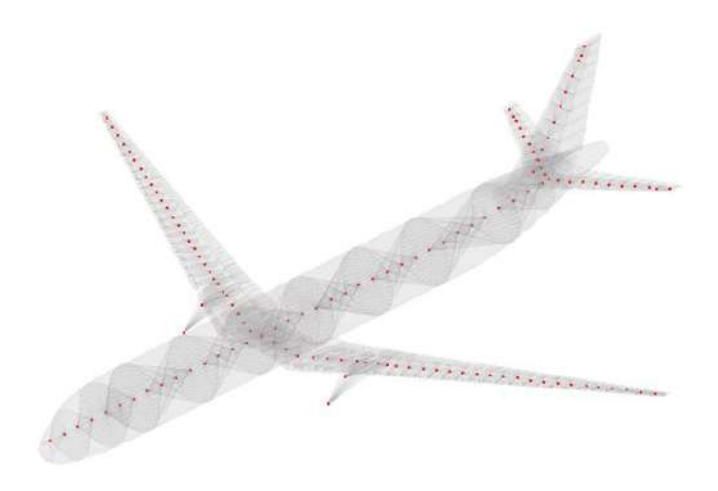


Figure 5.7: F25-AR15 CONM2 mass point distribution.

5.3 Aerodynamic Models

Two levels of fidelity are used for the aerodynamic discipline: high-fidelity aerodynamics is used for the performance analysis module, whereas linear aerodynamics is used in the loads model to drive the structural sizing optimisation.

5.3.1 Structural Sizing Optimisation

As outlined in Section 3.4.1, the doublet lattice method was selected to compute the aerodynamic loads for structural sizing. The aerodynamic meshes for this method were generated from the parametric geometry using Descartes. The entire aircraft, including the wing, fuselage, and vertical and horizontal tailplanes, was discretised. Figure 5.8 presents the DLM model for the F25-AR15.

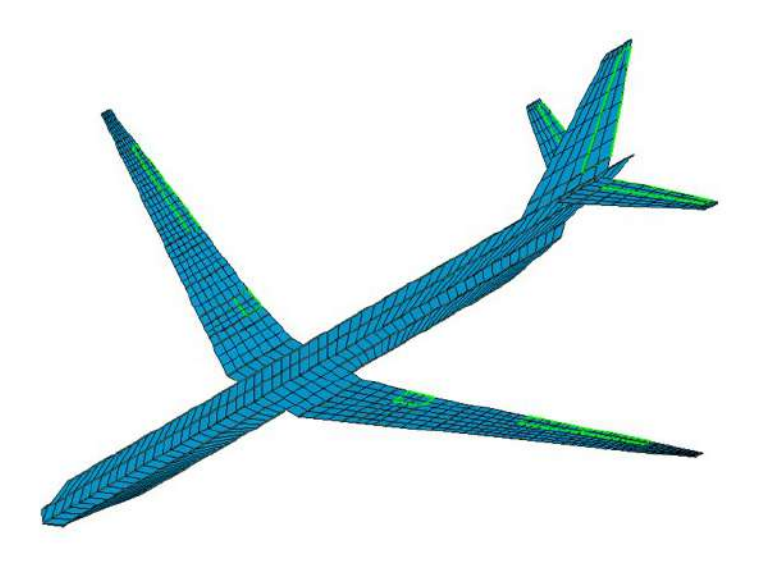


Figure 5.8: F25-AR15 doublet lattice method mesh.

The wing was discretised with 7 panels in the chordwise direction and 43 panels in the spanwise direction. The discretisation for the F25-AR17 follows the same approach. A limitation of the used meshes is that the number of chordwise panels was constant from root to tip, resulting in a coarser discretisation at the root and a denser distribution towards the tip. Additionally, Descartes constrains the panel length in the chordwise direction to be uniform, preventing increased discretisation around the leading edge compared to the trailing edge.

A mesh refinement study was not conducted in this work, as Descartes' meshing function for potential methods produces sufficiently fine meshes for preliminary design purposes. Furthermore, in previous studies [137], the DLR-F25 wing was discretised using a DLM mesh with a comparable level of refinement, yielding good results.

Control surfaces were also defined within the aerodynamic model according to their CPACS configuration. In Figure 5.8, the control surfaces available for deflection, including the elevator, rudder, and aileron, are outlined in green.

5.3.2 Aircraft Performance

In the aerostructural analysis for performance, the Reynolds-averaged Navier-Stokes equations are solved, as described in Section 4.4. The high-fidelity aerodynamic mesh used is based on a wing-body configuration of the DLR-F25. The vertical and horizontal tailplanes are not represented in this model. To reduce the computational cost associated with CFD analyses, a half-model of the aircraft is used, leveraging the symmetry of the configuration, as illustrated in Figure 5.9 for the F25-AR15.

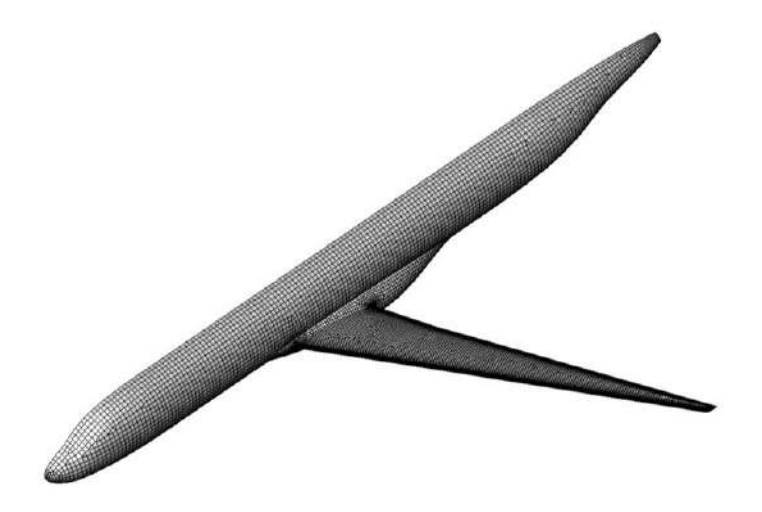


Figure 5.9: F25-AR15 high-fidelity aerodynamic surface mesh.

This computational grid, comprising 1.02 million nodes, was developed by DLR and provided through the UPWing project. The mesh is quite coarse; however it is suitable for the intended purpose. It has been previously utilised in related studies [25], having yielded accurate results for the performance metrics of interest in this work. The aerodynamic model of the F25-AR17 was generated by morphing the existing F25-AR15 mesh, and therefore, both meshes are topologically identical with the same number of nodes and elements.

5.4 Coupling Models

The models presented in Sections 5.2 and 5.3 have a different discretisation, meaning the meshes at the fluid-solid interface do not match, preventing direct information exchange. To enable aerostructural analysis, whether for structural sizing or performance evaluation, a coupling scheme between aerodynamics and structural mechanics is required to interpolate loads and displacements.

For structural sizing, the stiffness model presented in Figure 5.6 is coupled with the aerodynamic model shown in Figure 5.8 using the infinite plate spline method, as described in Section 3.4.3. In this method, the aerodynamic loads and structural displacements are interpolated through a set of structural nodes strategically arranged in a diamond pattern at the intersection of the wing's upper skin with the spars and ribs. Beyond the wingbox, this approach is extended to the leading and trailing edge devices, the fuselage, and the horizontal and vertical tailplanes. Figure 5.10 illustrates this nodal distribution for the F25-AR15 wing. The coupling model for the F25-AR17 follows the same principles.

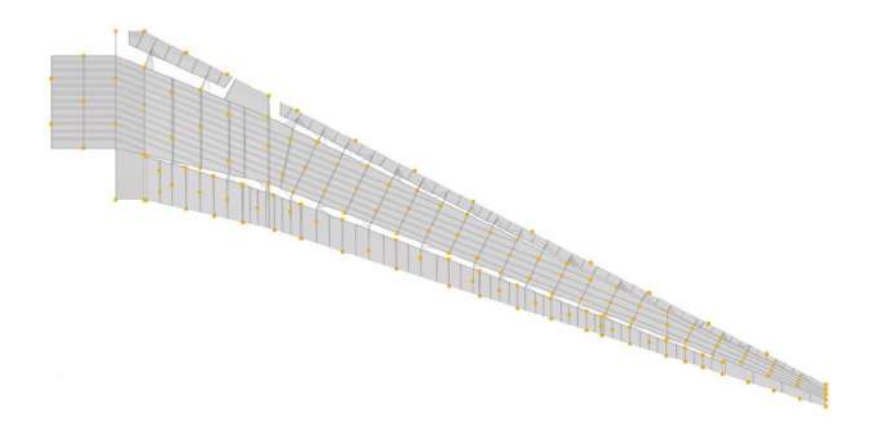


Figure 5.10: F25-AR15 wing coupling for structural sizing.

For the performance analysis, the moving least squares method was used, as detailed in Section 4.6. This mesh-free approach does not rely on a predefined set of nodes, being independent of the specific formulations of the structural and fluid problems. The method is both conservative and consistent.

Chapter 6

DLR-F25 Structural Sizing Optimisation for Minimum Mass

In this chapter, the structural sizing optimisation for mass minimisation is presented. It begins with a formal definition of the optimisation problem, followed by an outline of the optimisation workflow. Subsequently, the static and aeroelastic structural sizing optimisations are presented and analysed. Finally, the performance of both aspect-ratio aircraft is compared.

6.1 Problem Definition

For the structural sizing optimisation, it is necessary to define the optimisation parameters, the load cases, the design variables and their bounds and the structural sizing criteria. In this work, the optimisation model was primarily generated from a central parametric geometry using Descartes.

6.1.1 Optimisation Parameters

The objective of the structural sizing optimisation is to minimise the structural weight of the wing-box. As outlined in Section 2.5, the NLPQL algorithm, a second-order gradient-based deterministic optimisation algorithm, was selected for this study. Analytical coupled direct methods are used for the sensitivity analysis, with Lagrange automatically selecting them as the most appropriate approach, given that the number of objective and constraint functions exceeds the number of design variables, as shown in Table 6.4. An active-set strategy is implemented, restricting the sensitivity analysis to the 20,000 most violated constraints. The optimisation problem converges based on a Karush-Kuhn-Tucker (KKT) criterion [140] with a tolerance of 10^{-5} . These optimisation parameters are summarised in Table 6.1.

6.1.2 Load Cases

Pull-up and push-over manoeuvres were defined to be structurally design-driving. The MTOW configuration was used to generate the most critical aerostructural loads. A summary of the load cases

Table 6.1: Optimisation parameters used for structural sizing.

Optimisation Parameters						
Objective Optimisation algorithm Sensitivity analysis Active-set strategy Convergence criteria	Minimise wingbox mass NLPQL Analytical coupled direct 20,000 KKT of 10^{-5}					

considered in the structural sizing optimisation is presented in Table 6.2 [30].

Table 6.2: Load cases considered in the structural sizing optimisation.

Load Case	Load Factor [g]	Mach	Altitude [m]
Pull-up Push-over	2.5 -1	0.81	11,000

6.1.3 Design Variables

The optimisation focused exclusively on the structural sizing of the composite wingbox, specifically the skin, spars, and stringers, as these components bear the majority of the structural loads. The ribs were not structurally sized, as the linear FE model used does not accurately capture the loads acting on them due to their inherently non-linear behaviour.

The design variables were defined within patches using Descartes. For the skin, each patch is bounded by two ribs and two stringers, whereas patches for the stringers and spars are segmented by ribs. These patches are symmetrically linked to ensure both sides of the wing were identical. Figure 6.1 illustrates the design variable patches on the F25-AR15 wingbox, with each colour representing a distinct patch.

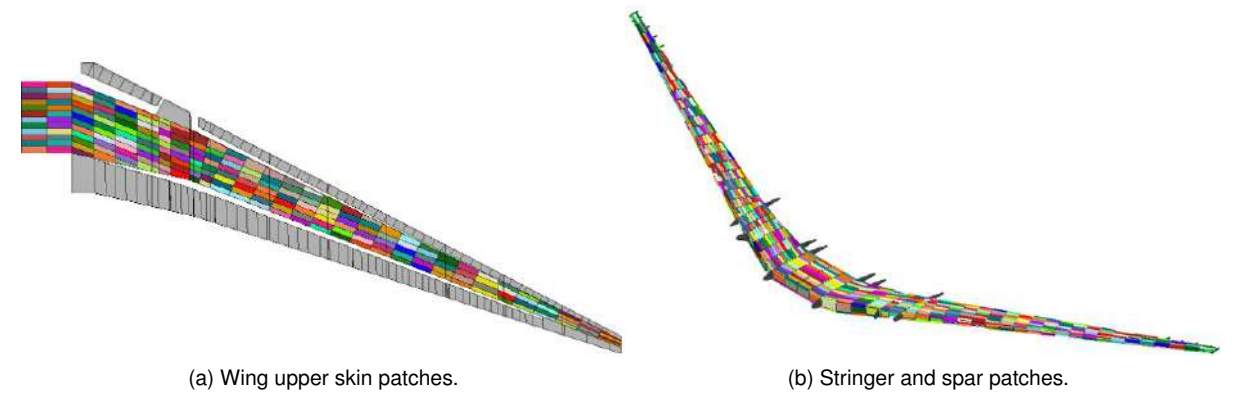


Figure 6.1: F25-AR15 wingbox design variable patches.

The initial composite was symmetric and balanced, and these properties were preserved throughout the optimisation by linking the design variables accordingly. Within each skin and spar web patch, plies of the same orientation are linked to preserve laminate symmetry. To ensure a balanced laminate, the thicknesses of the $+45^{\circ}$ and -45° plies are also linked. Consequently, three design variables per skin and spar web patch control the thickness of the ply orientations, as shown in Figure 6.2.

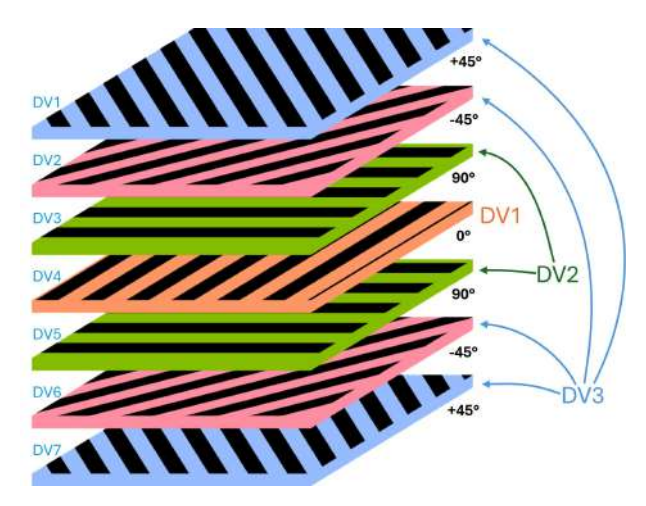


Figure 6.2: Design variable linking resulting in a total of three design variables.

Each spar cap patch is governed by a single design variable that determines its cross-sectional area. The T-shaped stringers are characterised by three design variables, which define the web height, foot width and thickness. As the stringers are constructed from two back-to-back L-profiles, the thickness of the foot and web are linked in a 1:2 ratio, as represented in Figure 6.3.

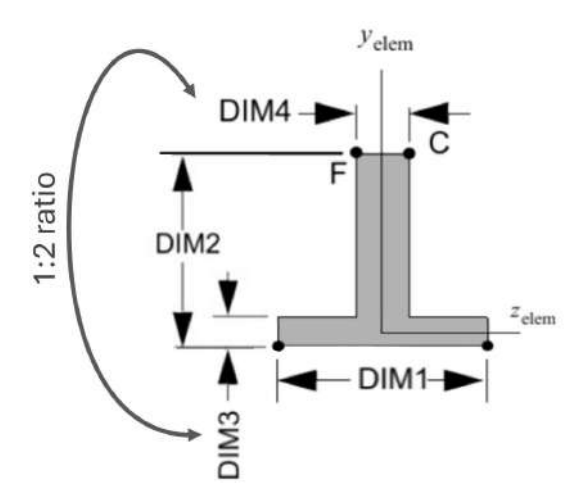


Figure 6.3: T-shaped stringer profile illustrating the 1:2 ratio between the foot and web thickness.

The bounds and initial values for the design variables are summarised in Table 6.3. These values were established in line with requirements concerning maximum and minimum element dimensions, taking into account the geometry of the DLR-F25 to minimise the risk of overlapping structural components, as well as manufacturability constraints related to production capabilities.

6.1.4 Structural Sizing Criteria

The structural sizing criteria for the composite wing focus primarily on optimising the wing covers, as they are the main driver for aeroelastic tailoring. Constraints on strength, buckling, and manufacturability are incorporated into the structural sizing optimisations in accordance with Section 3.5.

Table 6.3: Design variables and their bounds for structural sizing.

Component	Section	Design Variable	Lower Bound	Initial Value	Upper Bound
	Upper skin		0.164	0.254	2.000
Skin	Lower skin root	Ply thickness [mm]	0.254	0.508	2.000
SKIII	Lower skin middle	Fly tillckiless [illill]	0.254	1.016	2.500
	Lower skin tip		0.254	0.381	2.000
Spar	Inner & outer	Web ply thickness [mm]	0.164	0.254	2.000
Spar	illiler & outer	Cap area [mm ²]	80	100	1000
		Web height [mm]	51.5	66.5	81.5
	Inner	Foot length [mm]	80	100	120
Stringer		Foot thickness [mm]	3	3	9
Stringer		Web height [mm]	51.5	66.5	68.5
	Outer	Foot length [mm]	80	100	120
		Foot thickness [mm]	3	3	6

Strength Requirements

Strength constraints are uniformly applied to the skin, spars, and stringers, with maximum allowable material strains of 5,000 $\mu\epsilon$ in tension and 3,500 $\mu\epsilon$ in compression, and a safety factor of 1.5 incorporated. Additionally, a minimum wing stiffness requirement was imposed, constraining the maximum wingtip twist to -6.76° for F25-AR15 and -7.01° for F25-AR17, based on an extrapolation of the Airbus A320neo's in-flight twist distribution [141] with a factor of 1.5 applied.

Buckling Requirements

The skin and spar buckling panels are modelled as biaxially loaded, simply supported flat plates with anisotropic material properties. The critical buckling loads are determined using the analytical methods proposed by P. M. Weaver [123–125]. Stringer buckling is evaluated by modelling the stringer and attached sheet as a super-stiffener, with the critical buckling strength determined with the Johnson-Euler formula [126].

The buckling fields are defined by the arrangement of the ribs with stringers or spars, highlighting the importance of the minimum stringer and rib pitches of 220 mm and 800 mm, respectively. In Figure 6.4, the buckling fields for the wing upper skin, spars and the stringers are illustrated. A correction factor was applied to the skin buckling field size to account for the idealised modelling of the stringers as one-dimensional elements. This idealisation causes the buckling fields of the skin to appear larger in the FE model than in reality. To mitigate this discrepancy, a correction factor of 0.95 was applied, reducing the skin buckling field size by 5% to more accurately represent the true structure [104].

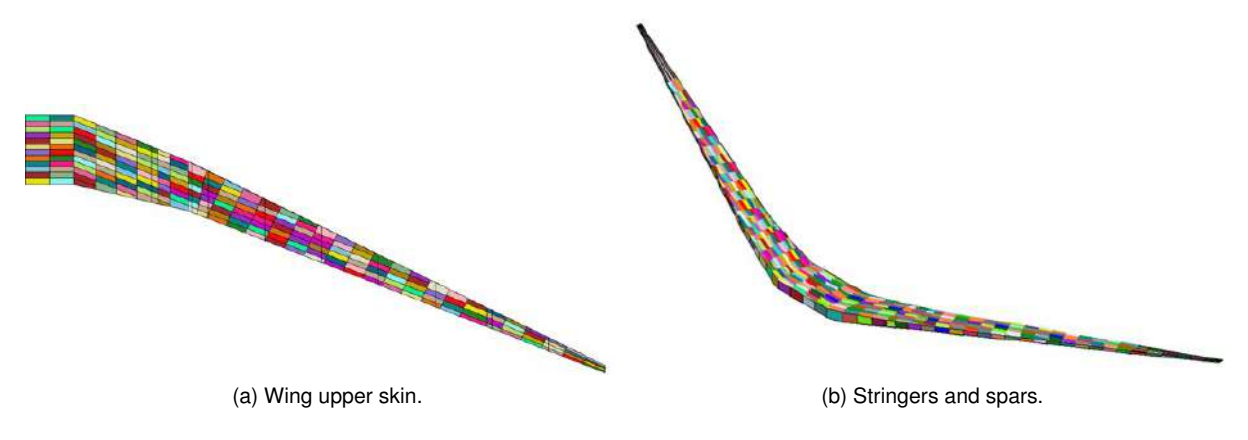


Figure 6.4: F25-AR15 wing upper skin, spars and stringers buckling fields.

Manufacturing Requirements

To ensure manufacturability of the optimised composite wing, thickness and ply share constraints are imposed. Thickness variations between adjacent wing skin patches are limited by a ramp rate of 1:20 in the spanwise direction and 1:10 in the chordwise direction. Continuity constraints prevent abrupt ply share variations, as well as ply drops and ply additions, by restricting ply thickness differences between adjacent patches to 1/10 of the ply thickness. Furthermore, ply share percentages in the skin are constrained to a range of 10 to 63% for 0° and 90° plies, and 20 to 80% for $\pm 45^{\circ}$ plies.

Additionally, a minimum thickness of 4 mm is enforced on the upper skin. On the lower skin, a minimum thickness of 20 mm is imposed in the pylon attachment area, with a 6 mm and 8 mm minimum thickness constraint outboard and inboard of this region. The patch sections where these minimum thicknesses are imposed are shown in Figure 6.5.

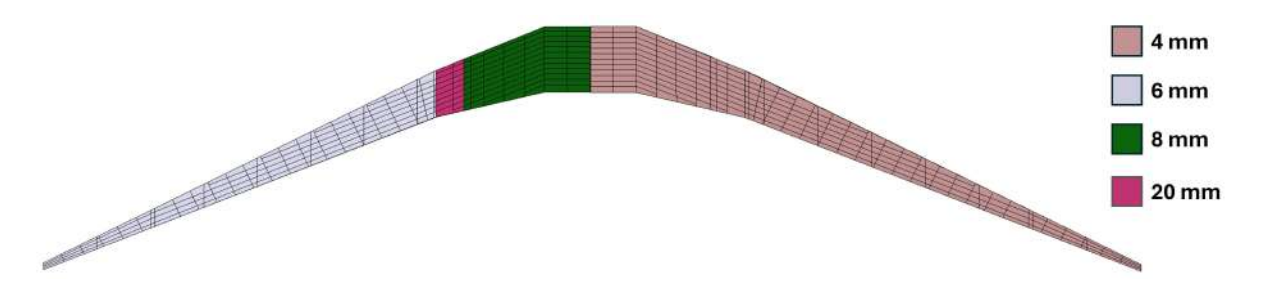


Figure 6.5: Minimum thickness requirements for the wing's lower (left) and upper skin (right).

These considerations led to an optimisation problem with about 3,000 design variables and over 200,000 constraints, as detailed in Table 6.4.

Table 6.4: Structural sizing optimisation problem size.

	Design Variables				Constraints			
	Skin	Spar	Stringer	Total	Strength	Buckling	Manufacturing	Total
F25-AR15	1,251	390	1,284	2,925	137,488	5,904	74,109	217,501
F25-AR17	1,353	470	1,372	3,195	149,800	6,352	81,025	237,177

6.1.5 Trimming

The load cases for structural sizing are trimmed not only to achieve equilibrium between aerodynamic and inertial forces, but also to balance the pitching moment, as shown in Figure 6.6. Unlike in the aerostructural analysis for performance, the pitching moment can now be used as a trimming condition because the aerodynamic model for structural sizing includes the horizontal tailplane. Trimming is formulated as an optimisation problem in Lagrange, with the angle of attack and elevator deflection as design variables. Since Lagrange only supports inequality constraints, the resulting loads in the relevant degrees of freedom are constrained within an allowable range.

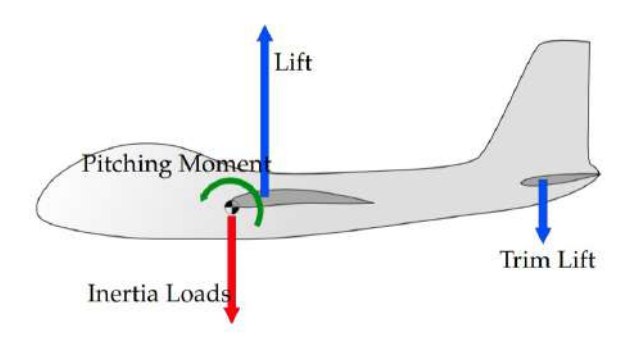


Figure 6.6: Force and pitching moment equilibrium in trimming for structural sizing [46].

6.2 Optimisation Workflow

The structural sizing optimisation process was divided into two main steps: a preliminary static structural sizing, followed by an aeroelastic structural sizing, as outlined in Figure 6.7.

Static Structural Sizing

Trim and Strenght Buckling Manufacturing structural static loads constraints criteria requirements Aeroelastic structural model

Figure 6.7: Structural sizing optimisation workflow.

A preliminary static structural sizing is conducted prior to the aeroelastic optimisation to quickly establish a feasible design with minimal computational cost. The design obtained from the static structural sizing provides a significantly improved starting point for the aeroelastic optimisation compared to a constant-thickness wing or other arbitrary initial designs.

In the static structural sizing, trimming is performed separately *a priori*, and the aerodynamic loads are computed once in advance in an aeroelastic analysis and then fixed to be used throughout the preliminary structural sizing. This means that, at this stage, the aeroelastic effects are neglected to facilitate convergence. Furthermore, within the static structural sizing optimisation, constraints are progressively introduced, starting with strength constraints, followed by buckling criteria, and concluding with manufacturing requirements. Each time a new set of constraints is introduced, the structural sizing optimisation

uses the previously converged solution as the new starting point. The goal of incrementally integrating the constraints is to ensure their proper formulation and incorporation into the optimisation.

Once the full set of constraints has been introduced and the static structural sizing optimisation has converged, the resulting design serves as the starting point for the aeroelastic structural sizing optimisation. In the aeroelastic structural sizing, the complete optimisation problem is solved, incorporating the fully coupled aeroelastic analysis described in Section 3.3, in which aerodynamic loads are recomputed at each iteration. This ultimately leads to the final optimised design.

6.3 DLR-F25 Baseline Properties

To gain a better understanding of the initial properties of the DLR-F25 aircraft models, the aeroelastic analysis described in Chapter 3 is carried out prior to structural sizing. Before the optimisations, both the F25-AR15 and F25-AR17 wings had a generic uniform thickness. As expected, neither aircraft variant satisfied the imposed criteria prior to structural sizing, with significant constraint violations observed, particularly near the wing root. Figure 6.8 illustrates the uniform thickness and strength constraint violation in the upper skin of the F25-AR15 wing.

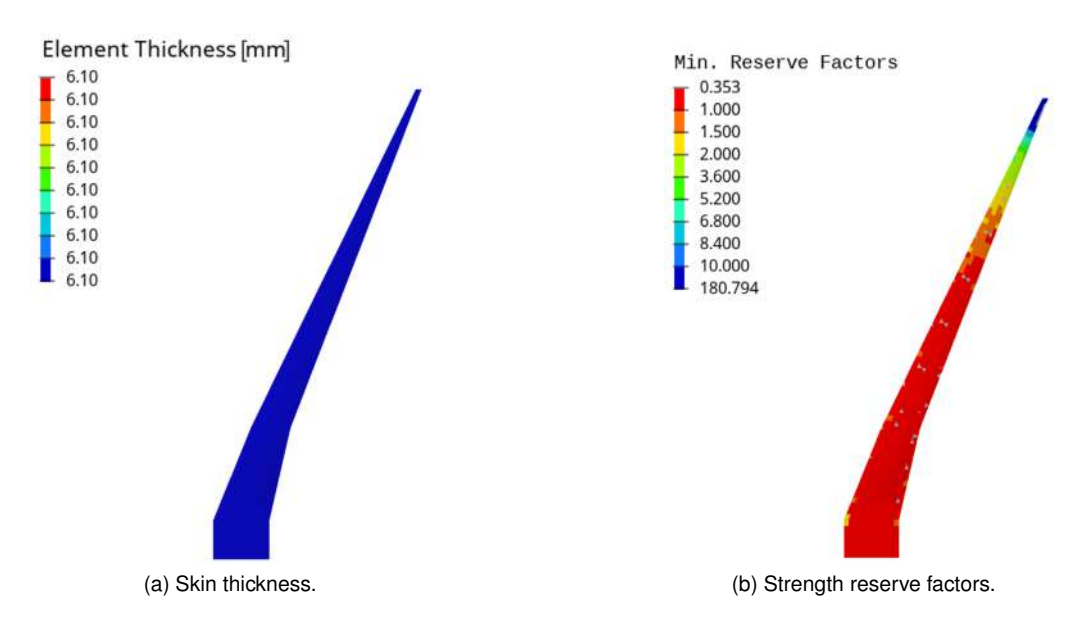


Figure 6.8: F25-AR15 wing upper skin uniform thickness and strength constraint violation prior to structural sizing.

The wingbox structural mass prior to structural sizing is presented in Table 6.5. Due to the extensive constraint violations in the baseline configurations, it is possible that the structural mass of the designs may increase as a result of the structural sizing.

Figure 6.9 presents the bending and twist distributions of both aspect-ratio aircraft under push-over and pull-up manoeuvres at MTOW, prior to structural sizing. Both wings exhibit significant flexibility, with the F25-AR17 experiencing greater deformations than the F25-AR15 as a reflection of its higher aspect ratio. The pull-up manoeuvre causes the wing to bend upwards, with a nose-down twist from root to tip, while the push-over manoeuvre results in downward bending accompanied by a positive twist.

Given that the structural modelling is linear, the deformation resulting from the push-over manoeuvre is symmetric to that of the cruise condition.

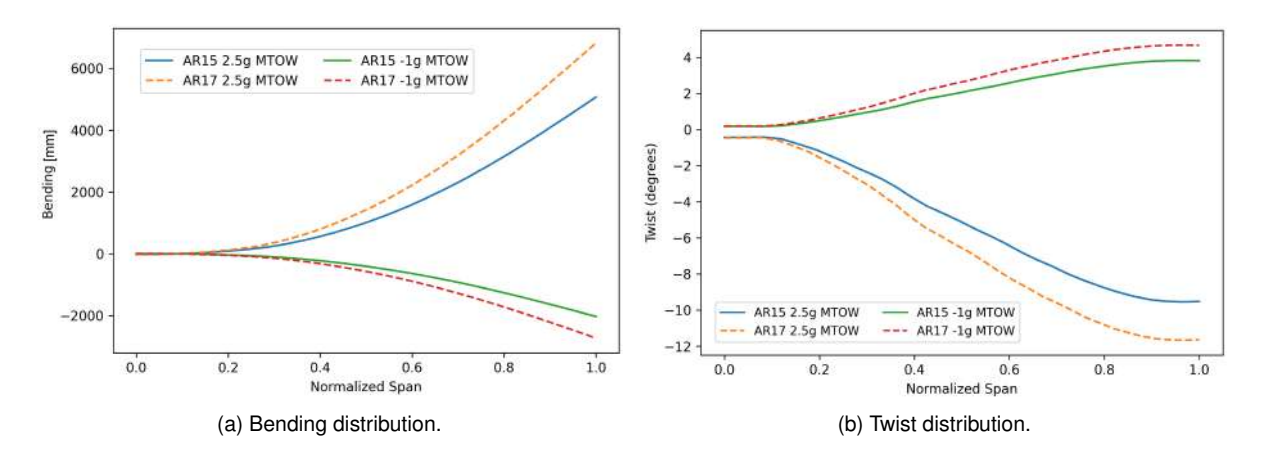


Figure 6.9: Bending and twist distributions prior to structural sizing.

6.4 Static Structural Sizing

The primary focus of the structural sizing is the wing skin, as it plays a fundamental role in aeroelastic tailoring and constitutes one of the main contributors to the wingbox weight. The emphasis on the optimisation of the skin is reflected in the more stringent design constraints imposed upon it, particularly in terms of manufacturing. Moreover, in this work, the skin is qualitatively representative of the changes on the stringers and spars during the structural sizing process. For these reasons, when discussing the optimisation results, particular emphasis will be placed on the skin.

Furthermore, the structural components of the F25-AR17 demonstrate a qualitatively similar response to structural sizing as those of the F25-AR15. Consequently, the main body of this work primarily focuses on presenting the results pertaining to the F25-AR15 configuration.

6.4.1 Wingbox Mass

The variation in wingbox structural mass as constraints are added throughout the static structural sizing is presented in Table 6.5. As expected, the wingbox mass of the preliminary F25-AR17 is heavier than that of the F25-AR15, with a difference of 5.41% (298 kg). This difference can be attributed to the additional material required due to the 7.5% larger wing area of the F25-AR17, as well as its thicker structural components at the wing root, necessary due to the higher wing root bending moment associated with the increase in aspect ratio.

Table 6.5: Wingbox structural mass throughout the static structural sizing.

	F25-AR15				F25-AR17			
	Baseline	Strength	Buckling	Manufacturing	Baseline	Strength	Buckling	Manufacturing
Mass [kg]	4,238	4,589	4,631	5,507	4,503	4,915	4,955	5,805
Variation	Ref.	+8.28%	+9.27%	+29.94%	Ref.	+9.15%	+10.04%	+28.91%

Moreover, as anticipated in the previous section, the wingbox mass grows substantially to satisfy the imposed constraints. Compared to the F25-AR15 and F25-AR17 baseline configurations, the wingbox mass of the preliminary designs is 29.94% (1,269 kg) and 28.91% (1,302 kg) heavier, respectively. The increase in wingbox mass is particularly pronounced when manufacturing requirements are incorporated, with the structural mass increasing by 20.67% (876 kg) and 18.87% (850 kg) for the F25-AR15 and F25-AR17, respectively. This striking increase in mass suggests that manufacturing requirements are the primary design driver in the structural sizing optimisation. The underlying reason for the significant impact of manufacturing requirements on structural mass will become clear when examining the variation of skin thickness as constraints are added to the static structural sizing.

6.4.2 Wingbox Deformation

The increase in wingbox mass suggests that the wing has become stiffer. This is confirmed by the reduction in wingtip bending throughout the static structural sizing, as listed in Table 6.6.

Table 6.6: Wingtip displacement throughout the static structural si	zing (in mm).

Loading Condition			F25-AR15			F25-AR17			
	,	Strength	Buckling	Manufacturing	Strength Buckling Manufacturi		Manufacturing		
MTOW	Pull-up Push-over	3.993 -1.597	3.978 -1.591	3.807 -1.523	5.256 -2.102	5.241 -2.097	5.023 -2.009		

Figure 6.10 presents the bending and twist distribution under push-over and pull-up manoeuvres with MTOW after the static structural sizing. Due to its higher aspect ratio, the F25-AR17 exhibits greater deformations, with a 31.94% larger wingtip displacement under a pull-up condition, which corresponds to the most critical deformation scenario considered.

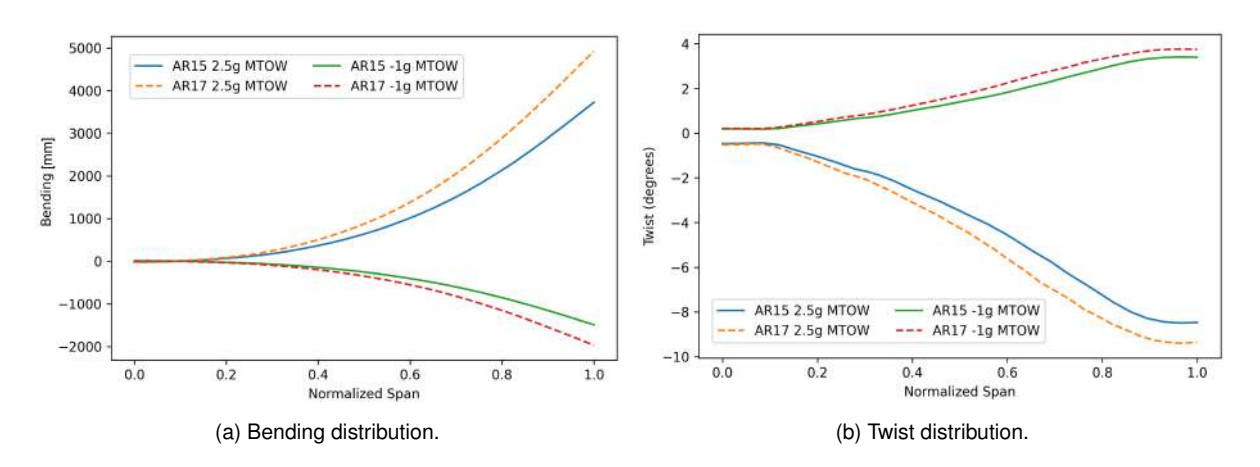


Figure 6.10: Bending and twist distributions after static structural sizing.

Comparing the deformations of the designs resulting from the preliminary structural sizing, Figure 6.10, with those of the baseline configurations, depicted in Figure 6.9, it is evident that the structural sizing has yielded a significantly stiffer wing.

6.4.3 Wing Skin Thickness

Figure 6.11 illustrates the change in the upper skin thickness of the F25-AR15 wing as constraints are progressively introduced throughout the static structural sizing. The importance of manufacturing constraints in wing design is evident from the significance of the changes they induce. Prior to the incorporation of these constraints, strength and buckling requirements could be satisfied by a few significantly thicker skin patches at specific locations, resulting in abrupt thickness variations to adjacent regions. However, such designs are not realistic. The incorporation of manufacturing constraints ensures smooth thickness variations, making the design feasible for production.

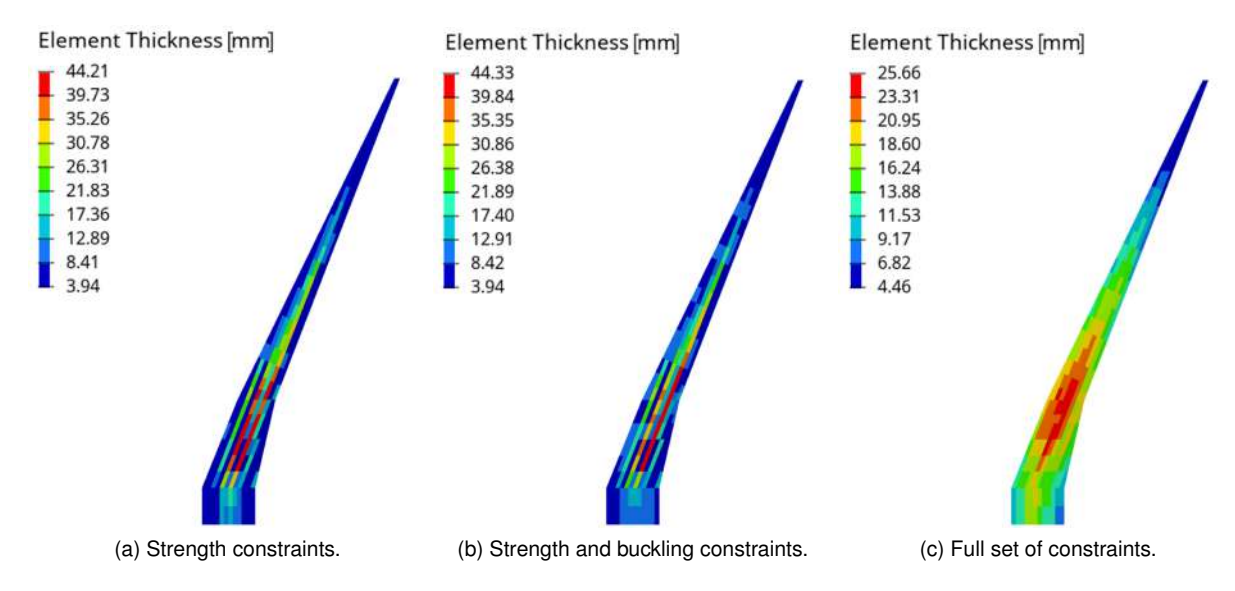


Figure 6.11: F25-AR15 wing upper skin thickness distribution throughout the static structural sizing.

The skin is thicker in the vicinity of the pylon, where the combined effects of bending moment and engine weight results in the highest structural loads. While this trend is already partially visible when considering only strength and buckling constraints, it becomes more pronounced with the inclusion of manufacturing requirements. From this highly loaded region, the thickness gradually tapers to the minimum allowable of 4 mm towards the wingtip. The upper skin thickness distribution of the F25-AR17 wing follows the same trends observed on the F25-AR15 (see Figure A.1 in Appendix). While both aircraft variants exhibit qualitatively similar characteristics, the F25-AR17 wing has a thicker skin near its root, due to its higher wing root bending moment.

Figure 6.12 presents the lower skin thickness distribution of the F25-AR15 wing throughout the static structural sizing. The corresponding results for the F25-AR17 wing exhibit similar behaviour (see Figure A.2 in Appendix). In the lower skin, similar trends to those observed in the upper skin emerge as constraints are introduced, with the skin being thicker in the engine location. In Figure 6.12c the ramp rate constraint and the minimum thickness of 20 mm in the pylon region are clearly distinguishable, with the thickness gradually decreasing from there to the minimum allowable of 6 mm towards the wingtip.

The introduction of manufacturing constraints in the static structural sizing results in a reduction of the maximum wing skin thickness, however there is a significant increase in its structural weight.

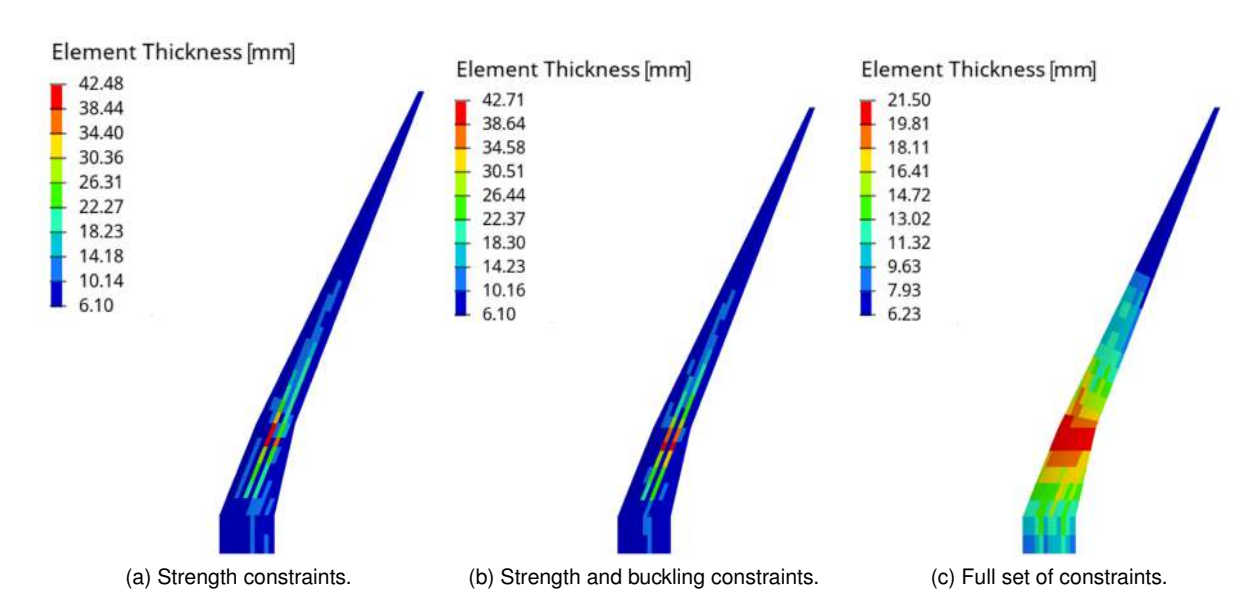


Figure 6.12: F25-AR15 wing lower skin thickness distribution throughout the static structural sizing.

In the absence of such constraints, the strength and buckling criteria could be satisfied with a few significantly thicker skin patches, allowing adjacent areas to remain relatively lightweight. However, when constraints are imposed to ensure a gradual variation in thickness and ply share, the surrounding regions must also be thickened. These regions can consequently carry a greater proportion of the loads, resulting in a more distributed load across a wider surface area. This redistribution reduces the maximum load, and ultimately, the overall maximum thickness required. However, despite the reduction in maximum thickness, with the enforcement of ramp rate requirements, the necessary thickness must now taper smoothly, leading to a larger surface area with increased thickness. The effect of this increased area outweighs the reduction in maximum thickness, resulting in a net increase in structural mass.

The average runtime per iteration for the static structural sizing was approximately 12 minutes. When manufacturing constraints were added the average runtime quadrupled, highlighting the complexity these constraints introduce to the design space. All optimisation tasks were executed on a HPC system equipped with CPUs operating at a base frequency of 2.0 GHz, 128 physical cores, and 256 GB of RAM.

The static structural sizing has yielded feasible preliminary designs for the subsequent optimisations.

6.5 Aeroelastic Structural Sizing

Once the static structural sizing has been completed, the resulting preliminary designs serve as a good starting point for the aeroelastic structural sizing optimisations.

6.5.1 Wingbox Mass and Deformation

In Table 6.7, the structural mass of the wingbox after aeroelastic structural sizing is presented. The F25-AR17 wingbox is 5.51% (293 kg) heavier than the F25-AR15, for the same reasons previously dis-

cussed. Compared to the preliminary configurations, the wingbox mass was reduced by 3.36% (185 kg) for the F25-AR15 and by 3.27% (190 kg) for the F25-AR17.

Table 6.7: Wingbox structural mass after aeroelastic structural sizing.

		F25-A	R15	F25-AR17			
	Static	Aeroelastic	Mass reduction	Static	Aeroelastic	Mass reduction	
Mass [kg]	5,507	5,322	-3.36% (-185 kg)	5,805	5,615	-3.27% (-190 kg)	

This reduction in wingbox mass results from the optimiser's ability to now fully exploit aeroelastic tailoring, tuning the elastic properties of the structure to influence its deflected shape to generate more favourable aerodynamic loads during flight. This is particularly effective in high aspect-ratio composite wings, where the directional properties of the laminate can be finely tuned to shift the aerodynamic loads inboard, reducing the wing root bending moment with passive load alleviation, and consequently, leading to mass savings.

The elastic properties of high aspect-ratio composite wings can be leveraged through aeroelastic tailoring with wing washout, whereby upward bending of the wing under load induces a nose-down twist, reducing the angle of incidence at the wingtips, consequently limiting aerodynamic loads in this region and increasing them inboard, thereby promoting passive load alleviation. The washout in the designs resulting from aeroelastic structural sizing is evident when comparing the increased twist of both aircraft variants in Figure 6.13b, with those obtained from static structural sizing, shown in Figure 6.10b.

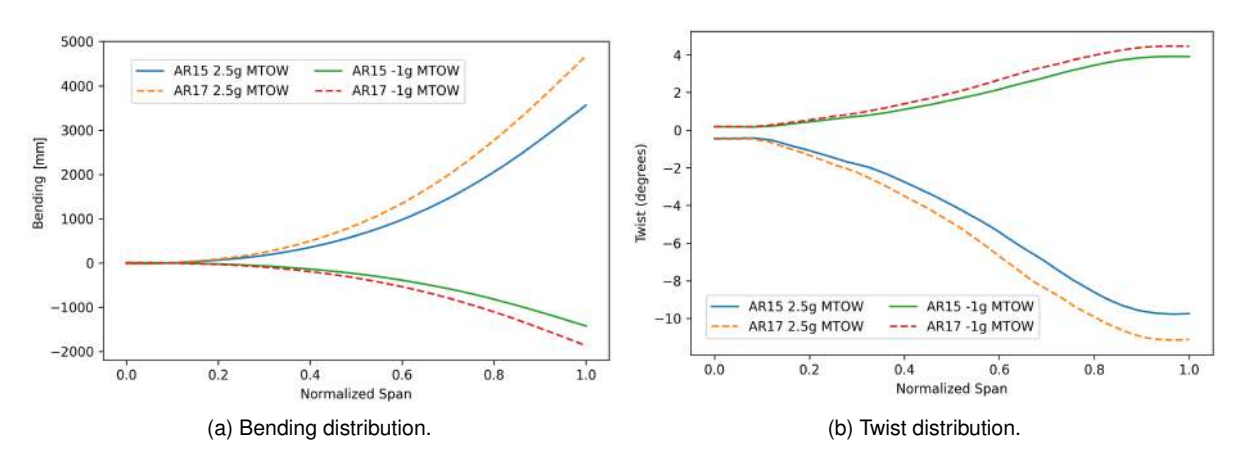


Figure 6.13: Bending and twist distributions after aeroelastic structural sizing.

6.5.2 Wing Skin Thickness

The wing skin thickness distribution after aeroelastic structural sizing is presented in Figure 6.14. In general, the skin thickness for both aspect ratios is very similar, with the thickness increasing in the vicinity of the pylon region in both the upper and lower skins. However, the F25-AR17 has a thicker skin at the wing root due to its higher wing root bending moment.

The wing skin thickness resulting from the aeroelastic structural sizing is lower than that obtained

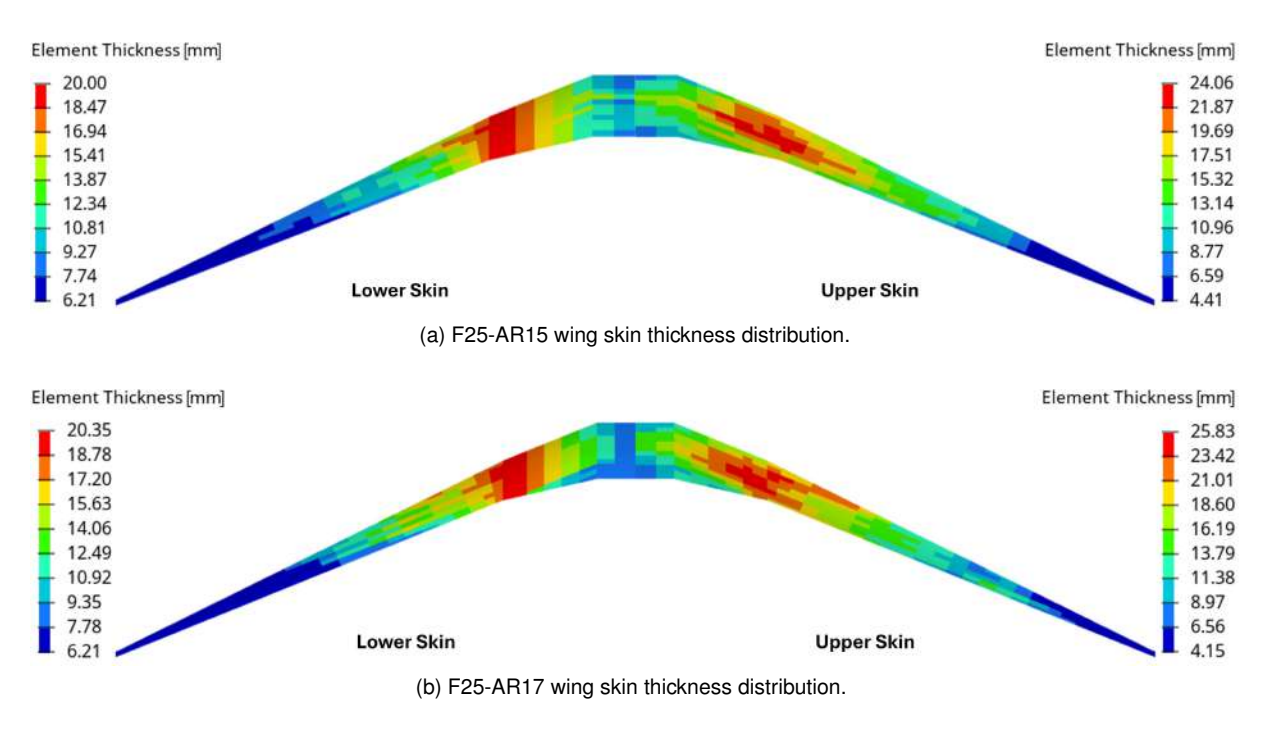


Figure 6.14: Wing skin thickness after aeroelastic structural sizing.

through static structural sizing, as the lift distribution is shifted inboard through aeroelastic tailoring. This reduces the aerodynamic lever arm, leading to a lower wingbox structural mass. Nevertheless, the static structural sizing provided a good starting point for the aeroelastic optimisation.

In both aspect ratios, the spars and stringers exhibit qualitatively similar behaviour to that of the wing skin after aeroelastic structural sizing. Their thickness increases near the engine and wing root to accommodate the loads and bending moment. However, unlike in the wing skin, no manufacturing constraints were imposed, leading to more pronounced thickness variations between adjacent patches. The dimensions of these components after aeroelastic structural sizing are provided in Figure A.3 and A.6 in Appendix for the F25-AR15 and F25-AR17, respectively.

6.5.3 Wing Skin Ply Shares

The distribution of ply shares across the wing skin provides valuable insights into how the optimiser leverages the properties of each ply direction to efficiently accommodate the loads in different regions of the wing. The ply shares were bounded by the upper and lower limits defined in Section 6.1.4. Figure 6.15 presents the ply share distribution for the 0° , $\pm 45^{\circ}$, and 90° plies in the upper skin of the F25-AR15 wing after aeroelastic structural sizing. The ply share distributions for the lower skin and the F25-AR17 wing are analogous to these and are presented in Appendix in Figures A.4 and A.7, respectively.

The 0° plies constitute a significant portion of the total ply share across the wing skin. Their contribution is most pronounced at two specific locations: the leading edge, and the trailing edge of the inner wing section. Their presence diminishes progressively towards the wingtip. This distribution is consistent with structural expectations as, in the inner wing section, the principal load direction is well aligned with the 0° plies, which can therefore provide a good strength-to-weight ratio.

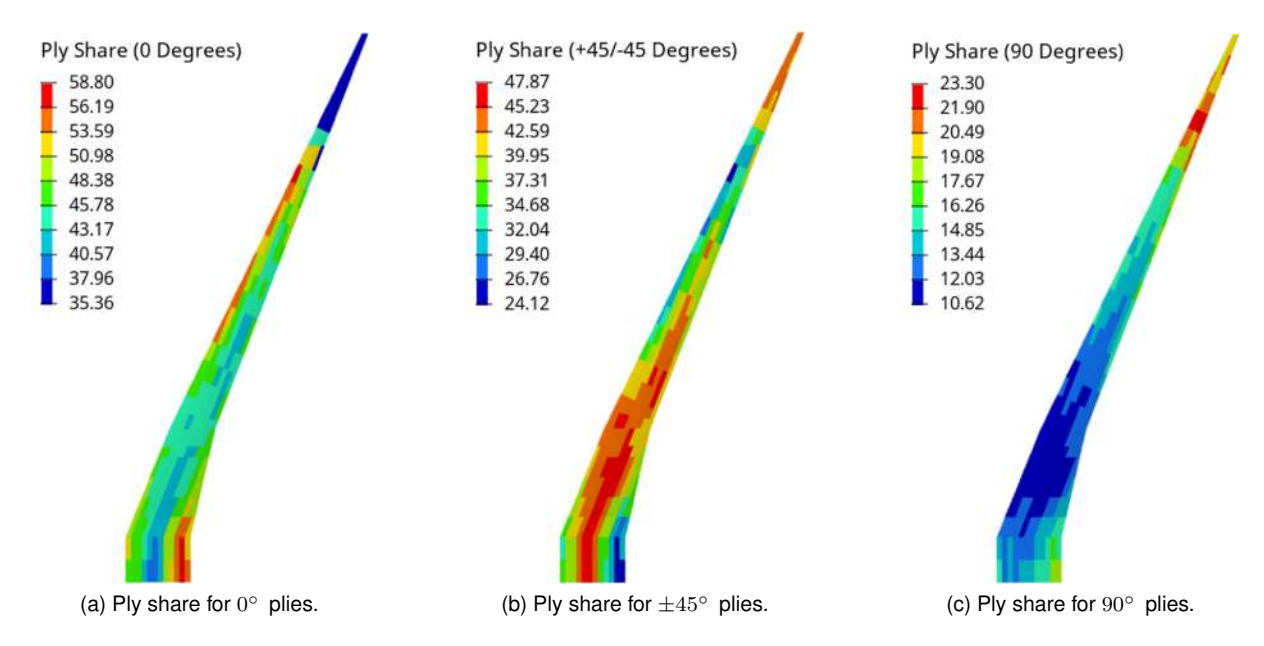


Figure 6.15: F25-AR15 wing upper skin ply share distribution after aeroelastic structural sizing.

The $\pm 45^\circ$ plies also constitute a significant portion of total ply share, particularly in the middle section of the wing skin, and, in conjunction with the 0° plies, form the majority of the laminate. Given that both aspect-ratio wings have a sweep of approximately 25° , the observed trend to favour $\pm 45^\circ$ plies towards the middle section of the wing is consistent with the need to carry loads along the span. Furthermore, these plies contribute to the laminate's capacity to withstand in-plane shear stresses in this region.

The 90° plies play a less significant role in the composite wing structure. Before the application of manufacturing constraints, their ply share was less than 10% in most regions. From a load-bearing perspective, this distribution is reasonable, as these plies are not well aligned with the majority of loads. Overall, the highest share of 90° plies is found near the wingtip, while the remainder of the wing tends to the imposed minimum.

6.5.4 Wing Skin Reserve Factors

Following the structural sizing, it is important to assess which types of constraints were most critical. This assessment is carried out by examining their respective Reserve Factors (RF). The reserve factor quantifies the margin of compliance with a given constraint and is defined as the ratio between the allowable limit and the current design value,

$$RF = \frac{Allowable Limit}{Actual Value},$$
 (6.1)

where the allowable limit refers to, for example, the maximum strain, critical buckling load, or ramp rate and the actual value is the predicted value from the analysis. A reserve factor greater than one indicates that the constraint is satisfied with a safety margin, whereas a reserve factor equal to unity signifies that the constraint is active, meaning it is exactly at its permissible limit. Conversely, a reserve factor less than one denotes a constraint violation.

Figure 6.16 illustrates the strength, buckling, and manufacturing reserve factors on the upper skin of the F25-AR15 wing following aeroelastic structural sizing. The reserve factors for the lower skin, as well as those of the F25-AR17 wing, exhibit similar trends and are presented in Figures A.5 and A.8 in Appendix.

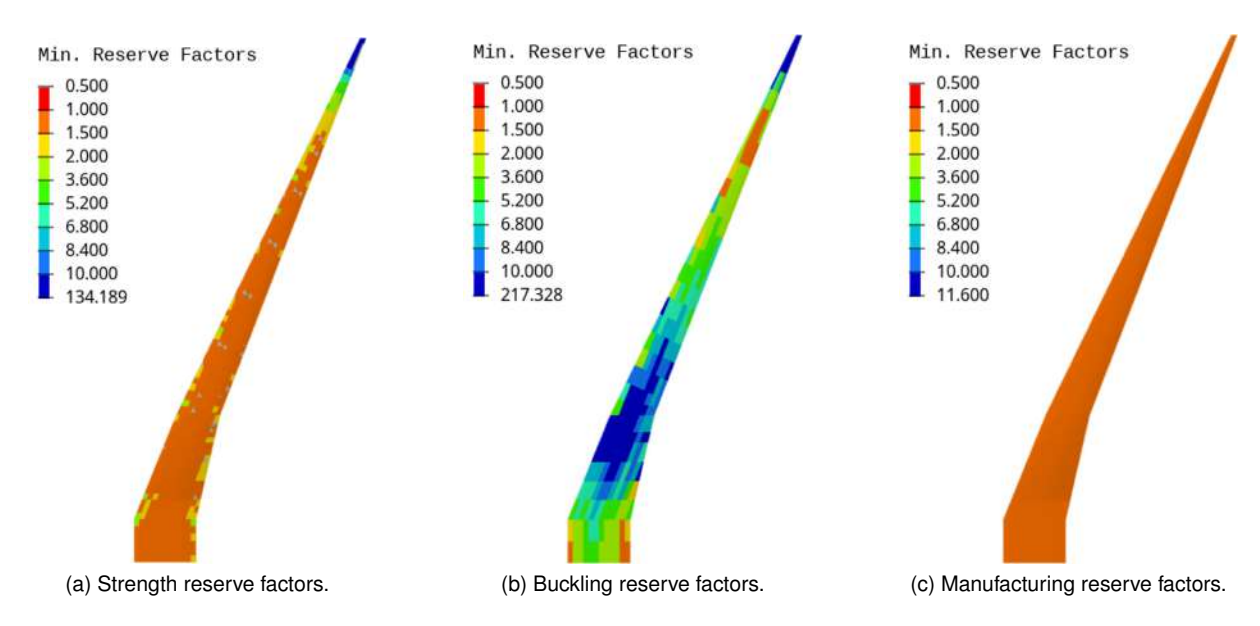


Figure 6.16: F25-AR15 wing upper skin reserve factors after aeroelastic structural sizing.

After structural sizing, no constraint violations (RF < 1) were observed in any wing skin patches. Manufacturing requirements constitute the most dominant constraints in the design, followed by strength and, subsequently, buckling criteria. Across the entire wing skin, manufacturing constraints remain active, or nearly active, with the reserve factor approaching unity, confirming that manufacturability is the dominant limitation for further mass savings. This is consistent with observations from the skin thickness distribution, wherein manufacturing requirements were the design driver that dictated the thickness of most skin patches. Strength constraints become increasingly active towards the wing root, playing a dominant role in driving the structural sizing in this region, alongside manufacturing criteria. In contrast, buckling has a relatively minor influence on the structural sizing, as a consequence of the imposed minimum rib and stringer pitches.

The aeroelastic structural sizing had an average runtime per iteration of approximately 62 minutes, which is over five times longer than that of the static structural sizing. This increase is due to the inclusion of full aeroelastic effects in the analysis. However, since the static structural sizing provided a good initial design for the aeroelastic optimisation, the latter converged in significantly fewer iterations. This demonstrates the advantage of the used approach, whereby a feasible preliminary design is first established by neglecting aeroelasticity, before proceeding to the aeroelastic structural sizing optimisation.

Overall, the aeroelastic structural sizing has yielded two feasible high aspect-ratio composite wings.

6.6 Performance Analysis

One of the primary objectives of this work is to investigate the effects of increasing the aspect ratio on transport aircraft performance. To this end, following the structural sizing, the high-fidelity aerostructural analysis described in Chapter 4 is used to evaluate the performance of both aircraft. The key metrics to be evaluated are the in-flight twist and lift distribution, and the drag during cruise. Additionally, as the relationship between aspect ratio and aircraft performance is inherently multidisciplinary, the Breguet range for both models is estimated and compared.

The aerostructural analyses for performance were carried out under cruise conditions at a Mach number of 0.78 and an altitude of 10,363 metres, corresponding to a Reynolds number of 22 million.

6.6.1 In-flight Twist Distribution

Figure 6.17 presents the twist distribution in cruise for both aircraft variants. A significant wing washout is observed in both aircraft, with the wings twisted nose-down from root to tip. As a result of the decreasing twist, the angle of incidence, and consequently, the lift are reduced at the wingtip, effectively shifting the lift distribution inboard. The washout is more pronounced in the higher aspect-ratio wing, suggesting a greater passive load alleviation as the aspect ratio increases.

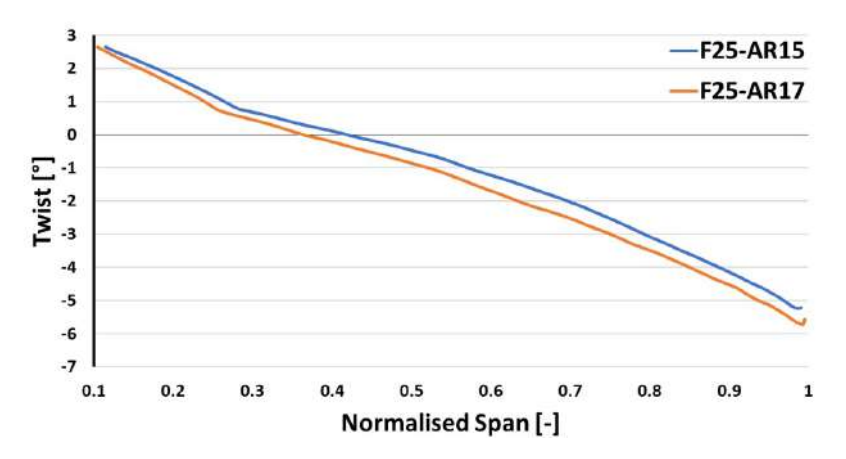


Figure 6.17: Twist distribution in cruise.

This desired twist distribution in cruise is achieved solely through aeroelastic tailoring, as the jig twist is not included as a design variable in the present optimisations.

6.6.2 Lift Distribution

Figure 6.18 illustrates the lift distribution in cruise for both aircraft models. The lift distributions closely resemble the classical bell-shaped distribution, originally proposed by Prandtl in 1933 as the aerostructurally optimal lift distribution for a wing design with variable span and constant weight [50].

The wing washout, obtained through aeroelastic tailoring, gives rise to this bell-shaped lift distribution which provides passive load alleviation. Compared to the aerodynamically optimal elliptical distribution [47], the bell-shaped distribution yields reduced lift near the wingtips, effectively shifting the loads

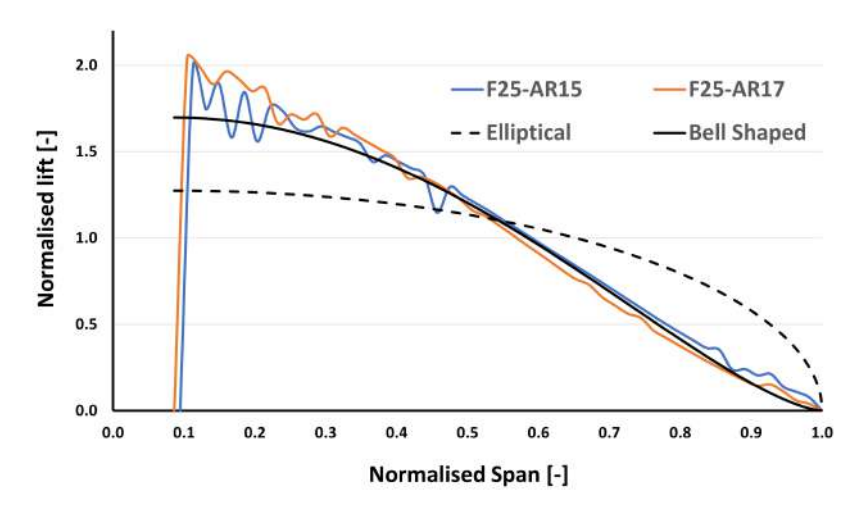


Figure 6.18: Lift distribution in cruise.

inboard. This inward shift decreases the aerodynamic lever arm, thereby reducing the mass-driving maximum wing root bending moment.

This passive load alleviation is more pronounced in the higher aspect-ratio configuration. Specifically, the F25-AR17 generates a higher lift loading up to approximately 40% of the span, whereas the F25-AR15 exhibits greater lift beyond this point. This observation is consistent with the more pronounced wing washout observed in the F25-AR17. Despite this fact, the wing root bending moment in cruise for the F25-AR17 is still 5.97% higher than that of the F25-AR15.

6.6.3 Drag Decomposition

Table 6.8 presents a comparison of wing drag during cruise between the F25-AR17 and F25-AR15. For both aircraft, the reference area considered is the F25-AR15 wing surface area. As anticipated, the F25-AR17 wing has a higher friction drag, by approximately 10.23%, attributable to its larger wetted surface area. However, this increase is offset by a 6.63% reduction in wing pressure drag relative to the F25-AR15. The net outcome is a 1.42% drag reduction for the higher aspect-ratio wing.

Table 6.8: Comparison of wing drag counts in cruise between the F25-AR17 and F25-AR15.

Wing Drag Counts	F25-AR17	F25-AR15	Δ AR17 - AR15
Pressure Friction	90.1 48.5	96.5 44.0	-6.63% +10.23%
Total	138.6	140.5	-1.42%

Moreover, the fuselage of the higher aspect-ratio aircraft experiences a 4.01% reduction in pressure drag compared to the F25-AR15. Overall, the higher aspect-ratio aircraft achieves a total drag reduction of 2.14%, thereby highlighting the aerodynamic advantages of increasing the wing aspect ratio in the investigated design point.

6.6.4 Breguet Range

To ensure a fair comparison between the Breguet range of both aspect ratio aircraft, while maintaining a simplified idealisation, several assumptions were made. The MTOW was fixed as a top-level requirement for both aircraft, and any increase in structural mass during the optimisations directly affected the available payload. Given that the F25-AR17 has a higher structural mass, it was assumed that this configuration would have less payload capacity. Under this assumption, the initial and final masses for the Breguet range estimation are defined as $M_{\rm initial} = MTOW$ and $M_{\rm final} = MTOW - M_{\rm fuel}$. The fuel mass of 10,590 kg [137] was the same for both configurations.

Considering the cruising altitude of 10,363 m, a Mach number of 0.78 and a TSFC of 14.33 g/kN/s [30] for both aspect ratios, the Breguet range was estimated according to Equation (4.1). The F25-AR15 yielded a Breguet range of 4,666 km, while the F25-AR17 achieved a slightly longer Breguet range of 4,768 km. This represents a 2.18% increase in Breguet range for the higher aspect-ratio configuration.

Chapter 7

DLR-F25 Structural Sizing for Maximum Aerodynamic Efficiency or Breguet Range

In this chapter, the structural sizing optimisations with aerodynamic efficiency and Breguet range as the objective functions are presented. The chapter begins with an overview of the revised structural sizing optimisation process and the definition of the newly formulated optimisation problems. Subsequently, the results of the structural sizing optimisations for the new objective functions are analysed. A detailed discussion on the influence of aspect ratio and objective function on overall aircraft performance follows.

7.1 Problem Definition

After completing the conventional structural sizing for mass minimisation and evaluating the performance of both aspect ratios, the natural question arises as to how the design might be affected if alternative optimisation objectives were considered. Accordingly, in addition to the classical objective of minimising structural mass, two further objectives are introduced for the structural sizing: (i) the maximisation of aerodynamic efficiency, and (ii) the maximisation of Breguet range.

Aerodynamic efficiency is selected as one of the objective functions of interest to provide a contrast with the conventional mass-minimisation approach, and the Breguet range is used to provide a trade-off between structural and aerodynamic metrics.

While the mass objective can be directly obtained from the structural model during the structural sizing process without the need for additional calculations, the newly introduced objective functions require additional computations to estimate drag. Since drag can only be accurately predicted with high-fidelity aerodynamics, these new optimisations with drag-dependent objectives necessitate a high-fidelity aerostructural analysis, such as the one used in the performance evaluation, to estimate the aerodynamic loads for the new objective functions.

Consequently, a new aerostructural design process is put in place, integrating the high-fidelity aerostructural analysis model for performance outlined in Chapter 4 within the conventional structural sizing process, described in Chapter 3. Therefore, this new aerostructural design process includes two major analysis modules: (1) the loads model, presented in Section 3.3, which computes the loads that drive the structural sizing using linear aerodynamics, and (2) the high-fidelity coupled aerostructural analysis, needed to evaluate the drag-dependent objective functions. The XDSM diagram of the new optimisation process used for the aerodynamic efficiency and Breguet range objectives is shown in Figure 7.1.

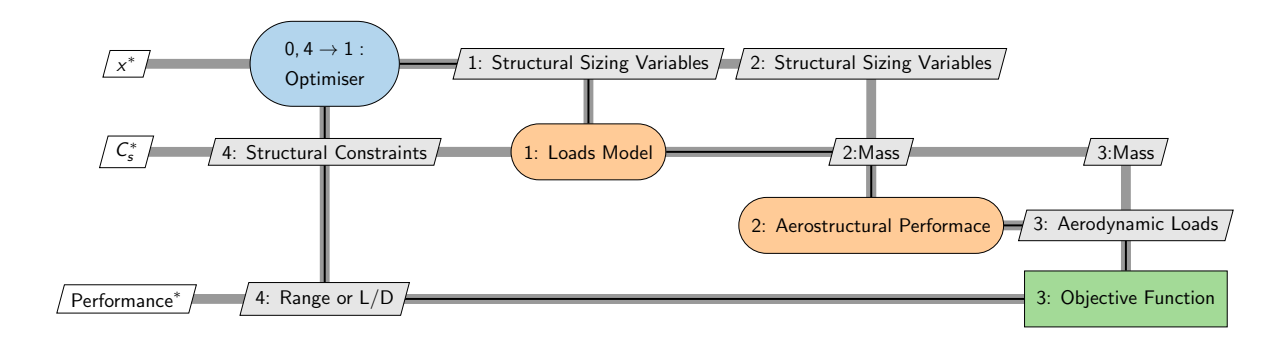


Figure 7.1: Structural sizing optimisation process for aerodynamic efficiency or Breguet range.

The new optimisation studies are conducted using the same high-fidelity multidisciplinary design optimisation framework [25, 26, 132] previously used for the performance evaluation. The aerodynamic, structural, and coupling models used in both fidelity aerostructural analyses are consistent with those previously presented in Chapter 5. Furthermore, the problem definition remains identical to that outlined in Section 6.1, with the exception of the objective functions. In the high-fidelity aerostructural analysis, both aircraft are trimmed to achieve the same target lift force. Consequently, the comparison of aerodynamic efficiency between two designs reduces to a comparison of the corresponding drag generated at that operating point.

The starting points for these new optimisations are the designs obtained from the conventional structural sizing for mass, presented in Section 6.5. The results of the conventional structural sizing of the F25-AR15 serve as the reference in the following optimisations studies.

7.2 Structural Sizing for Aerodynamic Efficiency

Starting from the mass-optimal designs, the optimisation process illustrated in Figure 7.1 is used to perform the structural sizing of both aspect-ratio aircraft for aerodynamic efficiency. The optimisations converge quickly and smoothly, however only the final iterations yielded feasible designs.

The convergence history of these optimisations is presented in Figure 7.2. The aerodynamic efficiency of the F25-AR15 increases 6.00%, albeit at the expense of a 1.89% increase in MTOW. Similarly, the F25-AR17 aerodynamic efficiency improved 7.86% at the cost of a 3.54% increase in MTOW, compared to its mass-optimal design. These results highlight the distinct design characteristics that emerge when aerodynamic efficiency is prioritised over structural weight.

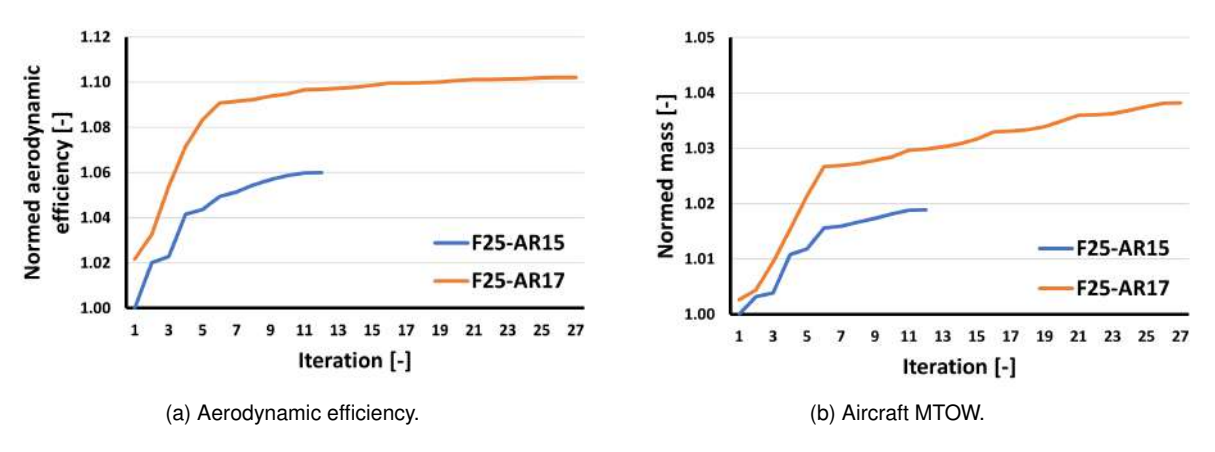


Figure 7.2: Convergence history of the structural sizing optimisations for aerodynamic efficiency.

The improvements in aerodynamic efficiency, relative to the conventional structural sizing, are due to a reduction in pressure drag. This reduction arises from a more favourable lift distribution, with the centre of lift shifting outboard by more than 10%, as illustrated in Figure 7.4. As a consequence of this shift, the wing root bending moment increases by more than 10%, thereby increasing the mass. In the conventional structural sizing, minimising the wing root bending moment through passive load alleviation is crucial for mass reduction, however, when the design objective shifts towards aerodynamic performance, this consideration is deprioritised.

When comparing the two aspect ratio configurations, the F25-AR17 exhibits a 3.98% higher aerodynamic efficiency due to its 3.83% lower drag. This emphasises the potential of higher aspect-ratio wings to improve aerodynamic performance at the investigated conditions.

7.3 Structural Sizing for Breguet Range

Following the optimisations for structural and aerodynamic performance metrics, Breguet range was selected as the objective function. The starting points for these optimisations were also the designs obtained from the conventional structural sizing. Figure 7.3 presents the convergence history of the structural sizing optimisations for Breguet range.

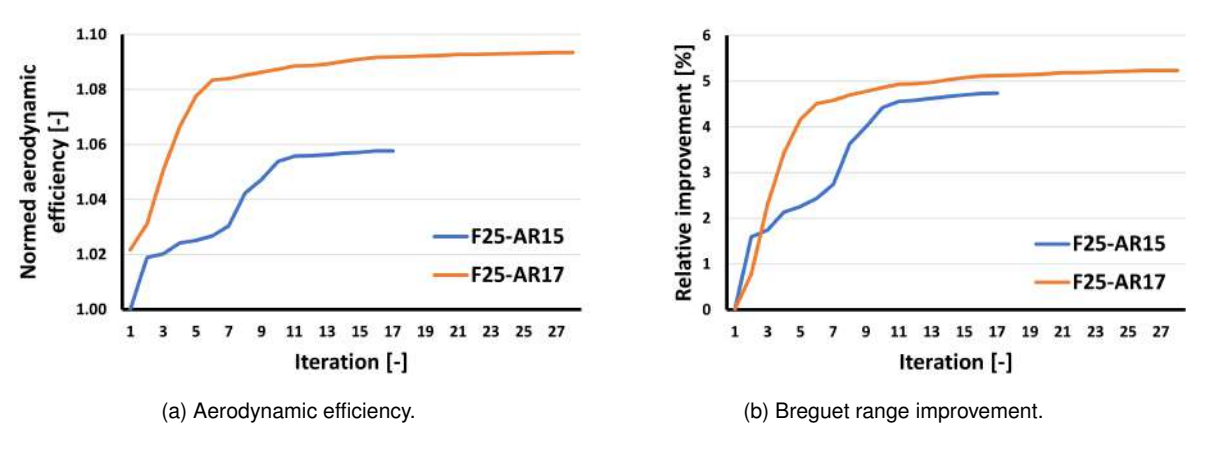


Figure 7.3: Convergence history of the structural sizing optimisations for Breguet range.

The Breguet range improved by 4.73% and 5.23% for the F25-AR15 and F25-AR17, respectively. Relative to their mass-optimal counterparts, the designs optimised for Breguet range achieve aerodynamic efficiency improvements of 5.77% and 7.03% for the F25-AR15 and F25-AR17, respectively, albeit at the expense of a 0.93% and 1.59% increase in MTOW. The aerodynamic efficiency gains realised are comparable to those obtained under the aerodynamic efficiency objective, while simultaneously offering substantial mass savings. This highlights the potential of the Breguet range to achieve a favourable trade-off between structural and aerodynamic efficiency under the investigated conditions.

The drag reduction associated with the higher aspect-ratio wing is also observed in the optimisations for Breguet range. The F25-AR17 exhibits a 3.38% higher aerodynamic efficiency due to its 3.27% lower drag, highlighting the aerodynamic advantages conferred by the higher aspect ratio in this context.

Table 7.1 presents a summary of the structural and aerodynamic characteristics of the designs resulting from the distinct optimisation objectives. Furthermore, the influence of aspect ratio is examined by comparing the designs of both aircraft variants optimised for the same metric.

	Mass			Aerodynamic Efficiency			Breguet Range		
	MTOW	L/D	C_D	MTOW	L/D	C_D	MTOW	L/D	C_D
F25-AR15	Ref.	Ref.	Ref.	1.89%	6.00%	-5.66%	0.93%	5.77%	-5.45%
F25-AR17	0.27%	2.18%	-2.14%	3.82%	10.21%	-9.27%	1.86%	9.34%	-8.54%

3.98%

-3.83%

0.92%

3.38%

-3.27%

1.89%

Table 7.1: Structural and aerodynamic characteristics of the optimised designs.

The average runtime per iteration for the primal solution was approximately 1 hour and 20 minutes, with roughly half of this time allocated to the loads model and the other half to the high-fidelity aerostructural analysis. The sensitivity analysis required about 2 hours per iteration, again with an even distribution between the loads model and the performance analysis. Compared to the structural sizing optimisations for mass, the average runtime per iteration of the optimisations with drag-dependent objectives was over three times longer. This was due to the computationally expensive high-fidelity aerostructural analysis required to compute the drag-dependent objectives.

7.4 Lift Distributions

0.27%

2.18%

-2.14%

AR impact

Figure 7.4 illustrates the lift distributions after the structural sizing optimisations considering mass, aerodynamic efficiency, and Breguet range as the objective functions. All optimisation cases exhibit lift distributions that closely resemble the bell-shaped distribution proposed by Prandtl in 1933 [50].

For both aspect ratios, the structural sizing optimisations aimed at reducing finite element mass shift the aerodynamic loads inboard, through passive load alleviation, to reduce the wing root bending moment, which is one of the main contributors to structural mass in wing design. The optimisations for aerodynamic efficiency and Breguet range produce lift distributions that are very similar and start tending towards an elliptical profile, highlighting the prioritisation of drag reduction in these objectives.

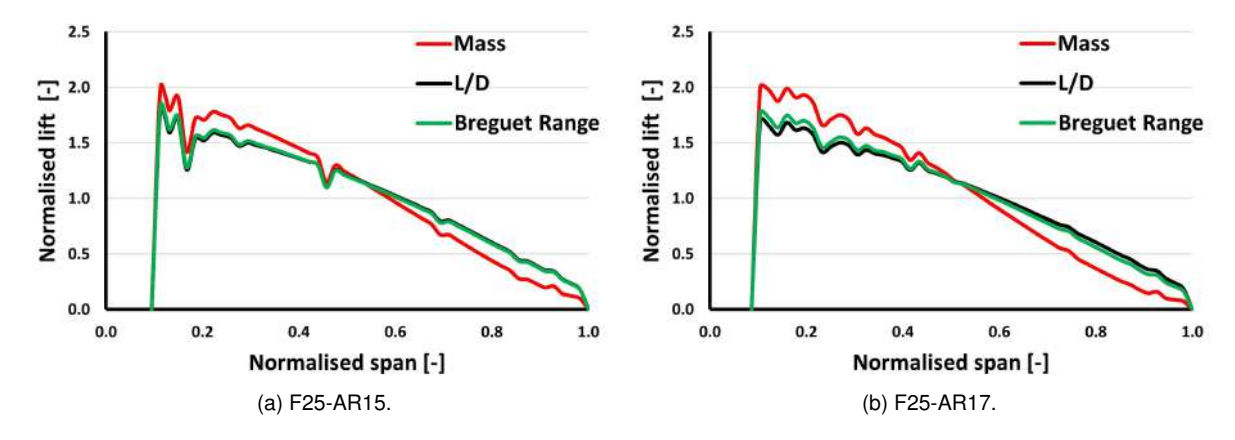


Figure 7.4: Lift distributions for the structural sizing optimisations for mass, aerodynamic efficiency, and Breguet range.

7.5 Pareto Fronts

Based on the three optimal design points, corresponding to the minimisation of structural mass, the maximisation of aerodynamic efficiency, and the optimisation of Breguet range, the estimated Pareto fronts for both aspect ratios are presented in Figure 7.5.

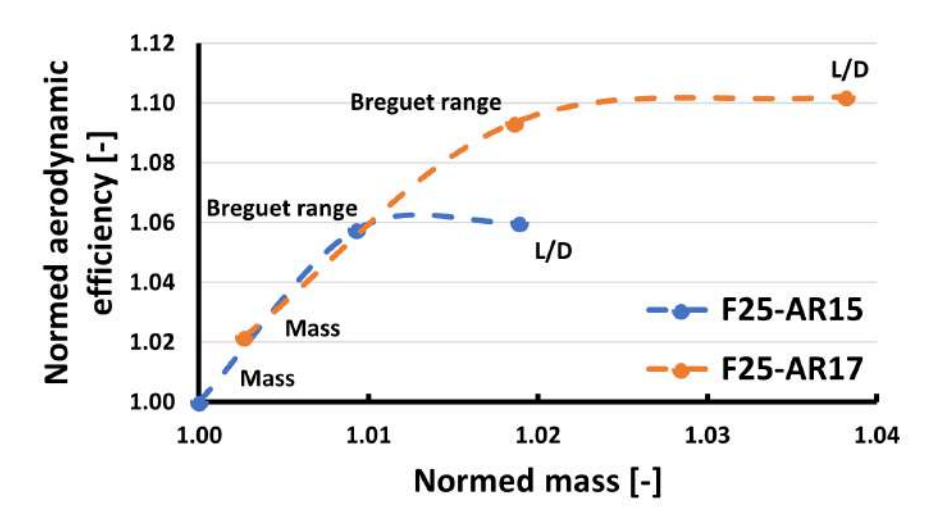


Figure 7.5: F25-AR15 and F25-AR17 Pareto fronts.

When comparing the results of the first two optimisation cases, which focused on a single discipline objective, with those obtained by optimising for the Breguet range, it becomes clear that the latter achieves a better trade-off between structural and aerodynamic efficiency for the investigated design points.

Both aspect ratios offer markedly different characteristics in terms of mass and aerodynamic efficiency. For short-range missions, the F25-AR15 configuration is more favourable due to its lower structural weight. Conversely, for longer missions, the F25-AR17 offers superior performance as a result of its improved aerodynamic efficiency.

Chapter 8

Conclusions and Future Work

This chapter presents a brief summary of the dissertation and of the main conclusions drawn from this work. The key achievements are outlined, along with a discussion of potential future developments. Recommendations for improving and extending the current structural sizing optimisation process are also provided.

8.1 Summary

The main objective of this work was to investigate the impact of increasing the aspect ratio on the performance of modern transport aircraft. Additionally, the influence of different objective functions on structural sizing design trade-offs was assessed.

To this end, two high aspect-ratio composite wings of short-medium-range transport aircraft underwent aeroelastic structural sizing, and their performances were compared. The optimisations were conducted using Airbus's in-house MDO suite and structural solver Lagrange and DLR's CFD solver TAU. Three distinct objective functions were considered: the classical minimisation of mass, the maximisation of aerodynamic efficiency, and the maximisation of Breguet range. The first two objectives focused on a single discipline, whilst the third facilitated a multidisciplinary trade-off between the structural and aerodynamic domains. A gradient-based algorithm with direct sensitivity analysis was used. The design variables, numbering approximately 3,000, included structural sizing parameters such as the thicknesses and cross-sectional areas of the skin, spars, and stringers. Constraints reflected industry requirements and encompassed structural strength, buckling stability, and manufacturing criteria.

Washout in the composite wing was induced solely with aeroelastic tailoring, providing passive load alleviation through a bell-shaped lift distribution. This strategy effectively reduced the wing root bending moment, a primary driver of structural mass in the design of high aspect-ratio wings.

From the analysis of the mass-optimal designs, it was possible to examine how different ply orientations are leveraged across various wing regions to manage loads effectively. It was also determined that manufacturing requirements were the most limiting constraint in achieving further mass savings.

For the investigated design points, the benefits of increasing the aspect ratio in modern transport aircraft were demonstrated, notably the improvement in aerodynamic efficiency and reduction in drag, despite the increase in structural weight. Furthermore, the results captured the markedly different design characteristics that arise from different objective functions, and the value of a multidisciplinary performance-based objective, such as the Breguet range, in effectively guiding design trade-offs during the preliminary design stage.

The optimisations presented in this work did not consider constraints imposed by overall aircraft design or by disciplines beyond structural mechanics. Nonetheless, the findings presented herein may serve as a valuable reference for aircraft designers in informing the early stages of the design process.

8.2 Outlook

Future work should expand the current shape parameter study to more aspect ratios, leveraging Descartes' capabilities to rapidly modify geometries and generate the corresponding analysis and optimisation models, whilst exploiting the opportunity to run these optimisations in parallel.

Moreover, the design space should be widened to include shape variables such as jig twist and aerofoil geometry. To this end, the use of parametric geometries and mesh morphing is recommended. Furthermore, the integration of additional disciplines into the optimisation process, particularly flight control, which is critical for high aspect-ratio configurations, is strongly advised. A broader set of load cases, including gust encounters and aeroelastic phenomena such as flutter, should also be considered to achieve more realistic and robust design outcomes.

Above all, the main conclusion drawn from this work for future investigations is that the results from multidisciplinary design optimisations should serve to inform designers during the decision-making process. This reflects a core value of MDO in the current aerospace industry: to support and improve the design process rather than to replace it. To achieve this, it is essential to critically analyse and interpret the results provided by the optimisation, viewing it not as a black box or a panacea, but as a powerful tool for gaining valuable insights into the design space.

Bibliography

- [1] Clean Sky 2 Joint Undertaking. Clean Sky 2 Development Plan. Technical Report CS2DP-October-2021, European Commision, October 2021.
- [2] E. J. Adler and J. R. R. A. Martins. Hydrogen-powered aircraft: Fundamental concepts, key technologies, and environmental impacts. *Progress in Aerospace Sciences*, 141:100922, 2023. doi: 10.1016/j.paerosci.2023.100922. Special Issue on Green Aviation.
- [3] EUROCONTROL. Aviation Outlook 2050. Technical Report STATFOR Doc 683, April 2022.
- [4] European Commission. Reducing emissions from aviation. https://climate.ec.europa.eu/eu-action/transport/reducing-emissions-aviation_en. Last accessed: 20 November 2024.
- [5] A. Esqué, G. Fuchs and R. Riedel. Fuel efficiency: Why airlines need to switch to more ambitious measures. Technical report, McKinsey & Company Aerospace and Defense, March 2022.
- [6] Clean Aviation Joint Undertaking. Strategic Research and Innovation Agenda. Technical Report CAJU-GB-2021-12-16-SRIA, European Commission, December 2021.
- [7] B. Graver, K. Zhang and D. Rutherford. CO2 Emissions From Commercial Aviation, 2018. Technical Report A40-WP/560, International Coalition for Sustainable Aviation, September 2019.
- [8] E. C. Borrás, M. Fischer, A. Kaysser-Pyzalla, A. Klöckner, D. Kügler, R. Mönig, B. Nagel, C.-C. Rossow and M. Wiedemann. Fit For Change: DLR strategy towards zero-emission aviation. In 33th Congress of the International Council of the Aeronautical Sciences, Stockholm, Sweden, September 2022.
- [9] European Commission. The European Green Deal, COM (2019) 640, 2019.
- [10] F. Afonso, G. Leal, J. Vale, É. Oliveira, F. Lau, and A. Suleman. The effect of stiffness and geometric parameters on the nonlinear aeroelastic performance of high aspect ratio wings. *Proceedings of the Institution of Mechanical Engineers, Part G: Journal of Aerospace Engineering*, 231(10): 1824–1850, 2017. doi: 10.1177/0954410016675893.
- [11] J. R. A. Martins, G. J. Kennedy and G. W. Kenway. High Aspect Ratio Wing Design: Optimal Aerostructural Tradeoffs for the Next Generation of Materials. In 52nd Aerospace Sciences Meeting, National Harbor, Maryland, January 2014. doi: 10.2514/6.2014-0596.

- [12] F. Afonso, J. Vale, É. Oliveira, F. Lau and A. Suleman. A review on non-linear aeroelasticity of high aspect-ratio wings. *Progress in Aerospace Sciences*, 89:40–57, 2017. doi: 10.1016/j.paerosci. 2016.12.004.
- [13] F. Daoud, S. Deinert, R. Maierl, and Ö. Petersson. Integrated multidisciplinary aircraft design process supported by a decentral MDO framework. In 16th AIAA/ISSMO Multidisciplinary Analysis and Optimization Conference, Dallas, Texas, June 2015. doi: 10.2514/6.2015-3090.
- [14] G. K. W. Kenway and J. R. A. Martins. Multipoint High-Fidelity Aerostructural Optimization of a Transport Aircraft Configuration. *Journal of Aircraft*, 51(1):144–160, 2014. doi: 10.2514/1. C032150.
- [15] A. Suleman, F. Afonso, J. Vale, É. Oliveira, and F. Lau. Non-linear aeroelastic analysis in the time domain of high-aspect-ratio wings: Effect of chord and taper-ratio variation. *The Aeronautical Journal*, 121(1235):21–53, 2017. doi: 10.1017/aer.2016.94.
- [16] K. A. James, G. J. Kennedy and J. R. R. A. Martins. Concurrent aerostructural topology optimization of a wing box. *Computers & Structures*, 134:1–17, 2014. doi: 10.1016/j.compstruc.2013.12. 007.
- [17] A. Eberle, B. Stefes, and D. Reckzeh. Clean Aviation Ultra-Performance Wing (UP-Wing). In AIAA SCITECH 2024 Forum, Orlando, Florida, January 2024. doi: doi.org/10.2514/6.2024-2109.
- [18] R. Maierl, Ö. Petersson, F. Daoud. Automated Creation of Aeroelastic Optimization Models from a Parameterized Geometry. In *15th International Forum on Aeroelasticity and Structural Dynamics*, Bristol, United Kingdom, June 2013.
- [19] C. M. Liersch and M. Hepperle. A distributed toolbox for multidisciplinary preliminary aircraft design. *CEAS Aeronautical Journal*, 2:57–68, 2011. doi: 10.1007/s13272-011-0024-6.
- [20] B. Nagel, D. Böhnke, V. Gollnick, P. Schmollgruber, A. Rizzi, G. La Rocca, J. J. Alonso. Communication in aircraft design: Can we establish a common language. In *28th International Congress of the Aeronautical Sciences*. Brisbane, Australia, September 2012.
- [21] M. Alder, C. Liersch, M. Hepperle, R. Maierl, S. Deinert, J. Kleinert, M. Siggel, D. Kohlgrüber, E. Moerland and B. Nagel. 20 years of CPACS: A Brief History and Future Vision of Establishing a Common Language for Aircraft Design. In *Deutscher Luft- und Raumfahrt Kongress DLRK*. Hamburg, Germany, October 2024.
- [22] M. Alder, E. Moerland, J. Jepsen, B. Nagel. Recent Advances in Establishing a Common Language for Aircraft Design with CPACS. In *Aerospace Europe Conference 2020*. Bordeaux, France, February 2020.
- [23] G. Schuhmacher, F. Daoud, Ö. Petersson and M. Wagner. Multidisciplinary Airframe Design Optimization. In 28th International Congress of the Aeronautical Sciences. Brisbane, Australia, September 2012.

- [24] F. Daoud, Ö. Petersson, S. Deinert and P. Bronny. Multidisciplinary Airframe Design Process: Incorporation of steady and unsteady aeroelastic loads. In *12th AIAA Aviation Technology, Integration, and Operations (ATIO) Conference and 14th AIAA/ISSMO Multidisciplinary Analysis and Optimization Conferences*. Indianapolis, Indiana, September 2012.
- [25] F. Volle, M. Abu-Zurayk, A. U. Balani, S. Deinert and Ö. Petersson. Simultaneous Shape and Sizing Optimization for Improving Aircraft Performance Using the Aero-Structure Adjoint. In *Deutsche Luft- und Raumfahrtkongress DLRK*, Stuttgart, Germany, September 2023.
- [26] A. A. Gastaldi, F. Volle, F. Daoud, C. Breitsamter. Simultaneous Airframe Shape and Sizing Optimization Using FlowSimulator and the Lagrange MDO Suite. In *Deutsche Luft- und Raumfahrtkongress DLRK*, Dresden, Germany, September 2022.
- [27] D. Schwamborn, T. Gerhold, R. Heinrich. The DLR TAU-code: recent applications in research and industry. In *ECCOMAS CFD 2006 Conference*, Delft, Netherlands, 2006.
- [28] D. Schwamborn, A. Gardner, H. von Geyr, A. Krumbein, H. Lüdeke, and A. Stürmer. Development of the TAU-Code for aerospace applications. In *50th NAL International Conference on Aerospace Science and Technology*. Bangalore, India, June 2008.
- [29] S. Langer, A. Schwöppe, and N. Kroll. The DLR Flow Solver TAU Status and Recent Algorithmic Developments. In *52nd Aerospace Sciences Meeting*. Maryland, USA, January 2014.
- [30] S. Wöhler, J. Häßy and V. Kriewall. Establishing the DLR-F25 as a research baseline aircraft for the short-medium range market in 2035. In *34th Congress of the International Council of the Aeronautical Sciences*,. Florence, Italy, September 2024.
- [31] S. Cumnuantip, M. Schulze and W. R. Krüger. Assessment of the Aeroelastic Stability of High Aspect Ratio Wing Aircraft During The Preliminary Design. In *International Forum on Aeroelasticity and Structural Dynamics*, The Hague, The Netherlands, June 2024.
- [32] D. Raymer. *Aircraft Design: A Conceptual Approach*. American Institute of Aeronautics and Astronautics, 2012. ISBN 0-930403-51-7. doi: 10.2514/4.869112.
- [33] L. R. Jenkinson, D. Rhodes and P. Simpkin. *Civil Jet Aircraft Design*. American Insitute of Aeronautics and Astronautics, 1999. ISBN 9780340741528.
- [34] J. D. Anderson. Aircraft Performance and Design. McGraw-Hill New York, 1999. ISBN 9780070702455.
- [35] F. Daoud, J. Dornwald, P. Ernstberger, H. P. Frantzen, R. Maierl, S. Deinert, and Ö. Petersson. High-Performance Aircraft Through Innovative Development Process and Methods. In 58th AIAA/ASCE/AHS/ASC Structures, Structural Dynamics, and Materials Conference, Grapevine, Texas, January 2017. doi: 10.2514/6.2017-1074.

- [36] F. Daoud, R. Maierl, P. D. Ciampa and X. Gu. Aeroelastic shape and sizing optimization of aircraft products supported by AGILE design paradigm. In *18th AIAA/ISSMO Multidisciplinary Analysis and Optimization Conference*, Denver, Colorado, June 2017. doi: 10.2514/6.2017-4141.
- [37] G. Schuhmacher, I. Murra, L. Wang, A. Laxander, O. O'Leary and M. Herold. Multidisciplinary design optimization of a regional aircraft wing box. In *9th AIAA/ISSMO Symposium on Multidisciplinary Analysis and Optimization*, Atlanta, Georgia, June 2002. doi: 10.2514/6.2002-5406.
- [38] T. H. G. Megson. *Aircraft structures for engineering students*. Elsevier, 2012. ISBN 978-0-12-822868-5.
- [39] C.-T. Sun and A. Adnan. *Mechanics of aircraft structures*. John Wiley and Sons, 2021. ISBN 978-1-119-58391-2.
- [40] L. Krog, A. Tucker, M. Kemp, and R. Boyd. Topology optimisation of aircraft wing box ribs. In *10th AIAA/ISSMO Multidisciplinary Analysis and Optimization conference*, Albany, New York, September 2004. doi: 10.2514/6.2004-4481.
- [41] T. Chen and J. Katz. Induced Drag of High-Aspect Ratio Wings. In *42nd AIAA Aerospace Sciences Meeting and Exhibit*, Reno, Nevada, January 2004. doi: 10.2514/6.2004-38.
- [42] I. H. Abbott and A. E. Von Doenhoff. Theory of wing sections: including a summary of airfoil data. Dover Publications, Inc. New York, 1959. ISBN 978-1-119-58391-2.
- [43] I. Kroo. Drag due to lift: concepts for prediction and reduction. *Annual review of fluid mechanics*, 33:587–617, 01 2001. doi: 10.1146/annurev.fluid.33.1.587.
- [44] J. Katz and A. Plotkin. *Low-speed aerodynamics*. Cambridge University Press, 2001. ISBN 9780511810329.
- [45] A. Abbas, J. De Vicente and E. Valero. Aerodynamic technologies to improve aircraft performance. *Aerospace science and technology*, 28:100–132, 2013. doi: 10.1016/j.ast.2012.10.008.
- [46] S. Deinert. Shape and Sizing Optimization of Aircraft Structures with Aeroelastic and Induced Drag Requirements. PhD thesis, Technische Universität München, Germany, 2016.
- [47] L. Prandtl. Tragflügeltheorie. In *Nachrichten von der Gesellschaft der Wissenschaften zu Goettingen*, pages 451–477, Goettingen, Germany, 1918.
- [48] M. Schulze, F. Müller, S. Cumnuantip, V. Handojo, T. Hecken, T. Klimmek, M. Ritter, and M. Zimmer. The Effect of Aspect Ratio Variation on the Preliminary Aeroelastic Assessment of a Mid-Range Transport Aircraft. In *International Forum on Aeroelasticity and Structural Dynamics* (IFASD), The Hague, The Netherlands, June 2024.
- [49] E. Torenbeek. Advanced aircraft design: conceptual design, analysis and optimization of subsonic civil airplanes. John Wiley and Sons, New York, 2013. ISBN 9781118568101.

- [50] L. Prandtl. Über Tragflügel kleinsten induzierten Widerstandes. In *Zeitschrift für Flugtechnik und Motorluftschiffahrt*, volume 24, pages 305–306, 1933.
- [51] I. Kroo. Nonplanar wing concepts for increased aircraft efficiency. *Von Karman Institute lecture series on innovative configurations and advanced concepts for future civil aircraft*, June 2005.
- [52] P. W. Jansen, R. E. Perez and J. R. A. Martins. Aerostructural optimization of nonplanar lifting surfaces. *Journal of Aircraft*, 47(5):1490–1503, September 2010. doi: 10.2514/1.44727.
- [53] R. T. Jones and A. T. Lasinski. Effect of Winglets on the Induced Drag of Ideal Wing Shapes. Technical Report TM-81230, NASA, September 1980.
- [54] C. D. Cone. The theory of induced lift and minimum induced drag of nonplanar lifting systems. Technical Report NASA-TR-R-139, National Aeronautics and Space Administration, 1962.
- [55] R. T. Whitcomb. A design approach and selected wind tunnel results at high subsonic speeds for wing-tip mounted winglets. Technical Report NASA-TN-D-8260, National Aeronautics and Space Administration, 1976.
- [56] J. M. Cansino and R. Román. Energy efficiency improvements in air traffic: The case of Airbus A320 in Spain. Energy Policy, 101:109–122, 2017. doi: 10.1016/j.enpol.2016.11.027.
- [57] L. Demasi, G. Monegato, R. Cavallaro, and R. Rybarczyk. Optimum induced drag of wingtip devices: the concept of best winglet design. *Aerotecnica Missili & Spazio*, 101:61–93, March 2022. doi: 10.1007/s42496-022-00110-z.
- [58] International Civil Aviation Organization. Annex 14 to the Convention on International Civil Aviation, Aerodromes: Volume I Aerodrome Design and Operations. Technical report, ICAO, Montreal, QC, Canada, 2018.
- [59] K. C. Bishop. Assessment of the ability of existing airport gate infrastructure to accommodate transport category aircraft with increased wingspan for improved fuel efficiency. Master's thesis, Massachusetts Institute of Technology, USA, 2012.
- [60] A. Y. N. Sofla, S. A. Meguid, K. T. Tan, W. K. Yeo. Shape morphing of aircraft wing: Status and challenges. *Materials & Design*, 31(3):1284–1292, 2010. doi: 10.1016/j.matdes.2009.09.011.
- [61] S. Barbarino, O. Bilgen, R. M. Ajaj, M. I. Friswell, D. J. Inman. A review of morphing air-craft. *Journal of intelligent material systems and structures*, 22(9):823–877, 2011. doi: 10.1177/1045389X11414084.
- [62] H. Gu, F. Healy, D. Rezgui, and J. Cooper. Sizing of high-aspect-ratio wings with folding wingtips. *Journal of Aircraft*, 60(2):461–475, 2023. doi: 10.2514/1.C036908.
- [63] F. Healy, R. Cheung, T. Neofet, M. Lowenberg, D. Rezgui, J. Cooper, A. Castrichini and T. Wilson. Folding wingtips for improved roll performance. *Journal of Aircraft*, 59(1):15–28, 2022. doi: 10. 2514/1.C036372.

- [64] R. C. M. Cheung, D. Rezgui, J. E. Cooper, and T. Wilson. Testing of folding wingtip for gust load alleviation of flexible high-aspect-ratio wing. *Journal of Aircraft*, 57(5):876–888, 2020. doi: 10.2514/1.C035732.
- [65] A. Kretov and D. Tiniakov. Evaluation of the mass and aerodynamic efficiency of a high aspect ratio wing for prospective passenger aircraft. *Aerospace*, 9(9):497, 2022. doi: 10.3390/aerospace9090497.
- [66] Y. Ma and A. Elham. Designing high aspect ratio wings: A review of concepts and approaches. *Progress in Aerospace Sciences*, 145:100983, 2024. doi: 10.1016/j.paerosci.2024.100983.
- [67] O. Stodieck, J. E. Cooper, P. M. Weaver and P. Kealy. Aeroelastic tailoring of a representative wing box using tow-steered composites. *American Institute of Aeronautics and Astronautics journal*, 55 (4):1425–1439, April 2017. doi: 10.2514/1.J055364.
- [68] P. Beaumont, C. Soutis, and A. Hodzic. Structural integrity and durability of advanced composites: Innovative modelling methods and intelligent design. Woodhead Publishing, 2015. ISBN 978-0-08-100137-0.
- [69] G. J. Kennedy. *Aerostructural analysis and design optimization of composite aircraft*. PhD thesis, University of Toronto, Canada, 2012.
- [70] T. R. Brooks, G. Kennedy and J. R. R. A. Martins. High-Fidelity Multipoint Aerostructural Optimization of a High Aspect Ratio Tow-steered Composite Wing. In 58th AIAA/ASCE/AHS/ASC Structures, Structural Dynamics, and Materials Conference, Grapevine, Texas, January 2017. doi: 10.2514/6.2017-1350.
- [71] T. R. Brooks, J. R. A. Martins and G. J. Kennedy. High-fidelity aerostructural optimization of tow-steered composite wings. *Journal of Fluids and Structures*, 88:122–147, 2019. doi: 10.1016/ j.jfluidstructs.2019.04.005.
- [72] T. R. Brooks, J. R. A. Martins and G. J. Kennedy. Aerostructural tradeoffs for tow-steered composite wings. *Journal of Aircraft*, 57(5):787–799, 2020. doi: 10.2514/1.C035699.
- [73] G. J. Kennedy and J. R. R. A. Martins. A Comparison of Metallic and Composite Aircraft Wings Using Aerostructural Design Optimization. In 14th AIAA/ISSMO Multidisciplinary Analysis and Optimization Conference, Indianapolis, Indiana, September 2012. doi: 10.2514/6.2012-5475.
- [74] R. T. Jones. The spanwise distribution of lift for minimum induced drag of wings having a given lift and a given bending moment. Technical Report NACA-TN-2249, National Advisory Committee for Aeronautics, December 1950.
- [75] J. R. A. Martins, J. J. Alonso and J. J. Reuther. High-fidelity aerostructural design optimization of a supersonic business jet. *Journal of Aircraft*, 41(3):523–530, 2004. doi: 10.2514/1.11478.
- [76] J. Nocedal and S. J. Wright. Numerical optimization. Springer, 1999. ISBN 978-0-387-40065-5.

- [77] J. R. A. Martins and A. Ning. *Engineering Design Optimization*. Cambridge University Press, 2021. ISBN 9781108833417.
- [78] I. R. Chittick and J. R. R. A. Martins. An asymmetric suboptimization approach to aerostructural optimization. *Optimization and Engineering*, 10:133–152, 2009. doi: 10.1007/ s11081-008-9046-2.
- [79] I. M. Kroo. Multidisciplinary Design Optimization: State-of-the-Art, chapter MDO for Large-Scale Design, pages 22–44. Society for Industrial and Applied Mathematics, Philadelphia, 1997. ISBN 0898713595.
- [80] J. Sobieszczanski-Sobieski and R. T. Haftka. Multidisciplinary aerospace design optimization: survey of recent developments. *Structural optimization*, 14:1–23, 1997. doi: 10.1007/BF01197554.
- [81] J. R. A. Martins, J. J. Alonso and J. J. Reuther. A coupled-adjoint sensitivity analysis method for high-fidelity aero-structural design. *Optimization and Engineering*, 6:33–62, 2005. doi: 10.1023/B: OPTE.0000048536.47956.62.
- [82] M. Bras, A. Suleman, R. Diogo and A. C. Marta. Ant colony optimization method applied to topology optimization of aircraft structures. In 26th Canadian Congress of Applied Mechanics (CANCAM), Victoria, British Columbia, Canada, June 2017.
- [83] R. P. Henderson, J. R. A. Martins and R. E. Perez. Aircraft conceptual design for optimal environmental performance. *The Aeronautical Journal*, 116(1175):1–22, 2012. doi: 10.1017/ S000192400000659X.
- [84] H. Wu, S. Li, D. Shi, X. Yang, and H. Qi. Optimization Design Method for High-Aspect-Ratio Composite Wing Based on Neural Network and Genetic Algorithm. In *International Conference on Computational and Experimental Simulations in Engineering*, Singapore, August 2024. doi: 10.1007/978-3-031-81673-4_35.
- [85] P. E. Gill, W. Murray, and M. A. Saunders. SNOPT: An SQP Algorithm for Large-Scale Constrained Optimization. *SIAM Review*, 47(1):99–131, 2005. doi: 10.1137/S003614450446096.
- [86] K. Schittkowski. NLPQL: A FORTRAN subroutine solving constrained nonlinear programming problems. *Annals of operations research*, 5:485–500, 1986. doi: 10.1007/BF02022087.
- [87] J. R. A. Martins and J. T. Hwang. Review and unification of methods for computing derivatives of multidisciplinary computational models. *AIAA journal*, 51(11):2582–2599, November 2013. doi: 10.2514/1.J052184.
- [88] J. lott, R. T. Haftka, and H. M. Adelman. Selecting step sizes in sensitivity analysis by finite differences. Technical Memorandum 86382, National Aeronautics and Space Administration, 1985.
- [89] R. E. Perez, P. W. Jansen and J. R. A. Martins. pyOpt: a Python-based object-oriented framework for nonlinear constrained optimization. *Structural and Multidisciplinary Optimization*, 45: 101–118, 2012. doi: 10.1007/s00158-011-0666-3.

- [90] J. R. A. Martins, I. Kroo and J. Alonso. An automated method for sensitivity analysis using complex variables. In 38th Aerospace Sciences Meeting and Exhibit, number AIAA Paper 2000-0689, 2000. doi: 10.2514/6.2000-689.
- [91] J. R. A. Martins, P. Sturdza and J. Alonso. The complex-step derivative approximation. ACM Transactions on Mathematical Software (TOMS), 29(3):245–262, 2003. doi: 10.1145/838250. 838251.
- [92] J. R. R. A. Martins, P. Sturdza and J. Alonso. The connection between the complex-step derivative approximation and algorithmic differentiation. In *39th Aerospace Sciences Meeting and Exhibit*, number AIAA Paper 2001-0921, 2001. doi: 10.2514/6.2001-921.
- [93] C. A. Mader, J. R. A. Martins, J. J. Alonso and E. Van der Weide. ADjoint: An approach for the rapid development of discrete adjoint solvers. *AIAA journal*, 46(4):863–873, 2008. doi: 10.2514/1.29123.
- [94] A. C. Marta. Rapid development of discrete adjoint solvers with applications to magnetohydrodynamic flow control. PhD thesis, Stanford University, USA, 2007.
- [95] A. C. Marta, C. A. Mader, J. R. A. Martins, E. Van der Weide and J. J. Alonso. A methodology for the development of discrete adjoint solvers using automatic differentiation tools. *International Journal of Computational Fluid Dynamics*, 21(9-10):307–327, 2007. doi: 10.1080/ 10618560701678647.
- [96] J. R. A. Martins. *A coupled-adjoint method for high-fidelity aero-structural optimization*. PhD thesis, Stanford University, USA, 2003.
- [97] J. R. A. Martins and A. B. Lambe. Multidisciplinary design optimization: a survey of architectures. *AIAA journal*, 51(9):2049–2075, 2013. doi: 10.2514/1.J051895.
- [98] A. B. Lambe and J. R. A. Martins. Extensions to the design structure matrix for the description of multidisciplinary design, analysis, and optimization processes. *Structural and Multidisciplinary Optimization*, 46:273–284, 2012. doi: 10.1007/s00158-012-0763-y.
- [99] J. Gray, K. Moore, T. Hearn, and B. Naylor. A standard platform for testing and comparison of MDAO architectures. In 53rd AIAA/ASME/ASCE/AHS/ASC Structures, Structural Dynamics and Materials Conference, Honolulu, Hawaii, April 2012.
- [100] N. P. Tedford and J. R. R. A. Martins. Benchmarking multidisciplinary design optimization algorithms. *Optimization and Engineering*, 11:159–183, 2010. doi: 10.1007/s11081-009-9082-6.
- [101] G. Kennedy and J. R. A. Martins. Parallel solution methods for aerostructural analysis and design optimization. In 13th AIAA/ISSMO multidisciplinary analysis optimization conference, Fort Worth, Texas, September 2010. doi: 10.2514/6.2010-9308.

- [102] S. S. Chauhan, J. T. Hwang and J. R. R. A. Martins. An automated selection algorithm for nonlinear solvers in MDO. *Structural and Multidisciplinary Optimization*, 58:349–377, 2018. doi: 10.1007/s00158-018-2004-5.
- [103] S. Deinert, Ö. Petersson, F. Daoud and H. Baier. Aircraft loft optimization with respect to aeroelastic lift and induced drag loads. In *10th World Congress on Structural and Multidisciplinary Optimization*, Orlando, Florida, May 2013.
- [104] H. Golombek. Comparison of aeroelastic structural sizing approaches for aircraft conceptual design. Master's thesis, Technische Universität Braunschweig, Germany, 2024.
- [105] R. L. Bisplinghoff and H. Ashley. *Principles of aeroelasticity*. Dover Books on Engineering. Dover Publications, 2 edition, 2013. ISBN 9780486613499.
- [106] R. Maierl, A. Gastaldi, J. N. Walther and A. Jungo. Aero-structural optimization of a MALE configuration in the AGILE MDO framework. In *Flexible Engineering Toward Green Aircraft: CAE Tools for Sustainable Mobility*, volume 92, pages 169–187. Springer, 2020. ISBN 978-3-030-36514-1.
- [107] I. Berezin, P. Sarkar, and J. Malecki. Fluid-structure interaction simulation. *Recent Progress in Flow Control for Practical Flows: Results of the STADYWICO and IMESCON Projects*, pages 263–281, 2017. doi: 10.1007/978-3-319-50568-8_14.
- [108] M. Drela. Flight vehicle aerodynamics. MIT press, 2014. ISBN 9780262319928.
- [109] E. Albano and W. P. Rodden. A doublet-lattice method for calculating lift distributions on oscillating surfaces in subsonic flows. *AIAA Journal*, 7(2):279–285, 1969. doi: 10.2514/3.5086.
- [110] T. P. Kalman, W. P. Rodden and J. P. Giesing. Application of the doublet-lattice method to nonplanar configurations in subsonic flow. *Journal of Aircraft*, 8(6):406–413, 1971. doi: 10.2514/3.59117.
- [111] W. P. Rodden, P. F. Taylor and S. C. McIntosh. Further refinement of the subsonic doublet-lattice method. *Journal of Aircraft*, 35(5):720–727, 1998. doi: 10.2514/2.2382.
- [112] S. G. Hedman. Vortex lattice method for calculation of quasi steady state loadings on thin elastic wings in subsonic flow. Technical Report 105, Aeronautical Research Institute of Sweden, 1966.
- [113] T. M. Kier. Comparing different potential flow methods for unsteady aerodynamic modelling of a flutter demonstrator aircraft. In AIAA SciTech 2023 Forum. National Harbor, Maryland, January 2023. doi: 10.2514/6.2023-0177.
- [114] E. Sulaeman. *Effect of compressive force on aeroelastic stability of a strut-braced wing.* PhD thesis, Virginia Polytechnic Institute and State University, USA, 2002.
- [115] J. N. Reddy. Mechanics of laminated composite plates and shells: theory and analysis. CRC press, second edition, 2003. ISBN 9780849315923.
- [116] R. M. Jones. *Mechanics of composite materials*. CRC press, second edition, 2018. ISBN 9781315272986.

- [117] J. N. Reddy. *An introduction to the finite element method*. McGraw-Hill New York, fourth edition, 2019. ISBN 9781259861901.
- [118] O. C. Zienkiewicz and R. L. Taylor. *The finite element method for solid and structural mechanics*. Elsevier, seventh edition, 2014. ISBN 978-1-85617-634-7.
- [119] MSC Software Corporation. Nastran quick reference guide, 2021.
- [120] C. M. Ribas. Comparison of the response of different rivet layout patterns in aircraft repair patches. Master's thesis, Universitat Politècnica de Catalunya, Spain, 2021.
- [121] S. Gnanasekar, B. Santhosh, V. Rajamohan, V. Raj, H. Elangovan and V. Barathan. Strength and stability analysis of composite inverted conical structure. *International Journal of Mechanics and Materials in Design*, pages 1–27, 2024. doi: 10.1007/s10999-024-09723-7.
- [122] R. L. Harder and R. N. Desmarais. Interpolation using surface splines. *Journal of Aircraft*, 9(2): 189–191, 1972. doi: 10.2514/3.44330.
- [123] P. M. Weaver. On Optimisation of Long Anisotropic Flat Plates Subject to Shear Buckling Loads. In 45th AIAA/ASME/ASCE/AHS/ASC Structures, Structural Dynamics and Materials Conference. Palm Springs, California, April 2004. doi: 10.2514/6.2004-2053.
- [124] P. M. Weaver. Design Formulae for Buckling of Biaxially Loaded Laminated Rectangular Plates with Flexural/twist Anisotropy. In 46th AIAA/ASME/ASCE/AHS/ASC Structures, Structural Dynamics and Materials Conference. Austin, Texas, April 2005. doi: 10.2514/6.2005-2105.
- [125] P. M. Weaver. Approximate analysis for buckling of compression loaded long rectangular plates with flexural/twist anisotropy. *Proceedings of the Royal Society A: Mathematical, Physical and Engineering Sciences*, 462(2065):59–73, 2006. doi: 10.1098/rspa.2005.1552.
- [126] D. E. Calderon, J. E. Cooper, M. Lowenberg, S. A. Neild and E. B. Coetzee. Sizing High-Aspect-Ratio Wings with a Geometrically Nonlinear Beam Model. *Journal of Aircraf*, 56:1455–1470, 2019. doi: 10.2514/1.C035296.
- [127] M. Niu. Airframe Stress Analysis and Sizing. Hong Kong Conmilit Press, 1997. ISBN 9627128120.
- [128] G. Ntourmas, F. Glock, F. Daoud, G. Schuhmacher, D. Chronopoulos, and E. Özcan. Mixed integer linear programming formulations of the stacking sequence and blending optimisation of composite structures. *Composite Structures*, 264:113660, 2021. doi: 10.1016/j.compstruct.2021.113660.
- [129] L. Reimer. The FlowSimulator A Software Framework for CFD-related Multidisciplinary Simulations. In *European NAFEMS Conference Computational Fluid Dynamics (CFD) Beyond the Solve*. Munich, Germany, December 2015.
- [130] M. Meinel and G. Ó. Einarsson. The FlowSimulator framework for massively parallel CFD applications. In *Applied parallel and scientific computing 10th International Conference*. Reykjavik, Iceland, June 2010.

- [131] F. Volle. Structure Optimization for Improving Aero-Elastic Cruise Performance of an Aircraft Using the Adjoint Approach. In *EUROGEN Conference*, Crete, Greece, June 2023.
- [132] F. Volle. Aero-Structural Optimization of the AIAA MDO Benchmark Model With TAU and Lagrange. In AIAA SCITECH 2025 Forum, Orlando, Florida, January 2025. doi: 10.2514/6. 2025-2815.
- [133] A. C. Gray and J. R. R. A. Martins. A proposed benchmark model for practical aeroelastic optimization of aircraft wings. In AIAA SciTech 2024 Forum. Orlando, Florida, January 2024. doi: 10.2514/6.2024-2775.
- [134] U. Küttler and A. W. Wall. Fixed-point fluid-structure interaction solvers with dynamic relaxation. *Computational mechanics*, 43(1):61–72, 2008. doi: 10.1007/s00466-008-0255-5.
- [135] A. Schuster, L. Reimer and J. Neumann. A Mesh-Free Parallel Moving Least-Squares-based Interpolation Method for the Application in Aeroelastic Simulations With the Flow Simulator. *New Results in Numerical and Experimental Fluid Mechanics X*, 132:573–583, 2016. doi: 10.1007/978-3-319-27279-5_50.
- [136] A. Rempke. Netzdeformation mit Elastizitätsanalogie in multidisziplinärer FlowSimulator-Umgebung. In *Jahresbericht 2016 zum 20. DGLR-Fach-Symposium der STAB*. Braunschweig, Germany, November 2016.
- [137] F. Müller. The impacts of aspect ratio variations in preliminary design of a mid-range jet transport aircraft. Master's thesis, Université de Liège, Belgique, 2024.
- [138] Å. R. Triviño. Horizontal double bubble aircraft design for the middle of the market. Master's thesis, Universidad Europea De Madrid, Spain, 2024.
- [139] Airbus. A321 aircraft characteristics airport and maintenance planning. Technical report, Airbus S.A.S., 2005.
- [140] S. Boyd and L. Vandenberghe. *Convex optimization*. Cambridge university press, 2004. ISBN 78-0-521-83378-3.
- [141] M. Orlita and R. Vos. Cruise Performance Optimization of the Airbus A320 through Flap Morphing. In 17th AIAA Aviation Technology, Integration, and Operations Conference. Denver, Colorado, June 2017.

Appendix A

Structural Sizing Optimisation

A.1 Static Structural Sizing

A.1.1 F25-AR17

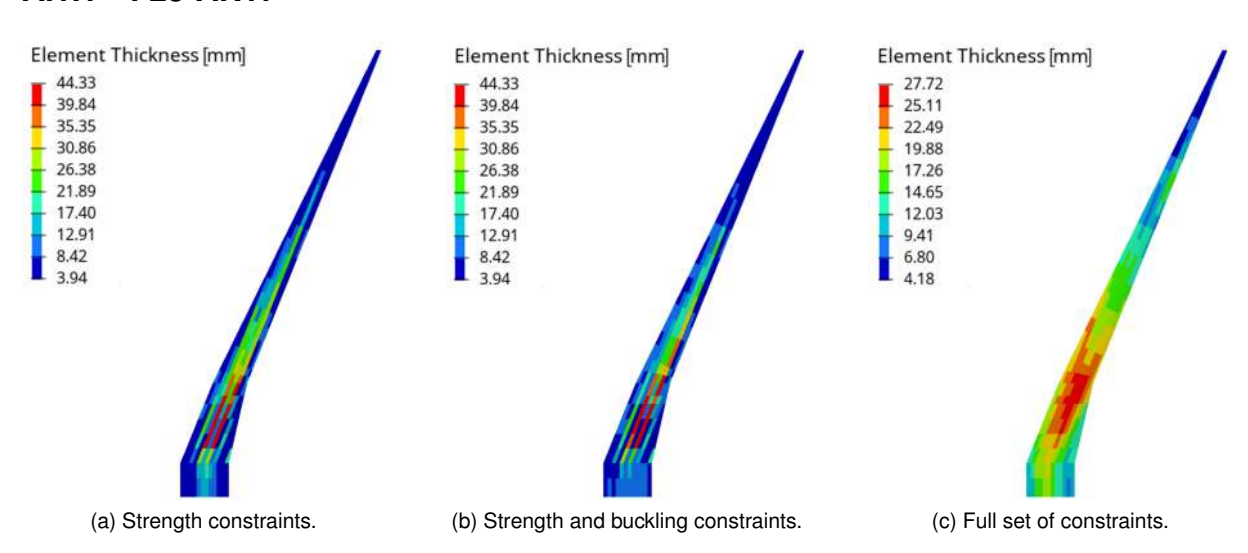


Figure A.1: F25-AR17 wing upper skin thickness distribution throughout the static structural sizing.

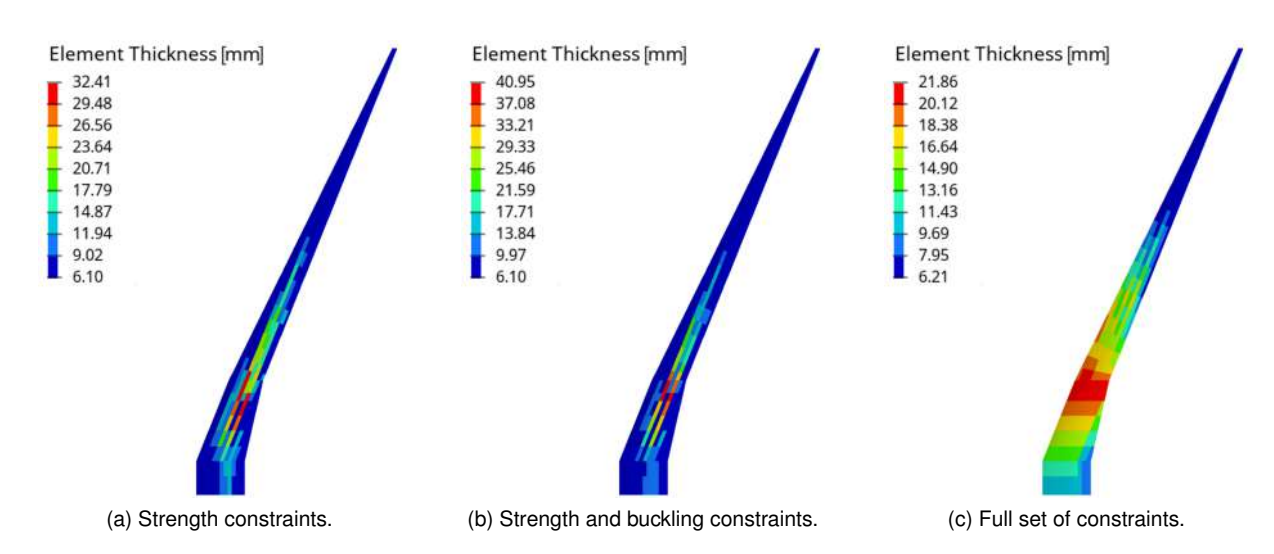


Figure A.2: F25-AR17 wing lower skin thickness distribution throughout the static structural sizing.

A.2 Aeroelastic Structural Sizing

A.2.1 F25-AR15

Spars and Stringers

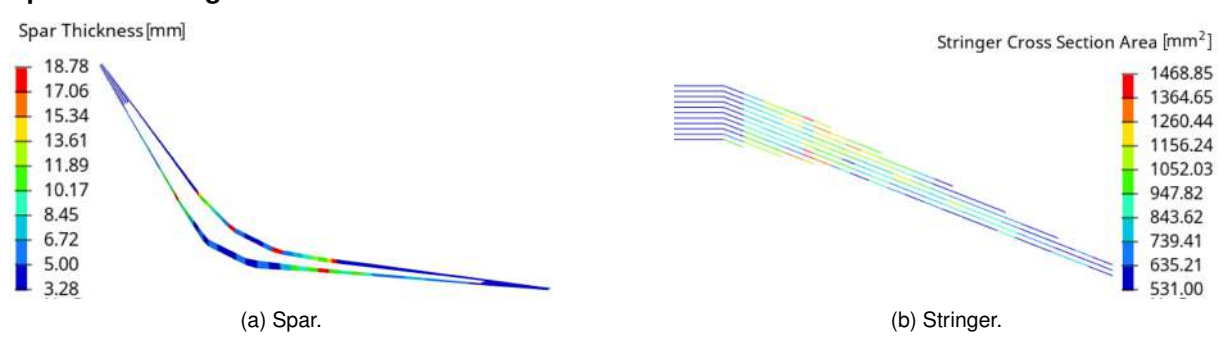
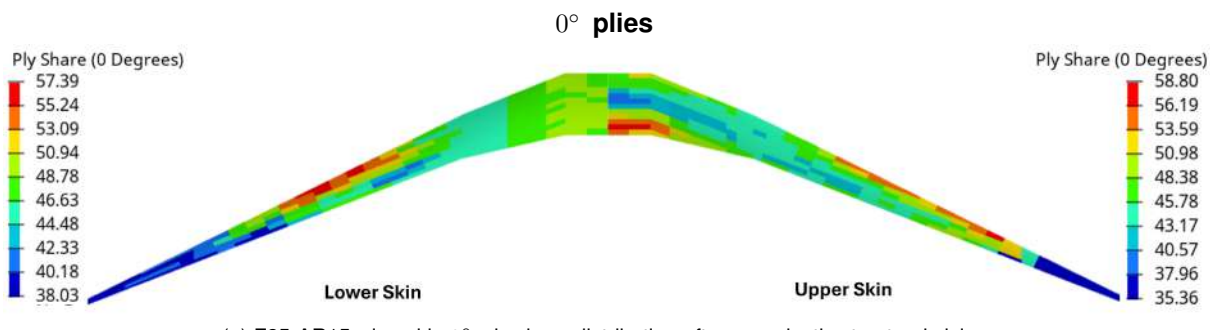
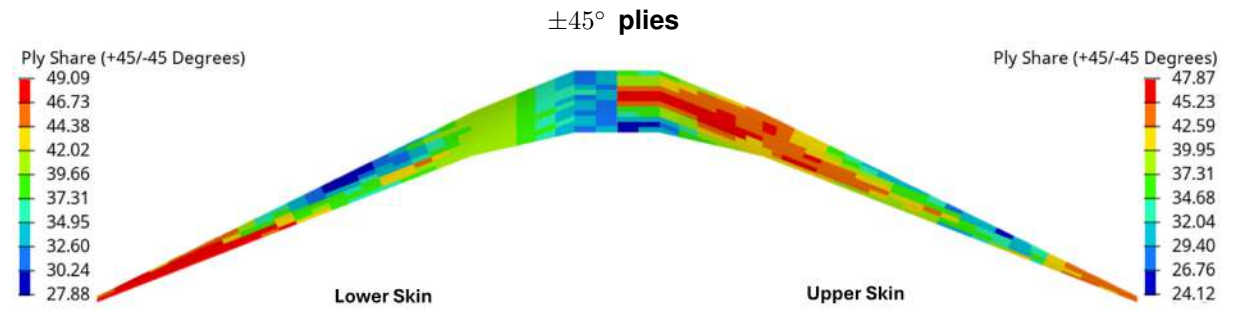


Figure A.3: F25-AR15 spar and stringer dimensions after aeroelastic structural sizing.

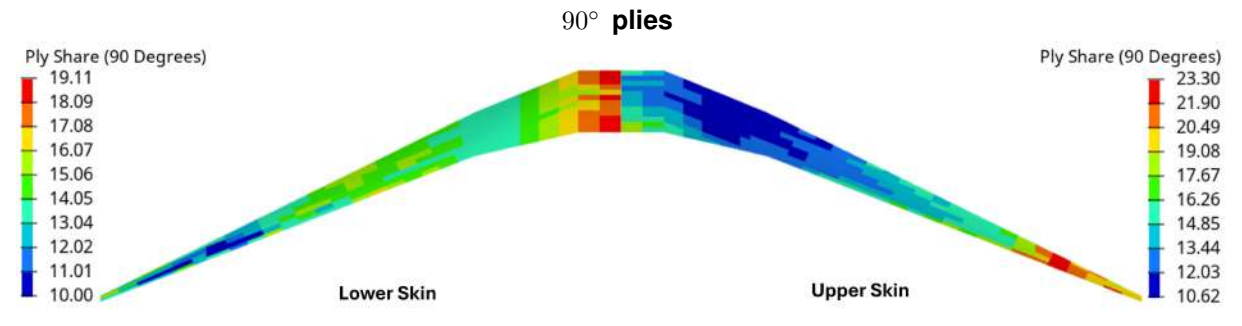
Wing Skin Ply Shares



(a) F25-AR15 wing skin $0^\circ\,$ ply share distribution after aeroelastic structural sizing.



(b) F25-AR15 wing skin $\pm 45^{\circ}$ ply share distribution after aeroelastic structural sizing.



(c) F25-AR15 wing skin $90^{\circ}\,$ ply share distribution after aeroelastic structural sizing.

Figure A.4: F25-AR15 wing skin ply share distribution after aeroelastic structural sizing.

Wing Skin Reserve Factors

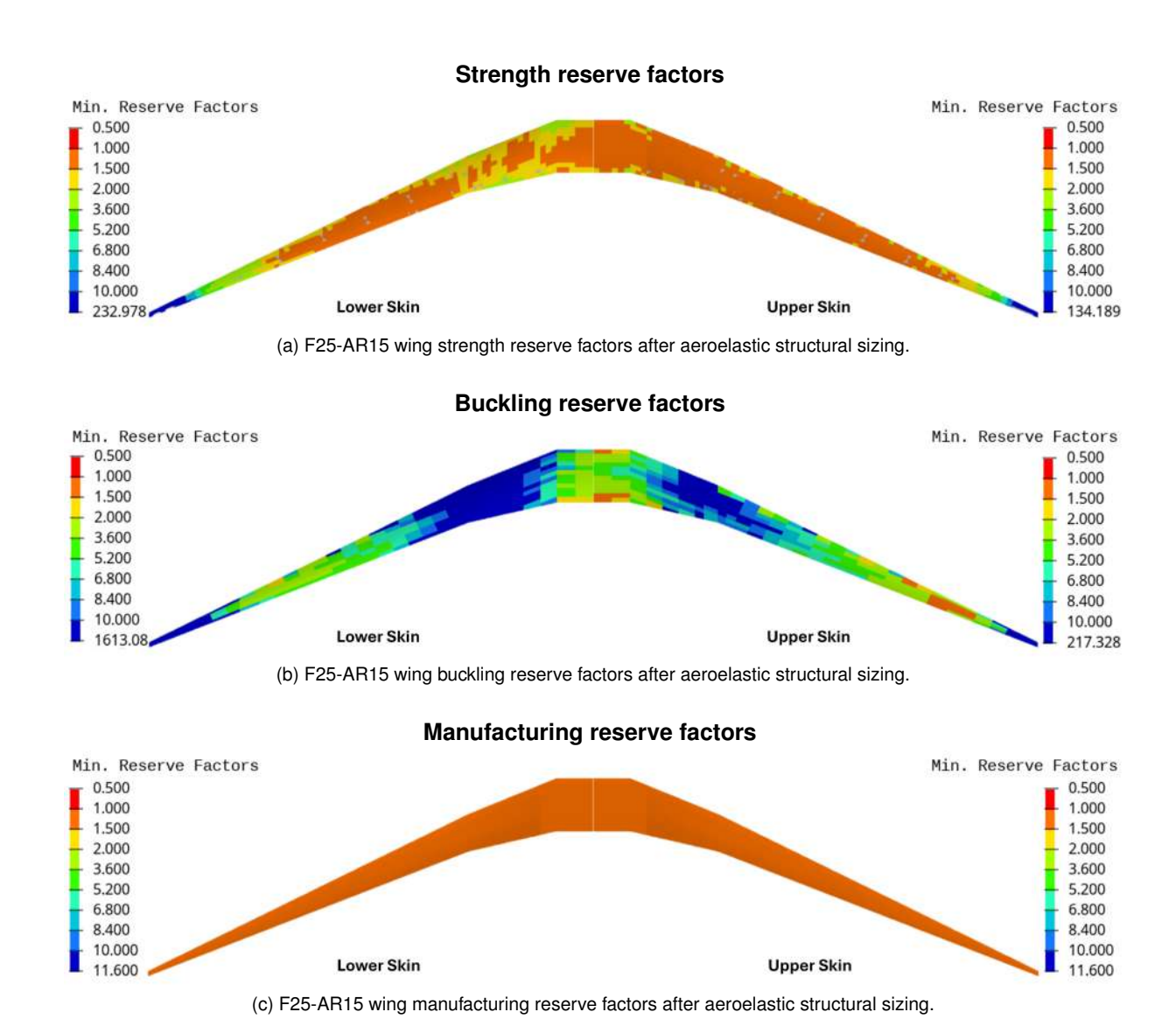


Figure A.5: F25-AR15 wing skin reserve factors after aeroelastic structural sizing.

A.2.2 F25-AR17

Spars and Stringers

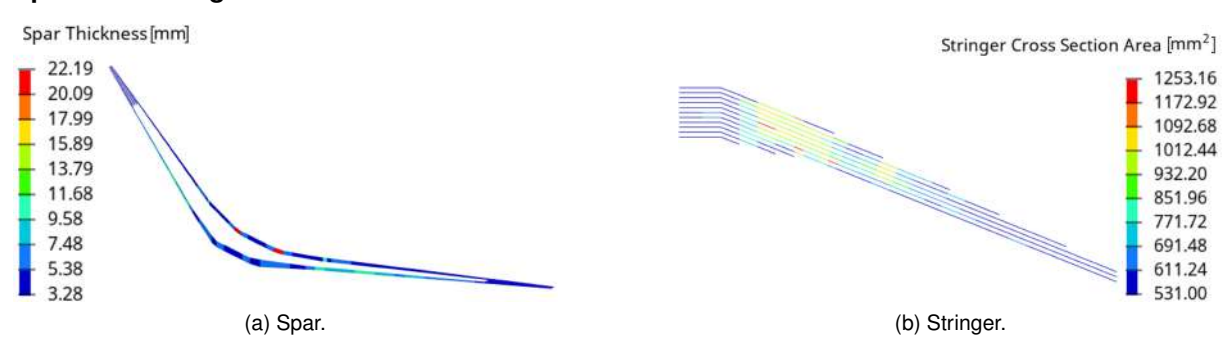


Figure A.6: F25-AR17 spar and stringer dimensions after aeroelastic structural sizing.

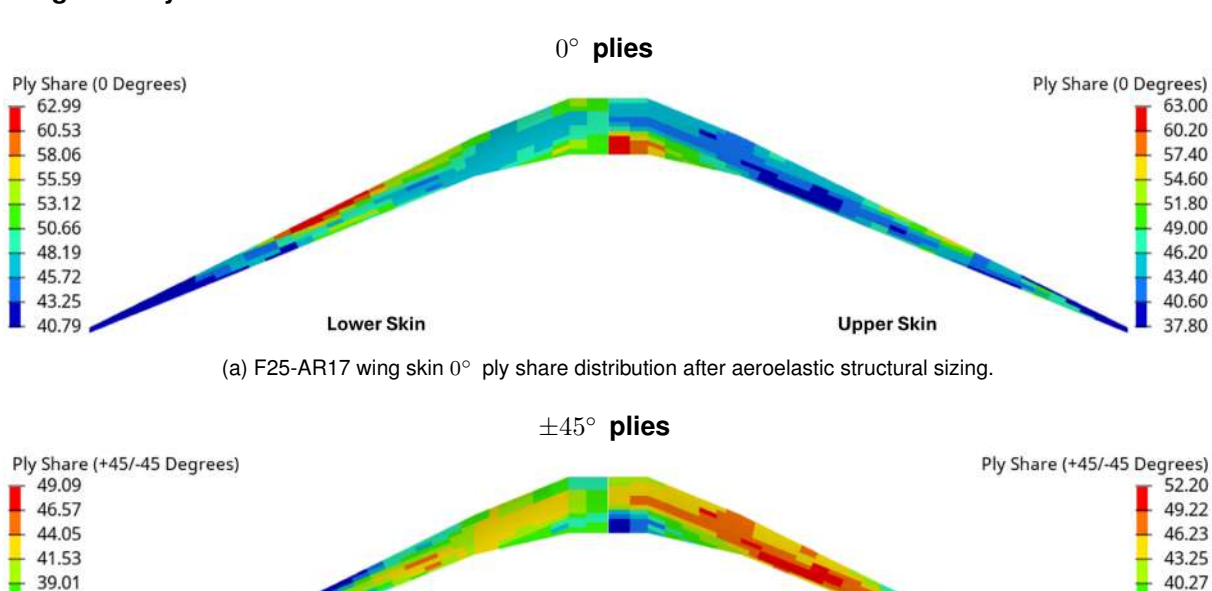
Wing Skin Ply Shares

36.49 33.97

31.46

28.94

26.42



(b) F25-AR17 wing skin $\pm 45^{\circ}\,$ ply share distribution after aeroelastic structural sizing.

Upper Skin

Lower Skin

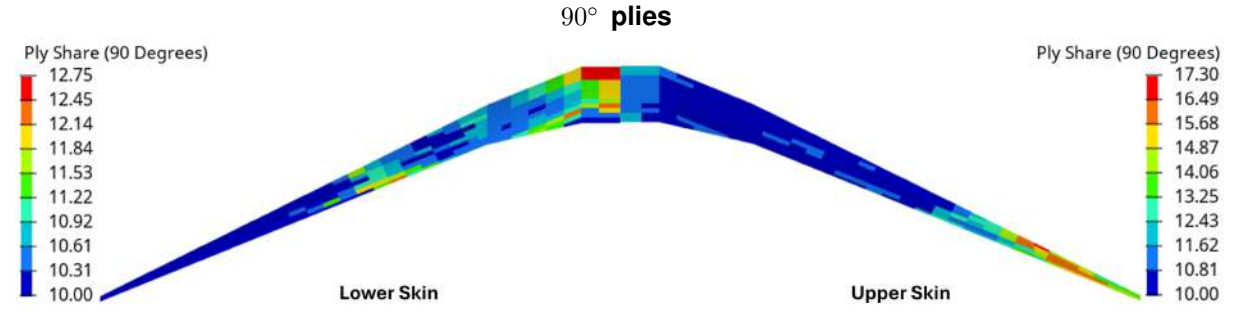
37.29

34.30

31.32

28.34

25.35



(c) F25-AR17 wing skin $90^\circ\,$ ply share distribution after aeroelastic structural sizing.

Figure A.7: F25-AR17 wing skin ply share distribution after aeroelastic structural sizing.

Wing Skin Reserve Factors

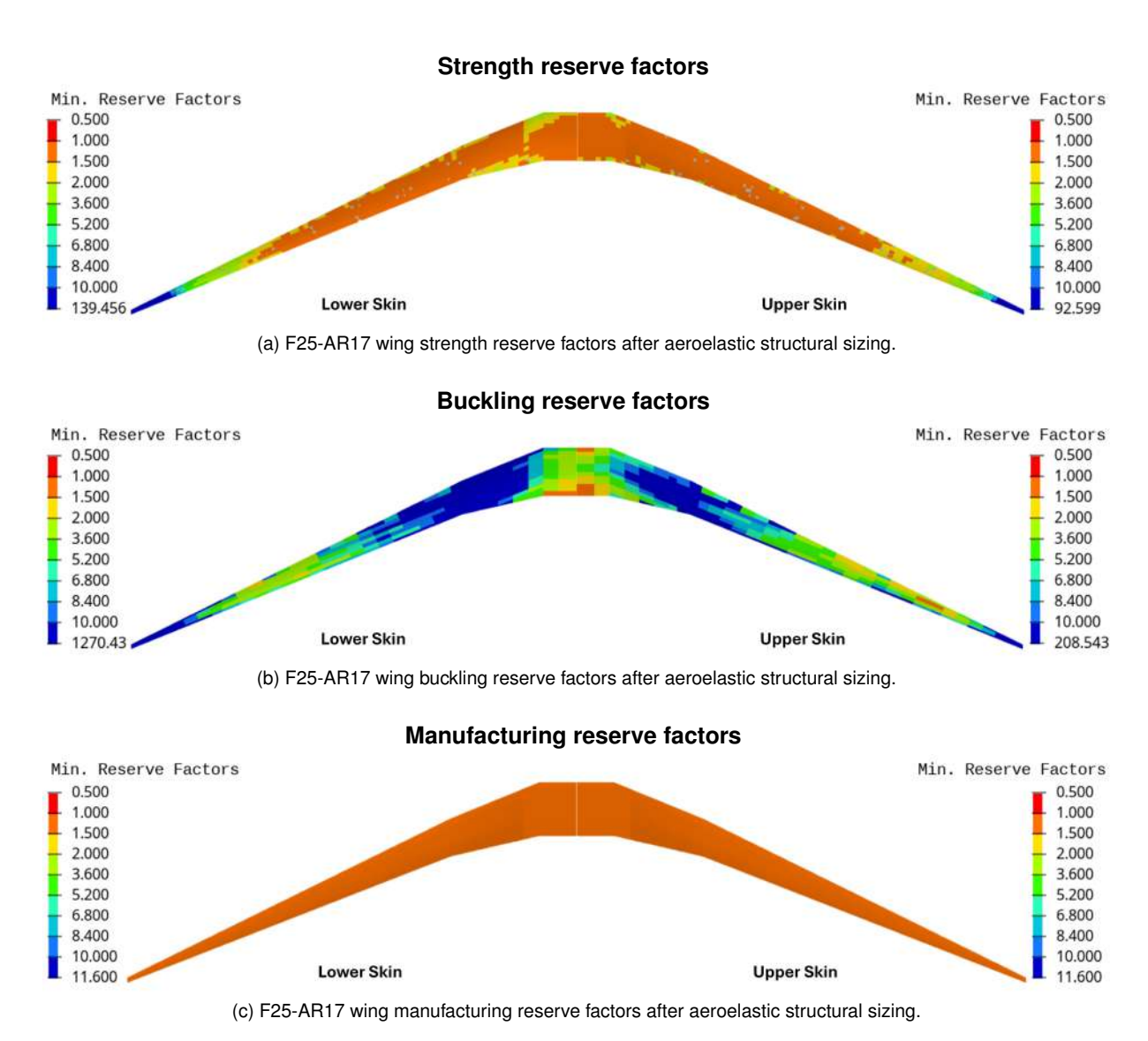


Figure A.8: F25-AR17 wing skin reserve factors after aeroelastic structural sizing.